Electrically-driven Photonic Crystal Lasers

Dimopoulos, Evangelos

Publication date:
2023

Document Version
Publisher's PDF, also known as Version of record

Doctor of Philosophy
Doctoral thesis in Photonics Engineering

DTU Electro
Department of Electrical and Photonics Engineering

Electrically-Driven Photonic Crystal Lasers

Evangelos Dimopoulos

Kongens Lyngby, Denmark 2023

Evangelos Dimopoulos
Electrically-Driven Photonic Crystal Lasers
PhD thesis, February 2023

Supervisors:
Professor Jesper Mørk
Professor Kresten Yvind
Senior Researcher Yi Yu

Technical University of Denmark
Department of Electrical and Photonics Engineering
Ørsteds Plads, Building 343
2800 Kongens Lyngby, Denmark
www.electro.dtu.dk

Abstract

The rising demand for integrated optical communication and data processing solutions is fueling the advancement of on-chip photonic components that are ultra-compact and energy-efficient. A critical element of this endeavor is the development of high-performance small-footprint light sources that can be integrated onto silicon. Among various on-chip sources, heterogeneously-integrated photonic crystal lasers are gaining momentum as a promising solution for on-chip applications.

This thesis is focused on the demonstration and investigation of electrically-driven photonic crystal membrane lasers based on the InP-on-Si platform. A critical element of the lasers is the photonic crystal cavities, and their properties under different design variations and their characterization is analysed. Importantly, the effect of disorder and doping is investigated, showing that doping-induced losses are the primary determinant of the quality factor of the photonic crystal laser cavities.

Furthermore, the static characteristics of the lasers are studied, demonstrating ultra-low threshold current at continuous-wave room temperature operation. The thermal analysis revealed minimal self-heating under typical operating conditions but high sensitivity to ambient temperature. The main limiting factor of the laser performance is identified as a high leakage current that hinders the injection efficiency.

In addition, the properties of photonic crystal lasers are studied by systematically varying the active material size leading to unprecedented miniaturization and the demonstration of the first laser achieving sub-µA threshold at room temperature to date. The dynamic properties of the lasers were characterized via small-signal analysis, showing high modulation efficiency and high damping. Furthermore, the lasers exhibit ultra-low operating energy below 1 fJ bit^{-1} at typical processor clock speeds.

Finally, the properties of the Fano lasers and their corresponding passive cavities are explored, paving the way for a successful demonstration of the first electrically-driven Fano Laser.

Electrically-driven photonic crystal lasers show great potential offering immense possibilities for the future of on-chip light sources and photonic integrated circuits. This technology is at the forefront of a new era of miniaturization and cost-effectiveness that will revolutionize photonics and on-chip communications.

Resumé

Den stigende efterspørgsel på integrerede optiske kommunikations- og databehandlingsløsninger kræver at der udvikles nye on-chip ("på chippen") fotoniske komponenter, der er ultrakompakte og energieffektive. Et nøgleelement i denne bestræbelse er udviklingen af kompakte, effektive lyskilder, som kan integreres på silicium. Blandt forskellige on-chip-kilder er heterogent integrerede fotoniske krystallasere en lovende løsning til on-chip-applikationer.

Fokus for denne afhandling er på eksperimentelle demonstrationer og studier af elektrisk drevne fotoniske krystalmembranlasere baseret på Indiumfosfid-på-siliciumplatformen ("InP-on-Si"). Et vigtigt element i den fotoniske krystallaser er selve kaviteten, og i afhandlingen analyseres kavitetens egenskaber under forskellige designvariationer. Effekten af uorden og doterings studeres, og undersøgelserne viser, at doterings-inducerede tab er den primære årsag til reduktion af kvalitetsfaktoren af de fotoniske krystallaserkaviteter.

Desuden studeres lasernes statiske egenskaber, og der demonstreres ekstremt lav tærskelstrøm ved kontinuerlig pumpning ved stuetemperatur. En termiske analyse afslørede minimal selvopvarmning under typiske driftsforhold, men høj følsomhed over for temperaturen i det omkringværende miljø. Den væsentligste begrænsende faktor for laseren er identificeret som en høj lækstrøm, der mindsker injektionseffektiviteten.

Derudover studeres de lasernes egenskaber ved systematisk at variere volumenet af det aktive materiale, hvilket fører til hidtil uset miniaturisering og påvisning af den første laser nogensinde med en tærskelstrøm på under én mikroampere ved stuetemperatur. Lasernes dynamiske egenskaber blev desuden karakteriseret via dynamiske små-signal målinger, der viser høj modulationseffektivitet og høj dæmpning. Desuden udviser laserne ekstremt lav driftsenergi på under 1 fJ bit^{-1} ved typiske klokfrekvenser for computerprocessorer..

Til sidst udforskes Fano-lasernes en ny type laser, den såkaldte Fano laser, og for første gang demonstreres en elektrisk-drevet Fano laser. Der rapporteres detaljerede undersøgelser af egenskaberne af passive Fano kaviteter.

Elektrisk drevne fotoniske krystallasere har et stort potentiale, specielt indenfor anvendelser, hvor der er behov for on-chip lyskilder til integrerede fotoniske kredsløb.

Preface

This thesis is submitted in partial fulfillment of the requirements for the Ph.D. degree from the Technical University of Denmark (DTU). The project was carried out in the *Quantum and Laser Photonics* group at the Department of Electrical and Photonics Engineering (DTU Electro) from September 2019 to February 2023 under the supervision of Professor Jesper Mørk, Professor Kresten Yvind, and Senior Researcher Yi Yu.

The project has been a part of the research activities in the NAnophotonics for TErabit Communications (NATEC) center of excellence, financially supported by the Villum Fonden. The project was also part of the NanoPhoton - Center for Nanophotonics research activities supported by the Danish National Research Foundation and the European Research Council project on Fano Photonics.

Kongens Lyngby, Denmark
March 15, 2023

Evangelos Dimopoulos

Acknowledgements

First and foremost, I would like to deeply thank my principal supervisor Jesper Mørk, who entrusted me with this project. His guidance and support throughout this project were invaluable. Most of all, I am thankful to work by his side, for he leads by example and inspires me to become a better researcher and person. I would also like to thank my co-supervisor Kresten Yvind, who instilled in me a love for semiconductor lasers and processing, and for the pleasure of discussing interesting and challenging physics. I would also like to express gratitude to my co-supervisor Yi Yu for all the fruitful conversations sharing his knowledge and experience.

The success of this project would not have been possible without the collective work of multiple people to whom I am deeply grateful. In particular, I would like to express my gratitude to Aurimas Sakanas and Andrey Marchevsky for their immense work on developing the crucial technologies required to realize electrically-pumped nanolasers. I would also like to thank Meng Xiong for her excellent work and continuous support in nanofabrication. My heartfelt thanks go to Marco Saldutti for the insightful and challenging discussions on the lasers' physical behavior and theoretical modeling. I would also like to thank Gaoneng Dong for the fruitful conversations and his help in the lab. I would also like to offer my thanks my peer Quentin Saudan for the excellent discussions about fabrication issues and his work on the GDSpy mask. I am also thankful to Dagmawi Bekele for his constant support and work on the HERO project. Finally, I would like to express my gratitude to Kristoffer S. Mathiesen for his work on the HERO project, his beautiful ideas, and for sharing his knowledge at the start of my PhD.

Furthermore, I would like to thank all of my friends and peers from the Quantum and Laser Photonics group and the Nanophotonics Section for making the work during my PhD so memorable. Their positiveness and happy feelings transformed the long hours and made DTU feel like home.

Finally, I am very grateful to my family for their love and support, especially my dear sister, Chrysoula, for always inviting me to the best Jazz concerts in town! I would also like to thank my lovely partner, Maria, for her love, encouragement, and coping with me throughout the project.

List of Publications

The following publications have been authored or co-authored during the course of the PhD project:

Journal Publications

- **E. Dimopoulos**, M. Xiong, A. Sakanas, A. Marchevsky, G. Dong, Y. Yu, E. Semenova, J. Mørk, and K. Yvind, "Experimental Demonstration of Nanolaser with sub-µA Threshold Current", arXiv:2212.05148., *submitted*
- **E. Dimopoulos**, A. Sakanas, A. Marchevsky, M. Xiong, Y. Yu, E. Semenova, J. Mørk, and K. Yvind, "Electrically-driven Photonic Crystal Lasers with Ultra-low Threshold", Laser & Photonics Reviews, 2200109 (2022)
- M. Saldutti; M. Xiong, **E. Dimopoulos**, Y. Yu, M. Gioannini, and J. Mørk, "Modal Properties of Photonic Crystal Cavities and Applications to Lasers", Nanomaterials 2021, 11, 3030 (2021)
- **E. Dimopoulos**, G. Dong, M. Xiong, A. Sakanas, A. Marchevsky, Y. Yu, E. Semenova, K. Yvind, and J. Mørk, "Electrically-driven Fano Laser", *in preparation*

Conference Proceedings

- **E. Dimopoulos**, A. Sakanas, A. Marchevsky, M. Xiong, G. Dong Y. Yu, E. Semenova, J. Mørk, and K. Yvind, "Properties of Heterogeneously Integrated Photonic Crystal Nanolasers with Ultra-low Threshold Current," in Conference on Lasers and Electro-Optics (2023), *accepted*)
- **E. Dimopoulos**, A. Sakanas, A. Marchevsky, M. Xiong, Y. Yu, E. Semenova, J. Mørk, and K. Yvind, "Properties of Heterogeneously Integrated Photonic Crystal Nanolasers with Ultra-low Threshold Current," in Conference on Lasers and Electro-Optics, Technical Digest Series (Optica Publishing Group, 2022)

- J. Mørk, **E. Dimopoulos**, Y. Yu, M. Xiong, A. Sakanas, A. Marchevsky, M. Saldutti, E. Semenova, K. Yvind, "Semiconductor nanolasers", 2022 28th International Semiconductor Laser Conference (ISLC), pp. 1-2 (2022)
- G. Dong, M. Xiong, **E. Dimopoulos**, A. Sakanas, E. Semenova, K. Yvind, Y. Yu, and J. Mork, "Fano Laser Based on a Photonic Crystal Nanobeam Cavity," in Conference on Lasers and Electro-Optics, Technical Digest Series (Optica Publishing Group, 2022)
- M. Xiong, A. Sakanas, **E. Dimopoulos**, R. E. Christiansen, E. Semenova, O. Sigmund, Y. Yu, K. Yvind, and J. Mørk, "Experimental Realization of Topology-Optimized InP Photonic Cavities with Extreme Dielectric Confinement," in OSA Advanced Photonics Congress 2021 (2021)
- **E. Dimopoulos**, A. Sakanas, A. Marchevsky, M. Xiong, Y. Yu, E. Semenova, K. Yvind, J. Mørk, "Comparison of electrically and optically pumped buried-heterostructure photonic crystal lasers," 2021 Conference on Lasers and Electro-Optics Europe & European Quantum Electronics Conference (CLEO/Europe-EQEC), pp. 1-1 (2021)
- A. Sakanas, A. Marchevsky, **E. Dimopoulos**, M. Xiong, Y. Yu, K. S. Mathiesen, E. Semenova, J. Mørk, and K. Yvind, "Electrically-operated buried-heterostructure nanocavity laser with sub-20 A threshold current," in Conference on Lasers and Electro-Optics 2021 (Optica Publishing Group, 2021)

Contents

CHAPTER 1

Introduction

Throughout human history, communication has played a pivotal role in shaping society. The evolution of communication technologies has been significant, from the transmission of simple yet crucial messages over long distances via smoke signals to the modern-day transmission of internet data using lasers and optical fibers. Today's unprecedented access to information and the progress in computing enabled the digitalization revolution that transformed our way of life, providing new insights and opportunities for innovation. However, this progress is hindered by the increased energy costs of conventional communication technologies. In particular, ohmic losses in electrical interconnects, e.g., within computers, is a large source of unnecessary energy loss. The solution to this problem is analogous to the development of revolutionary technologies for transatlantic optical communication that replaced the existing electrical communication scheme, but this time on a chip-scale!

In this work, we contribute to current research by developing and studying nanolasers, which are set to play an integral role as components of future on-chip interconnects.

1.1 The Energy Challenge of Information and Communication Technologies

We live in an era of phenomenal technological advancement, where the widespread adoption of information and communication technologies (ICTs), such as the internet, mobile devices, and cloud computing, has fundamentally transformed our lives. However, this level of connectivity comes with a substantial rise in energy consumption, which has a notable impact on the global energy demand and the environment. Furthermore, the number of internet users is estimated at 66% of the global population and is proliferating,[1] while novel disruptive, but power-hungry technologies are emerging rapidly, like the Internet of Things,[2] and artificial intelligence.[3] Hence, widely cited energy forecasts suggest that global electricity demand for the ICT sector will accelerate in this decade.[4]

In the center of ICT technologies and the internet lie the *data centers*, gigantic clusters of servers and memory banks, where data are received, stored, processed, and sent back to end-users. The global data center electricity consumption in 2021 was

estimated to be up to 320 TWh,[1] which corresponds to 1.3% of the global electricity use.[5] Regarding carbon footprint, the data centers, and data transmission networks accounted for 300 Mt CO_2 in 2020, equivalent to 0.9% of the global greenhouse gas emission.[5] Furthermore, the energy consumption of data centers can increase to 8% of the projected global demand by 2030.[6] Fig. 1.1(a) shows the energy forecast related to the ICT sector performed by Jones *et al.* in 2018 [4], suggesting an exponential increase of the energy demand in data centers. While the data transmission outside the data centers is done via ultra-low loss optical communications, the traffic within the data centers is the bottleneck, accounting for up to 77% of the power consumption.[7] Hence, the fundamental problem is reduced to minimizing power consumption and heat generation on computer chips.

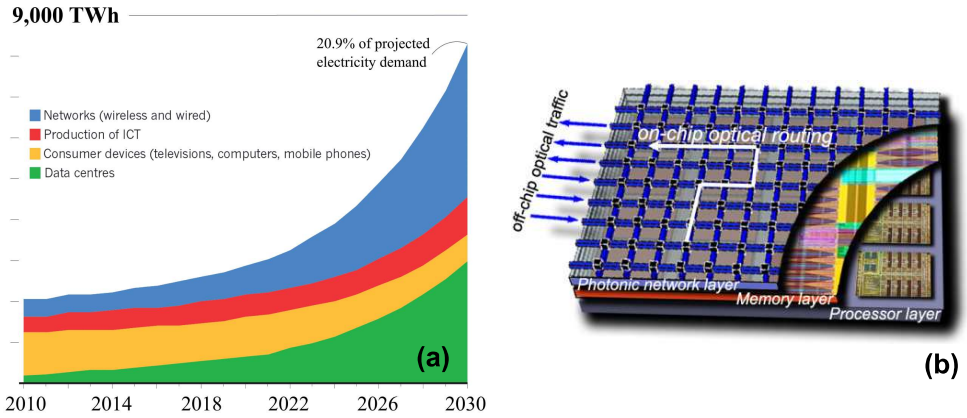

Figure 1.1 | Data centers and optical interconnects. (a) Energy forecast for global electricity demand from information and communication technologies (Adapted from [4]). (b) IBM vision for hybrid integration of a chip with electronic and photonic functionalities (Reprinted from [8]).

On-chip Communication

From the start of the semiconductor revolution of the 21st century, the efficiency and computational power of computer chips has been rising following Moore's law.[2] The efficiency of the miniaturization of transistors is reaching its fundamental limit, bound to a few tens of atoms below which quantum effects will undermine their deterministic operation. Furthermore, there is a speed limit on the transistor's switching time, and on the propagation of electrical signals over the chip, before excessive heat dissipation limit the processor's performance. Hence, the maximum clock rates have converged

[1] Exluding the energy used in cryptocurrency mining that is estimated to another 140 TWh.

[2] Moore's law is the empirical observation that the number of transistors on dense integrated circuits doubles every two years, which leads to the increased performance of modern chips.

to a few GHz since 2004, while the computations have been parallelized using multiple processor cores.[9]

Using novel lithographic processes has reduced the size of transistors and thus, the energy cost per logic gate operation. In particular, typical logic gates' operating energies are ∼3 fJ,[10] while a reduced capacitance and leakage currents can decrease this number by one to two orders of magnitude.[11],[12] The main contributor to the chips' energy consumption, however, stems from the electrical interconnects that are used to transmit information between the different chip components. In particular, a study from Intel in 2006 showed that over 50% of the total power consumption on the chip comes from the electrical interconnects.[13] The electrical interconnects comprise electrical wires, where the communication energy is bound by the line capacitance. The energy cost to transmit a bit using electrical interconnects are orders of magnitude higher than the cost of generating a bit via logical operations, exhibiting ∼600 fJ/bit to ∼5 pJ/bit for on-chip and off-chip communication, respectively.[14] Finally, the electrical interconnect density is capped by the resistance increase as the electrical wires get smaller, reducing the signal integrity and increasing the ohmic losses. An effective resolution for this challenge is to employ optical interconnects on the chip and motherboard scale, in analogy to the introduction of optical fiber technology for long-distance communications.

1.2 Optical Interconnects and Nanolasers

In contradistinction to electrons, photons are ideal candidates for low-loss communication since they interact weakly with matter and can propagate over long distances with minimal absorption and signal distortion.[3] Hence, replacing conventional electrical interconnects with novel optical interconnects is a focal point for research in academia and industry alike.[15] In Fig. 1.1(b) a schematic of a hybrid electronic-photonic chip is depicted as was envisioned by IBM in 2006.[8] Except for the low propagation losses, optical interconnects have several other advantages, including very high density, high bandwidth, and precise clocking.[14] Co-packaging of Si photonics and electronics for off-chip communication have been already demonstrated by multiple big tech players, including Intel, NVIDIA, and Cisco.[15],[16]

Significant steps have been also taken towards the hybrid electronic-photonic integration facilitating on-chip optical links. Notably, Chen Sun *et al.* demonstrated in 2015 [17] the first hybrid electronic-photonic central processing unit (CPU) with 70 million transistors and 850 photonic components. Further research was conducted by Atabaki *et al.* in 2018 [18] where they also co-integrated photonics and nanoelectronics on a single chip demonstrating high data rates and low power consumption. In both cases, however, the photonic integrated circuit relied on an external off-chip

[3] More precisely, material platforms exist where low-loss optical waveguides can be realized. Today's standard silicon-on-insulator (SOI) waveguides exhibit low propagation losses in the order of 0.1 to 1 dB/cm at telecom wavelengths ranging from 1.3 to 1.55 µm.

continuous-wave (CW) laser to provide the optical signal that was coupled and modulated via the passive optical components of the chip.

One of the most critical challenges for realizing optical interconnects is the integration of light sources on Si photonics chips. In particular, no semiconductor material is simultaneously efficient in light generation and compatible with the mature complementary metal-oxide-semiconductor (CMOS) technology. As a result, significant efforts are focused on the co-integration of optically active materials on Si substrates, like heterogeneous integration,[19] transfer printing,[20] and monolithic integration. While monolithic integration still needs further research to realize its potential, the heterogeneous integration of III-V-based lasers on Si is a relatively mature technology that uses wafer bonding or flip-chip methods. An extensive review of the different integration methods of III-V materials on Si can be found in [19].

The commercial potential of a particular optical interconnect technology depends on the energy cost for each transmitted bit, which reads as:

$$\text{Energy per bit} = \frac{\text{Input Power}}{\text{Data Rate}} \tag{1.1}$$

One of the key objectives for the new generation of interconnects is to achieve a total energy cost of around 10 fJ/bit.[14] The total energy per bit is calculated based on the power consumption of all the components required in the transmission process, i.e., the laser, modulator, and photodetectors. Compared to transmitters based on CW lasers integrated with external modulators, transmitters based on directly-modulated lasers are cost-effective for short-distance communication.[21] The power consumption of a laser is $P_{in} = IV$, where I is the injection current and V the applied bias, while the data rate is dependent on the modulation frequency. The laser wall-plug efficiency and modulation bandwidth depend on the injected current and, more specifically, the injected current above the laser threshold. To achieve the required energy cost per bit, developing ultra-compact lasers operated at currents in the order of a few µA is needed.

Miniaturization of Semiconductor Lasers

Achieving lasers with ultra-low operating energy requires the miniaturization of the active region while maintaining strong spatial confinement of the light. Thus, significant research and development have been centered around building ultra-compact lasers. Fig. 1.2 depicts the historical evolution of the threshold for different types of semiconductor lasers, where an exponential reduction of the threshold follows all the recent achievements in the field.

Distributed feedback lasers (DFBs) were among the first diode lasers to be developed.[48] They are massively employed for telecom applications due to their high efficiency. However, the weak optical confinement of DFBs poses a lower limit to the active material size, and the laser threshold has saturated to a few mA. Recently, membrane-based lasers featuring a distributed reflector (DR) have lifted this

limit since the high index contrast enables the required optical confinement for lasing using tens of microns long active regions.[35],[36] DR lasers have already achieved threshold currents in the order of a few hundred µA and moderate modulation frequencies and are strong candidates for inter-chip communication.[37] Vertical cavity surface emitting lasers (VCSELs) are also a mature technology showcasing exceptional performance. VCSELs are industry-leading devices for short-distance datacom applications.[49] Although reducing the laser threshold in VCSELs is possible,[31] vertical emission is not preferable for computer-com applications, where the coupling losses should be minimal.

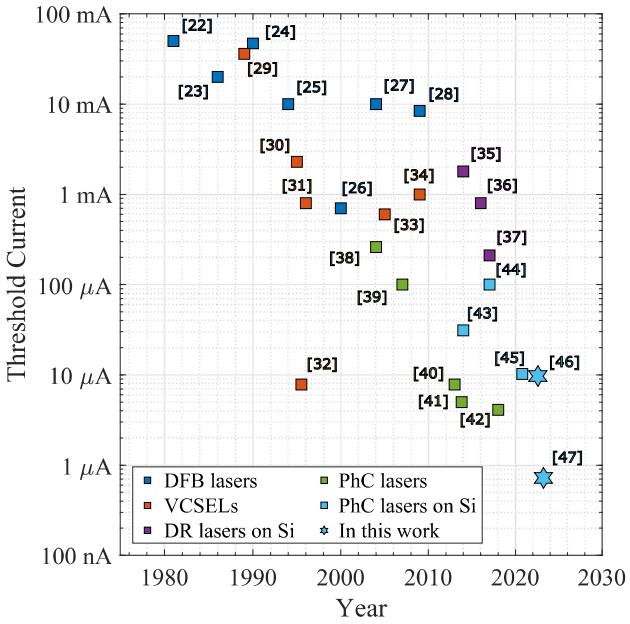

Figure 1.2 | Historical evolution of the threshold of semiconductor lasers.

This problem can be addressed using in-plane photonic crystal (PhC) nanolasers exhibiting strong spatial and temporal light confinement. The first demonstration of a PhC laser was performed by Akahane *et al.* in 2003 [50], and since then, optically-pumped PhC lasers have achieved estimated absorbed power at threshold of a few-µW,[51],[52] and sub-µW.[53] For electrically-pumped PhC lasers, the required metals and dopants will introduce additional optical losses increasing the laser threshold; thus, the lowest thresholds for electrically-driven PhC lasers on the InP and InP-on-Si platforms have converged to around 4 µA,[40]–[42],[54] and 10 µA,[43],[45],[46] respectively. Due to their low power consumption, lasers are among the most promising candidates for on-chip, and off-chip optical interconnects. During this work, additional contributions were made to developing ultra-low threshold InP-on-Si PhC lasers,[46] and demonstrating sub-μA threshold currents.[47]

1.3 Photonic Crystal Lasers

Lasers have transformed today's technology and are so common in our modern lifestyle that many forget that the word *laser* is actually an acronym for light amplification by stimulated emission of radiation. A laser consists of a gain medium that amplifies light, an optical feedback mechanism to circulate the photons, and a pumping mechanism to provide the energy in the system.

In a simple picture, a beam of light propagates through the gain medium, consisting of a material capable of amplifying the light via stimulated emission. The propagating photons can interact with the medium via stimulated emission events generating clone photons, and thus high-intensity coherent light is generated. A pumping mechanism is required to provide energy in the system, which is usually done via electrical contacts that provides carriers via a flow of electrons and holes; or an optical pump, where photons of higher energy excite the active material. An optical cavity is employed to enable multiple passes through the gain medium. The cavity can be thought of as two parallel mirrors, one partially transmitting, so useful light can be extracted.

Since the first semiconductor laser demonstration by Robert Hall *et al.* in 1962 [55], there have been significant developments in the semiconductor technology of photonic devices. These technological achievements include the development of novel high-quality gain media like strained-quantum wells and efficient p-i-n junctions that are essential building blocks of our PhC lasers. For the introduction to this work, we will focus on the most exotic element of these lasers, which is the optical resonator formed by the nanostructure called *Photonic Crystal*, and the most common gain media and pumping mechanisms used in photonic crystal lasers.

1.3.1 Photonic Crystal Cavities

The Photonic Crystal

Photonic crystals (PhC) are optical structures composed of periodic wavelength-scale refractive index changes. The periodicity of the refractive index affects the propagation of electromagnetic waves, similar to the propagation of electrons in a periodic potential, e.g., a crystal lattice. As a result, PhC structures can feature a photonic bandgap, i.e., a spectral range where no light can exist. This direct analogy to an electronic bandstructure of a solid crystal led Yablonovitch *et al.* [56] to name this structure a *Photonic Crystal* in their seminal work in 1989. In the following decades, PhCs have been studied extensively due to their rich physics and potential applications that rely on molding the flow of light, as was brilliantly put in the title of Joannopoulos *et al.* textbook [57], in which the established PhC theory is documented.

This work focuses on PhC cavity lasers, where the PhC structure is made of a

2D triangular PhC slab, which from now on, we will call PhC or PhC membrane.[4] PhC membrane structures are compatible with conventional planar semiconductor processing and are suitable for monolithic or heterogeneous integration.[58] The PhC membranes described in the thesis consist of low-index air holes periodically etched in a high-index dielectric material; a schematic diagram of the PhC membranes is illustrated in Fig. 1.3(a). The triangular PhC structure forms a TE-like bandgap for light propagating in-plane. The light is confined in the membrane via total internal reflection at the top and bottom slab-air interfaces. In other words, light whosei n-plane wave vector lies within the light cone is not confined in the membrane; this condition can be expressed as $k_{||} < (\omega/c)$, where $k_{||}$ is the in-plane wave vector component, ω the angular frequency of light, and c is the speed of light in the surrounding low-index medium. Fig. 1.3(b) depicts the bandstructure of a triangular PhC hole slab. The bandstructure of the TE-like and TM-like modes are drawn in red and blue respectively,[5] while the light cone region is painted purple.

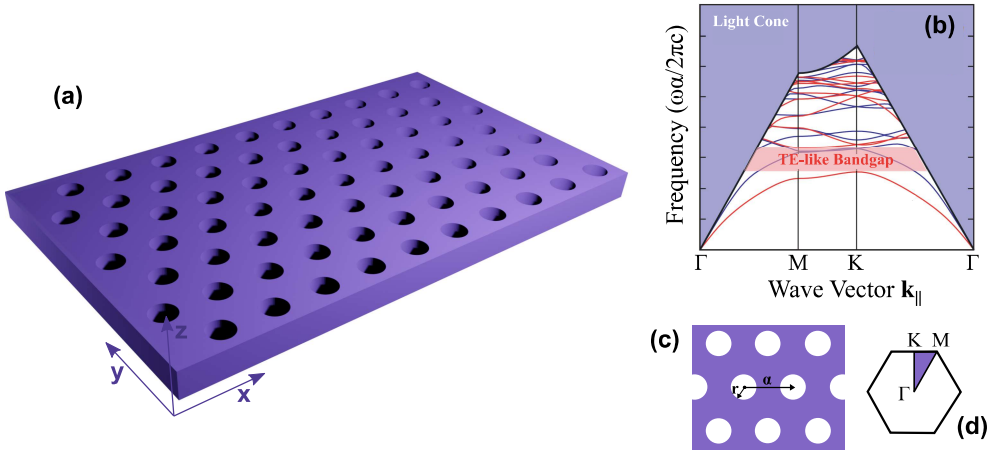

Figure 1.3 | Photonic crystal slab. (a) Render of a triangular PhC hole slab. (b) The bandstructure of the triangular PhC slab exhibiting a TE-like bandgap (Reprinted from [57]). The bandstructure of the TE-like and TM-like modes are drawn in red and blue lines, respectively; the purple region represents the light cone. (c) The top-view of a triangular PhC lattice in real space; a and r represent the PhC lattice constant and the hole radius, respectively. (d) The Brillouin zone of the reciprocal lattice; the purple painted area represents the irreducible Brillouin zone.

A top-view sketch of the PhC structure is shown in Fig. 1.3(c). The properties of the PhC structure are defined by the PhC lattice constant and the PhC hole radius.

[4] It is common to refer to 2D-PhC membranes as 2.5D-PhC to differentiate them from a vertically-infinite 2D-PhC structure. In this work, we stick to the *2D-PhC* naming, always implying the membrane effect.

[5] The TE-like modes are defined as modes where the electric field is predominantly lies within the membrane, while for TM-like modes, the electric field is orthogonal to the membrane.

Similarly, the PhC structure is transformed to the reciprocal space that can be reduced to the first Brillouin zone as shown in Fig. 1.3(d). Due to symmetry conditions, the Brillouin zone can be further reduced to the Irreducible Brillouin Zone (painted in purple).

Photonic Crystal Cavities

Any perturbation in the PhC structure will break the periodicity of the PhC structure locally, introducing discrete cavity modes that lie within the bandgap. PhC cavities can achieve strong spatial and temporal confinement of the photons featuring wavelength-scale mode volumes (V) with high Q-factors (Q). The high Q/V ratio is a known figure of merit for the light-matter interaction strength and is also related to enhancing the spontaneous emission rate via the Purcell factor.[59],[60] Therefore, PhC cavities are a central component of quantum optical systems,[61] lasers,[62] and are a favorable platform for on-chip communication.[63]

Point Defect cavities: The simplest form of such a cavity is the point defect cavity, where a *defect* is defined as the absence of a hole. Point-defect cavities are typically referred to as Hn PhC cavities, where n is the number of the missing air-holes; Fig. 1.4(a) depicts an H1 cavity.[64] Each PhC cavity supports a number of resonant modes. The total number of modes, and typical mode volumes and Q-factor rise as a function of the cavity length; the modal spacing decrease with cavity length, although, unlike the conventional Fabry-Pérot cavity modes, the modes of a PhC cavity are not spectrally equidistant.[65] The Q-factor of a mode depends on the radiation losses from the field components within the light cone and is defined as $Q = \omega/\Delta\omega$, where ω is the angular frequency of the mode, and $\Delta\omega$ is its corresponding resonance width that is associated with the optical energy decay rate. Careful modifications in the position and size of the holes adjacent to the cavity can minimize the out-of-plane radiation since abrupt termination of the field distribution in real-space leads to broadening in the k-space.[50],[66] By shifting the holes away from the cavity center, high Q-factors beyond 100,000 can be achieved at wavelength-scale mode volumes.[67] This technique is also highlighted in 1.4(a), where the red-painted holes are shifted radially to the defect.

Line Defect cavities: The same principles are extended to a line defect (LD) cavity, where several air holes are removed in succession along a line. The line defect cavities are typically referred to as Ln cavities, following the same nomenclature as the Hn cavities. Fig. 1.4(b) illustrates an L3 cavity, where three holes are removed along the K-Γ direction.[68] For this cavity, the optical mode resembles an optical wave traveling along the line-defect being reflected at the first mirror holes.[65] The same Q-factor optimization strategies apply in the LD cavity case, where adjusting the first few mirror-holes is enough to increase the Q-factor drastically.[50],[68],[69] However, achieving ultra-high Q-factor is increasingly complex, and more sophisticated

optimization methods are needed than just shifting the terminating mirror-holes away from the cavity center.[6] An extension to the LD cavity is a non-terminating LD, where light propagates along the defect, also known as a W1 waveguide. Slight changes in the surrounding rows of PhC holes can greatly affect the waveguide dispersion, which can be tailored to match specific application requirements.[70],[71]

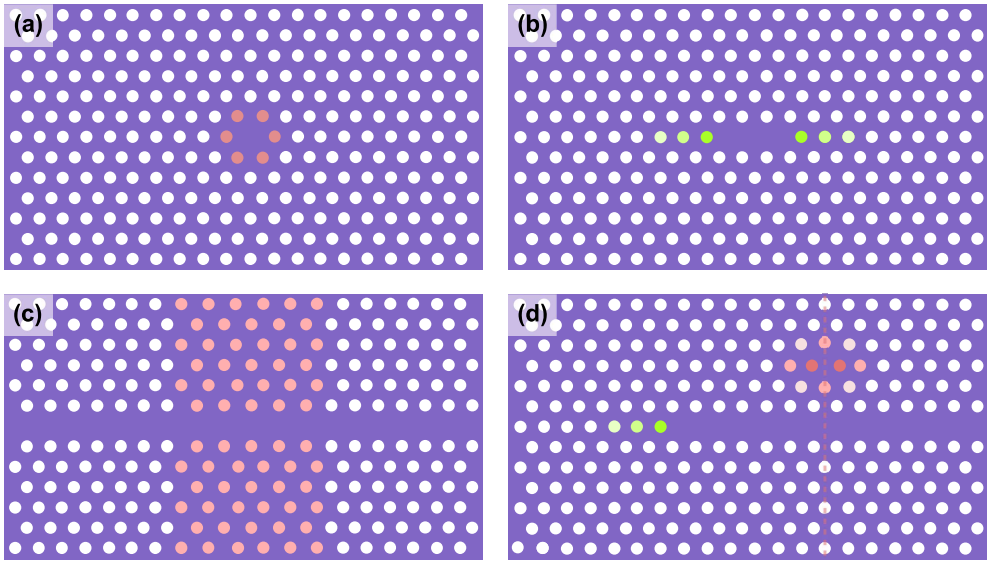

Figure 1.4 | Photonic crystal cavities. (a) A H1 point-defect PhC cavity. (b) An L3 line-defect PhC cavity. (c) A double-heterostructure PhC cavity. (d) A Fano PhC cavity based on an H0 nanocavity.

Double-heterostructure cavities: A different type of PhC cavity is the double-heterostructure cavity displayed in Fig. in 1.4(c). This cavity was first introduced by Song *et al.* in 2005;[72] the cavity is realized by locally altering the lattice constant of the PhC, that in turn changes the bandgap and the dispersion of the waveguide. Due to the mode gap difference of the guiding modes, an optical cavity is created. The spatial modulation of the mode-gap edge produces strong light confinement since the electric field change in real space is more gradual than the typical waveguide termination found in L*n* cavities. Using the *modulated mode-gap* cavity formation principle, ultra-high Q-factor cavities have been demonstrated.[73]–[75] Similar mode-gap modulation cavities can be realized via local waveguide width modification,[76]–[78] or local change of the refractive index using a buried-heterostructure active region. The latter example is especially relevant for PhC lasers, as it is the optical confinement principle behind the lambda-scale embedded active-region (LEAP) PhC lasers developed in the Nippon Telegraph and Telephone (NTT) Laboratories.[40],[43],[45],[79]–[82] Although the

[6] Details on these Q-factor optimization techniques are provided in Sec. 5.3.

Q-factor of the LEAP laser cavity is expected to be between a few hundred thousands to a few million at transparency,[51],[82] the LEAP cavity cannot be decoupled from the active material, whose refractive index and absorption coefficient is dependent on the carrier density. Therefore, no independent Q-factor measurement of the optical mode can be performed. An advantage of the LEAP laser cavity design is that electrical isolation trenches can be incorporated in the LD waveguide without a significant decrease in the Q-factor,[40],[43] although the most recent designs no longer include this element.[45],[54],[83]

PhC Fano cavities: Finally, the most exotic type of 2D PhC cavity is the *Fano* cavity based on the homonymous resonance type. A Fano resonance is a general physical phenomenon resulting from the interference of a discrete mode with a continuum of modes initially found and named after the physicist Ugo Fano.[84] The characteristic asymmetric Fano lineshape finds many uses in photonic devices,[85] like compact, low-power optical switches.[86]–[88]

The Fano spectral response can also be utilized in lasers to form a mirror. Such a nanophotonic system was proposed in 2014 by Mørk *et al.* [89] at the Technical University of Denmark (DTU). The Fano laser cavity comprises a line-defect waveguide and two different mirrors; a standard PhC mirror formed by the termination of the waveguide and the Fano mirror formed by a nanocavity side-coupled to the open end of the waveguide as illustrated in Fig. 1.4(d). Suppose that light propagates in the waveguide; if its frequency matches that of the nanocavity mode, the light will be partially coupled to the nanocavity. The reflectivity of the Fano mirror stems from the destructive interference of the light coupled out from the nanocavity and the light transmitted through the waveguide.

The Fano mirror is narrowband and highly dispersive, enhancing its laser properties and offering unique control possibilities previously unattainable for compact on-chip sources. In particular, a Fano Laser (FL) can be modulated using the nanocavity at THz speeds, not bound by the relaxation oscillation of the carriers,,[89] while its frequency modulation bandwidth is only limited by the nanocavity response[90] Furthermore, it is predicted to be robust against feedback-induced instabilities,[91] a property crucial for on-chip sources since compact integrated optical isolators have yet to be developed. In 2017, the first FL was experimentally realized [92], exhibiting single-mode operation and self-pulsing at the GHz frequency range as the nanocavity acted as a saturable absorber.[90] With the development of the BH technology, the active material could be localized in the LD waveguide, and a new generation of Fano Lasers was realized.[93] Such lasers exhibited ultra-coherent properties with a linewidth in the few MHz range - an order of magnitude reduction compared to conventional PhC lasers - due to frequency dependent reflectivity of the Fano mirror, counteracting the phase diffusion induced by spontaneous emission events that occur in the active region. Finally, the same system was used to demonstrate cavity damping by modulating the resonance of the nanocavity, attaining an order of magnitude peak power increase compared to conventional gain switching employed

in microscopic lasers.[94]

The Fano laser is a general type of lasers whose cavity comprises one (or more) characteristic Fano mirrors. Thus, any discrete optical mode can be utilized if the right conditions are met.[95] Although, the most popular Fano Laser designs from our group are 2D PhC lasers featuring an H0 or an L7 cavity, the general Fano-mirror principle has been extended to nanobeam cavities as well.[96]

1.3.2 Gain Media

The gain medium provides the optical gain in the laser. Due to energy and momentum conservation, high-probability spontaneous and stimulation emission events require a direct bandgap semiconductor material.[97] This limits the semiconductor material systems that can be used as photon sources.[7] The most common semiconductor photon sources are based on III-V semiconductors, which consists of Group III (Ga, In, Al) and Group V (As, P, Sb, N) elements forming a family of composite materials. By combining two or more III-V elements, the bandgap of the composite crystal can be tailored, tuning the emitted photons to match specific applications. Notable examples of the broad tunability of the III-V materials include the AlGaN deep-ultra-violet light emitting diodes (LEDs),[98] the Nobel Prize-winning GaN-based blue LEDs,[99] the InGaAs-based single-photon sources for quantum applications,[100] and the VCSELs for short-haul communications,[101] to the InGaAsP-based DFB lasers used for long-haul fiber communication.[48] In this project, we are interested in the long-wavelength optical communication regime around 1.55 µm.

The performance of semiconductor light sources, and more importantly, lasers, have been drastically improved with heterostructure gain media, where a lower bandgap material is sandwiched between higher bandgap materials confining the charge carriers. Creating a nanometer-scale heterostructure reduces the translational degrees of freedom of the carriers leading to an increased density of states near the edges of the conduction and valence sub-bands. As a result, population inversion can be achieved at reduced carrier densities, leading to efficient low-threshold lasers. By reducing the thickness of a double-heterostructure down to a few nanometers, a quantum-well (QW) structure can be created where the carriers are confined in 2D. The 2D confinement drastically changes the density of energy states exhibiting a step-like shape, enabling population inversion at a lower carrier density. The QW-based gain region can be further optimized by deliberately introducing compressive or tensile strain during the epitaxial growth.[102] Strain can reduce the density of states in the valence band, further reducing the carrier density required to reach population inversion. Furthermore, strain breaks the symmetry of the crystal and allows the manipulation of the polarization of the carriers' orbitals, so they mainly recombine into the polar-

[7] The most notrable example of an indirect bandgap semiconductor is silicon, whose poor optical properties drive the research and development of heterogeneous integration of direct bandgap materials on Si.

ization of the optical mode. Quantum wells are a mature technology and are the industry's standard for lasers and LEDs.

Further reduction of the dimensionality includes quantum wires, where the carriers are confined in 1D,[103] and quantum dots (QDs), where the carriers are confined in all three dimensions (0D). Although quantum wires are not commonly used, QDs have garnered significant attention due to their atom-like electronic structure, making them ideal quantum sources,[104],[105] and optical gain media for lasers.[106] QD-based gain materials have many desirable properties for lasing. Firstly, QDs can achieve population inversion at lower current densities than QWs due to the narrow δ-like density of states. In addition, the lack of higher energy states makes QD lasers less sensitive to temperature than the QW lasers,[107],[108] thus, QD-based lasers are strong candidates for high-speed modulation.[109]

1.3.3 Electrical Pumping

In order to achieve population inversion in a laser, a pumping mechanism is necessary. Optical and electrical pumping are the two most widely used methods in semiconductor lasers. Optical pumping uses a light source to excite carriers to the conduction band but is not practical for on-chip optical communications. On the other hand, electrical pumping involves the injection of charge carriers in the active region via a type of p-n junction. For brevity, only the p-i-n junction will be discussed here since it is the type of junction used in PhC lasers. P-i-n junction is a heterostructure where an intrinsic semiconductor region is sandwiched between a p-doped and an n-doped region. The addition of the intrinsic region reduces the carrier-induced losses in the optical cavity and lowers the capacity allowing for faster switching.

Vertical carrier injection (VCI) is the most conventional type of injection, and it is enabled by vertical doping performed during the epitaxial growth of the wafer. In this scheme, the layers below the active region are p-doped while the above layer is n-doped. In 2004, Hong-Gyu Park *et al.* [38] demonstrated the first electrically-driven PhC laser using VCI, where a p-doped nano-post is used to inject the holes in the QWs. The PhC laser was based on an H1 cavity formed on an p-i-n InGaAsP slab supported by a p-InP nano-post formed via selective HCl wet etching.[110] A render of the H1 laser is depicted in Fig. 1.5(a). Since then, a similar process has been used for optimized 2D PhC[39] and 1D PhC nanobeam lasers.[41] Fig. 1.5(b) shows the schematic diagram of the nanobeam laser featuring a VCI scheme with a nano-post. By shrinking the diameter of the nano-post, the carrier injection can be focused on a narrow region whose dimensions are limited by the current diffusion. As a result, the population-inverted region can be tailored to overlap with the optical cavity maximally, and an ultra-low-threshold current down to 5 mu has been demonstrated.[41] Similarly, VCI was used by Cronsier *et al.* [44] in 2017 on a nanobeam laser based on the InP-on-Si platform using an intricate junction design without the need of a nano-post. A bird's eye view and a cross-sectional view of the laser are shown in Fig. 1.5. This PhC laser design exhibits the highest wall-plug efficiency to date, suggesting a high electrical

injection efficiency; however, the threshold current is 100 µA, since the doping profile and the active region size is coupled to the nanobeam cavity.

A more versatile pumping scheme is the lateral carrier injection (LCI) enabled by a lateral p-i-n heterostructure. For this scheme, the p- and n-doped regions can be created using a multiple regrowth process,[111] or via ion implantation.[82],[112] Using a multiple regrowth processes complicates the process since wafer planarization for retaining high quality factor cavities is required.[21] Furthermore, the quality of the regrowth interfaces between the cladding layers and the active region might affect the electrical characteristics by an excessive voltage drop and the optical characteristics by surface recombination.[58] As a result, ion implantation is the process used for lateral doping of PhC lasers.

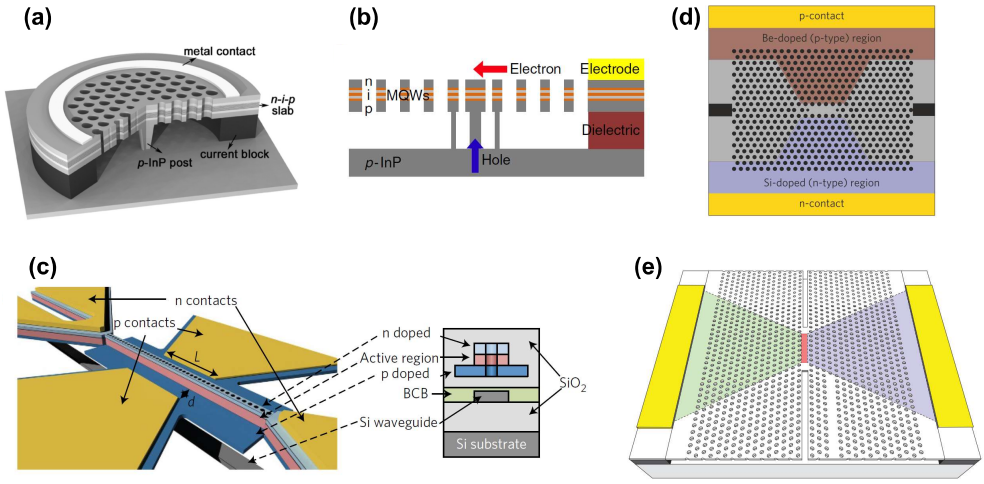

Figure 1.5 | Electrical pumping schemes for photonic crystal lasers. (a) VCI-based H1 laser featuring a p-doped nano-post (Reprinted from [110]) (b) A VCI-based nanobeam cavity laser featuring a nano-post. (c) Vertical carrier injection on an InP-on-Si nanobeam laser (Reprinted from [44]) (d) A laterally doped PhC laser based on a GaAs membrane embedded with InAs QDs (Reprinted from [112]). (d) A laterally doped PhC laser featuring a buried-heterostructure active region of InGaAsP-based QWs (Reprinted from [40]).

The first LCI-based PhC laser was demonstrated by Ellis *et al.* [112], and its schematic diagram is depicted in Fig. 1.5(d). The laser is based on a uniform QD membrane, where Be and Si ion implantation was used for defining the p- and n-doped regions, respectively. However, lasing was observed only at cryogenic temperatures.[8]

Finally, LCI on a wafer featuring a buried-heterostructure (BH) active region was established by NTT on both InP[40],[82] and InP-on-Si platforms.[43],[45] These

[8] A conclusion about the inherent efficiency of the lateral doping on an all-active membrane cannot be drawn, since the cryogenic-lasing might be also related to the high current leakage current through the substrate,[82] the high density p-doping adding to the optical losses, the quality of the InAs QDs affecting the gain, and the excessive non-radiative recombinations of GaAs.[113]

PhC lasers comprise InGaAsP-based QWs, and the lateral p- and n-doped regions are fabricated using Zn thermal diffusion and Si ion implantation. The schematic diagram of a LEAP laser is shown in Fig. 1.5(e). The LCI scheme with the lateral confinement of the carriers in the BH has demonstrated ultra-low threshold lasing in continuous-wave at room temperature operation and ultra-low energy consumption of 1 fJ/bit has been reported.[54]

Numerical simulations performed by Lupi *et al.* [114] suggest that lateral injection on a uniform active membrane is more efficient than vertical injection via a post. However, successful lasing at room temperature for 2D PhC lasers fabricated on a uniform active membrane has yet to be demonstrated to the author's knowledge. Finally, the lateral injection system using a BH region was found to be the most efficient scheme.

1.4 Thesis Outline

This work aims to contribute to the field of photonic crystal lasers. In particular, the main goal is the demonstration of electrically-driven PhC nanolasers and to provide a deeper understanding of their physical properties. The realization of such devices required extensive development and optimization of nanofabrication processing. This PhD project was mostly focused on the design and characterization of PhC lasers and PhC cavities intended for laser applications; however, significant time was also spent on processing and micro-scale characterization.

The thesis can be grouped into three main sections: Chapters 2-4 are introductory chapters establishing the experimental and numerical methods in terms of fabrication, characterization, and modeling, Chapters 6-7 describe distinct groups of investigations in terms of PhC lasers, while Chapter 9 provides a conclusion. In particular:

Chapter 2 provides an overview of the PhC laser devices and the nanofabrication process flow. The current limitations of the fabrication process, like the quality of PhC holes, the doping, and the BH, are discussed.

Chapter 3 lists the different optical characterization methods used throughout the thesis. In particular, the laser characterization setup and the Q-factor characterization setup are discussed in detail. The modifications to the laser characterization setup to incorporate optical pumping and Radio-Frequency measurements are explained. Furthermore, data acquisition, data analysis, and setup limitations are discussed.

Chapter 4 provides the necessary theory on laser physics to understand the conventional rate equations used for modeling the laser behavior and the small-signal analysis. Additionally, details on the electromagnetic finite-difference in time-domain simulations are given.

Chapter 5 summarizes the numerical and experimental results on PhC cavities. Special focus is given to the robustness of the design under different systematic and random variations of the PhC constituents. A method for visualizing the leaky field profiles is also explained in detail, enabling the Q-factor optimization of PhC cavities utilized throughout the project. Furthermore, the effect of disorder and doping on the Q-factor is experimentally quantified.

Chapter 6 is where the main characteristics of the electrically-driven PhC lasers are discussed. In particular, the static and thermal properties are investigated. Furthermore, we shed light on the injection efficiency and the leakage current by comparing optical and electrical pumping and electroluminescent measurements.

Chapter 7 investigates the properties of the PhC lasers under varying lengths of the active region placed in a fixed L7 cavity. First, FDTD simulations are used to extract the confinement factor and the modal losses, while the effective index of the buried-heterostructure is identified using experimental data. An investigation on the laser threshold is also conducted, and the first sub-μA nanolaser is demonstrated. Finally, a small-signal analysis is conducted on the lasers to understand the modulation efficiency, the dumping, and the energy cost per bit.

Chapter 8 is a bonus chapter dedicated to the demonstration of electrically-driven Fano Lasers. This chapter establishes the basic understanding of the Fano cavity design parameters via FDTD simulations, focusing on the effect of the BH refractive index and the doping. Furthermore, a characterization of the Q-factor of the Fano mode is performed. Finally, the electrically-driven Fano lasers are demonstrated.

Chapter 9 concludes the PhD thesis putting the main results into perspective while further possibilities are discussed.

1.4.1 Contributions

The fabrication process of electrically-driven PhC membrane lasers is highly complex and poses a major experimental challenge. The successful demonstration of electrical pumping was one of the main goals of the NATEC center and was realized by the work of multiple smart and hardworking colleagues, both cleanroom specialists and generalists. Most notably, Aurimas Sakanas developed the InP-on-Si bonding and the BH technology,[115] Andrey Marchevsky developed the lateral doping technology,[116] and Meng Xiong optimized the processes related to the PhC pattern formation.

The PhC lasers fall under the umbrella of the more general HERO project, in which both active and passive devices were fabricated on InP-on-Si wafers. Weekly meetings were held, where results and collective decisions on the mask and the process flow were made. As a result, special thanks go to Kristoffer Mathiesen,[117] Dagmawi Bekele,[118] and Quentin Saudan[119] who contributed to the cleanroom work, but

more importantly for their contribution via the various characterization methods that provided crucial feedback used in the optimization of the fabrication process.

Apart from the immediate HERO team, Kresten Yvind was the leader of the HERO nanofabrication team and also a supervisor of this PhD project, while Elizaveta Semenova supervised the epitaxial growth of the wafers. Finally, Jesper Mørk and Yi Yu also contributed via discussions, new ideas, and the supervision of this PhD project.

CHAPTER 2

Laser Design and Nanofabrication

This chapter gives a general overview and describes the fabrication of electrically-driven photonic crystal lasers and passive photonic crystal cavities and their characterization. A brief introduction to the fabrication process and the current limitations is given.

2.1 Device Overview

The PhC laser devices described in this work are based on a 250 nm air-suspended InP PhC membrane directly bonded on a SiO_2/Si wafer.[120] A buried-heterostructure (BH) active region is employed to confine the carriers vertically and laterally, while a PhC optical cavity is used to confine the photons. The carriers are injected into the BH region using a lateral p-i-n structure. A bird's-eye view schematic diagram of an electrically-driven L3 laser is shown in Fig. 2.1(a).

The main PhC laser cavity designs considered in this work are line-defect (LD) cavities. The main advantage of the LD cavity design stems from the fact that the optical resonator can be decoupled from the active region, whose effect on the cavity properties can be largely neglected. Therefore, the optical resonator can be characterized independently and on the same chip. Fig. 2.1(b) depicts the magnetic field profile of the fundamental mode of the L3 cavity. The PhC lattice constant is 440 nm, and the hole radius is centered around 120 nm to achieve lasing at telecom wavelengths close to 1550 nm.[1]

The BH active region comprises a single 8 nm InGaAsP/InAlGaAs-based quantum well (QW), whose emission wavelength is centered around 1550 nm and has a full-width at half-maximum of 60 nm.[2] To avoid any overlap with the etched PhC holes, the BH width is chosen as 400 nm, while its length matches the length of the

[1] Sweeps of the hole radius are performed across devices for resonance tuning to compensate for the non-uniformity of the PhC membrane thickness and the process variability during InP etching.

[2] The epitaxial structure of the active region can be found in Appendix C of the PhD thesis of Aurimas Sakanas [115].

PhC cavity. The lateral injection current scheme is realized by selective Zn thermal diffusion and Si ion implantation for the p- and n-doped regions, respectively. A scanning electron micrograph (SEM) of the top-view of the laser is depicted in Fig. 2.1(c), where the p- and n-dopants can be observed. Figs.2.1(d-e) illustrate cross-sectional SEM images of the air-suspended InP/SiO_2/Si PhC membrane and the BH region, respectively.

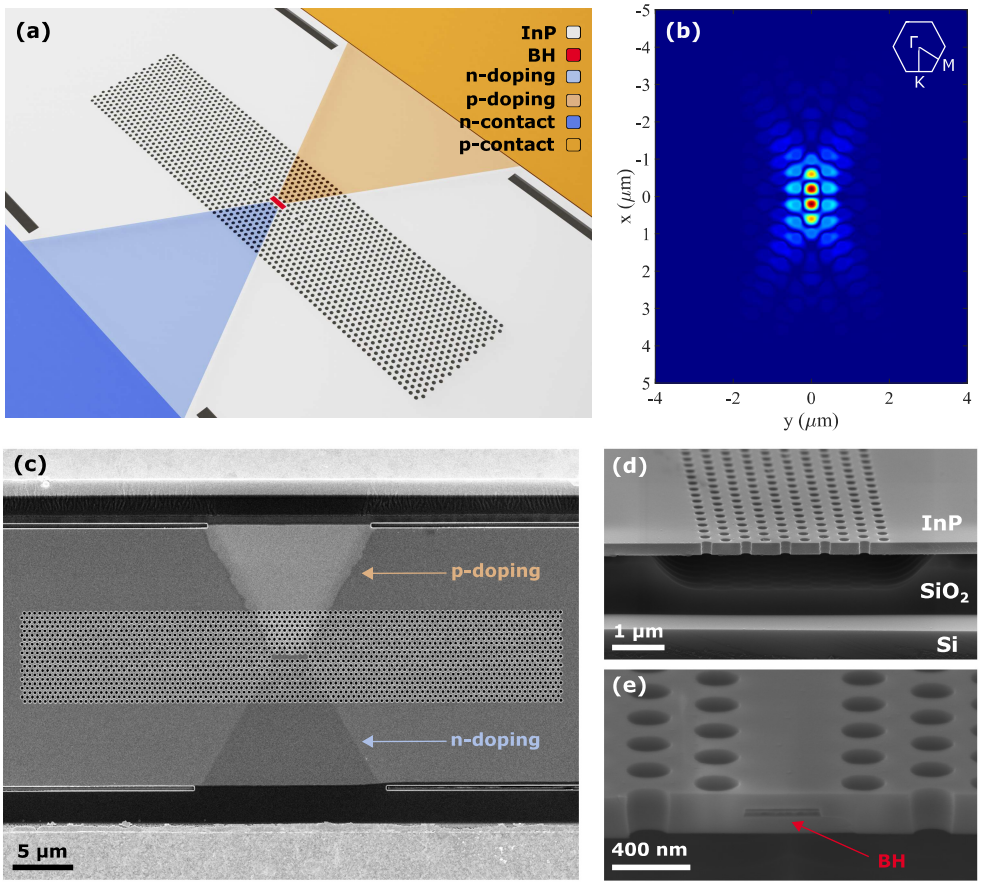

Figure 2.1 | Device overview. (a) Bird's eye view schematic diagram of an electrically-driven L3-type PhC laser. (b) Magnetic field profile of the fundamental mode of an L3 cavity. (c) SEM of the top of a PhC laser. (d) The cross-sectional SEM image of a PhC membrane. (e) The cross-sectional SEM image exhibiting the BH active region (The image is taken by Aurimas Sakanas).

2.2 NanoFabrication Process

This section gives an overview of the fabrication process of the PhC lasers. Appendix F contains the detailed step-by-step process flow.

The fabrication process starts with preparing a 2" active InP wafer and a 4" SiO2/Si wafer, as shown in Fig. 2.2(a). The InP wafer features an InGaAs etch-stop layer and InGaAsP/InAlGaAs QW layers epitaxially grown on the InP substrate via metalorganic vapor phase epitaxy (MOVPE). In a separate process, a SiO_2 thermal oxide layer of 1.1 µm is grown on the Si wafer by wet oxidation at 1100 °C.

The InP wafer is flipped and directly bonded on the SiO_2/Si wafer [Fig. 2.2(b)]. An intermediate 2 nm thick Al_2O_3 layer is deposited via atomic layer deposition (ALD) on each wafer to assist bonding.[121] The direct bonding process is done by stacking the wafers together and annealing them at 300 °C with applied pressure. The InP substrate and the InGaAs etch-stop layers are selectively removed by subsequent wet etching steps using HCl and H_2SO_4:H_2O_2:H_2O chemistry, respectively [Fig. 2.2(c)].

Consecutively, cross-shaped alignment marks are patterned on the Si substrate. Good quality alignment marks are required for patterning the BH region and the PhC holes requiring an alignment precision below 100 nm. Initially, pre-alignment openings are defined on the III-V layer using wet chemistry similar to one used for the InP substrate removal, while the openings are defined using standard UV lithography. Then, the 1.1 µm SiO_2 layer is etched via ICP dry etching with CF_4/H_2 chemistry, while the last 0.1 µm of SiO_2 is removed via wet etching using BHF not to degrade the quality of the Si beneath. Finally, the alignment marks are defined using UV lithography, and are etched on the Si substrate using ICP dry etching with SF_6/O_2 chemistry.

The BH mask is patterned via e-beam lithography on a 350 nm thick hydrogen silsesquioxane (HSQ) negative resist.[3] The exposed HSQ resist exhibits glass-like properties and acts as a hard mask during InP etching and in the following regrowth step. Mesa structures are formed by inductively-coupled plasma (ICP) reactive-ion etching (RIE) of the InP epilayers using $HBr/CH_4/Ar$ chemistry at 180 °C [Fig. 2.2(d)].

The HSQ mask is also used for the selective area regrowth of InP around the mesa structures and is then removed by HF etching after an initial plasma ashing step to strip the surface of any organic residues. The BH formation is completed after a second regrowth step for planarization, aiming for a 250 nm III-V device layer. A 50 nm lattice-matched InGaAs is also grown as a capping layer. The InGaAs layer is needed for high-quality doping since it reduces the wafer damage during doping, improves the lateral and vertical spread of the doping profile, and produces high-quality p-contacts. Both epitaxial regrowths are performed using MOVPE at 610 °C following a 15 min de-oxidation step at 650 °C.

[3] In the latest recipe, the HSQ thickness was changed to 120 nm.

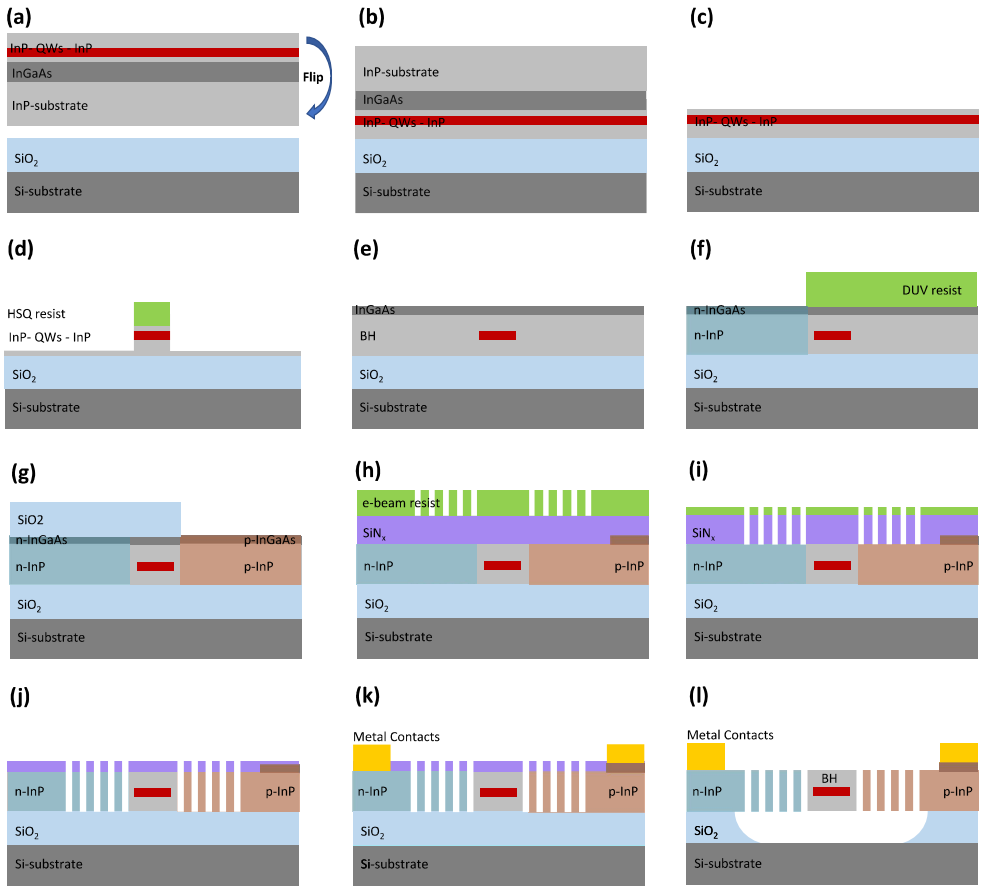

Figure 2.2 | Fabrication process of the electrically-driven PhC lasers. (a-b) The active InP wafer is flipped and directly-bonded InP wafer on Si/SiO_2 wafer. A 2 nm thick Al_2O_3 intermediate layer is deposited on the InP and Si wafers to assist bonding. (c) The InP substrate and the InGaAs etch-stop layers are removed via subsequent wet etchings. (d) HSQ-protected mesa-structures formed via e-beam lithography and dry etching. (e) A Buried-Heterostructure is formed after the second regrowth of InP. (f) Wafer after Si-ion implantation; a DUV mask is used for n-doping. (g) Wafer after Zn thermal diffusion; a glass mask is used for p-doping. (h) E-beam lithography for the PhC holes definition. (i) The e-beam mask is transferred to a SiN_x hard mask via dry etching. (j) The PhC holes are formed on the InP layer via dry etching. (k) Metallization is done via lift-off processes. (l) Membranization of PhC structures.

The n-type doping is performed using deep-ultraviolet (DUV) lithography and Si ion implantation [Fig. 2.2(f)]. The p-type doping is performed via DUV lithography and Zn diffusion. For both DUV lithography steps, a bottom anti-reflection coating of 60 nm is placed underneath the photoresist to suppress the reflection of the DUV

light from the substrate. For the p-doping, the DUV mask pattern is transferred on a SiO_2 hard mask because the Zn diffusion is done in the MOVPE tool at elevated temperatures [Fig. 2.2(g)]. The activation of the Si n-dopants is partially done during the Zn diffusion process, while rapid thermal annealing (RTA) enables the activation of the Zn p-dopants while completing the activation of the Si n-dopants.

After completing the n- and p-type doping, the InP device layer is patterned using e-beam lithography and a two-step etching process to form PhC holes, current-blocking trenches, waveguides, and grating couplers. Initially, the InGaAs capping layer is selectively removed from the wafer, except for the areas designed for the p-contacts, using wet etching. A 100 nm SiN_x hard mask is deposited using plasma-enhanced chemical vapor deposition (PECVD). Then, a 180 nm high-resolution CSAR e-beam resist is spin-coated and patterned using e-beam lithography [Fig. 2.2(h)]. The pattern is then transferred on the SiN_x by ICP etching using an $N_2/SF_6/CF_4/CH_4$ chemistry [Fig. 2.2(i)]. Finally, the pattern is transferred to InP using ICP etching at 180 °C, based on the HBr-based recipe developed for the BH etching [Fig. 2.2(j)].

The p- and n-metal contacts are formed via subsequent lift-off metallization processes [Fig. 2.2(k)]. The p- and n-contacts are fabricated on dedicated p-InGaAs/p-InP and n-InP openings of a negative photomask, respectively. The SiNx is removed from the designated openings, and the metals are deposited via e-beam evaporation. The p-contact comprises Ti/Pt/Au, and the n-contact comprises Ni/Ge/Au. Both contacts are alloyed simultaneously at the end of the metallization via RTA at 430 °C.

The final step is the membranization of the PhC layer, where the top SiNx layer and the bottom SiO_2 are selectively removed via wet HF-etching, leaving an air-suspended PhC membrane [Fig. 2.2(l)]. The etchant reaches the SiO_2 glass layer through the PhC holes. To protect the rest of the device, membranization windows are defined via UV lithography since HF can etch the Ti of the p-contacts as well as the glass beneath InP wire waveguides and PhC grating couplers.

Fabrication of passive InP PhC cavities

The process flow of passive InP PhC cavities follows similar processing steps as the electrically-driven PhC lasers; however, the fabrication complexity is significantly reduced since the selective etching and regrowth steps needed for the BH formation are not required. If the passive InP sample does not require lateral doping and metallization, the process flow is further reduced by neglecting the corresponding steps, including the formation of alignment marks on the Si substrate. A detailed process flow for the fabrication of passive PhC cavities is not explicitly described in this thesis since it is a subset of the process flow already presented.

2.3 Fabrication Limitations

In this section, the limiting factors on the laser performance that are attributed to fabrication imperfections are discussed. The author took part in multiple steps of the fabrication process; however, less time was spent on process development. The following information was mainly obtained by SEM imaging in conjunction with the optical characterization of the samples.

2.3.1 Definition of PhC holes and InP etching

The PhC structure is defined on the InP device layer using e-beam lithography and a two-step etching process as described in section 2.2. The PhC definition process is critical since the disorder of the holes is associated with increased scattering losses, and even random optical cavity formations,[122] i.e., Anderson localization. The evaluation of the etching process is typically done via SEM imaging. Fig. 2.3(a) depicts a top-view SEM image of a typical PhC lattice. The hole quality also depends on the surface roughness and the verticality of the sidewalls.

An imaging algorithm is used to detect the hole radii, and the mean value and variance are calculated. In Fig. 2.3(b), the mean fabricated PhC hole radius is plotted against the designed radius. During the PhC mask transfer process, the PhC holes are enlarged by a small factor (6-10%). The surface roughness is correlated with the standard deviation of the detected hole radii ensemble shown with the errorbars in Fig. 2.3(b); however, the surface roughness of process can be better assessed by calculating the deviation of every point on the boundary of the i^{th} PhC hole from its average hole radius $(r_i - \overline{r}_i)$. A histogram of this difference for all the holes in an SEM image is shown in 2.3(c). Such an imaging tool for etching quality testing can be useful in dedicated investigations on the disorder in PhC cavities,[123],[124] on which more experimental investigations are needed.[125],[126]

At the start of the PhD project, a 500 nm high-resolution ZEP resist (ZEP520A) was used during e-beam lithography. The pattern was transferred to a 200 nm SiNx hard mask that was etched via a standard RIE process. The InP layer was etched using a cyclic dry-etching process using CH_4/H_2 and O_2 mixtures in standard RIE. Due to the poor selectivity during etching, the thickness of the soft and hard mask layers was thick, and a large fabrication (enlargement) factor of $\sim$30% was obtained. The fabrication factor is defined as the ratio of the fabricated PhC holes' radius to the designed radius on the e-beam mask file. Due to irreproducibility issues, both etching steps were transferred to an ICP-RIE etching tool for III-V materials.

Additionally, a transition to a 180 nm CSAR (AR-P 6200.09) e-beam resist was made due to the possibility of automated handling at our cleanroom facilities, which leads to better process control, as well as its greatly reduced cost. The lithographic process was developed by the BSc students Simon Borregaard and Adrian Dubré under the supervision of the author.[127] During the last two years, the e-beam exposure was further optimized by Meng Xiong, while the SiN_x hard mask thickness was decreased to 100 nm. Finally, the ICP etching recipe for the InP layer was established

by Aurimas Sakanas during his work on the BH development,[115] and was further optimized by Meng Xiong posed to resolve the fine features of cavities designed for extreme dielectric confinement.[128]

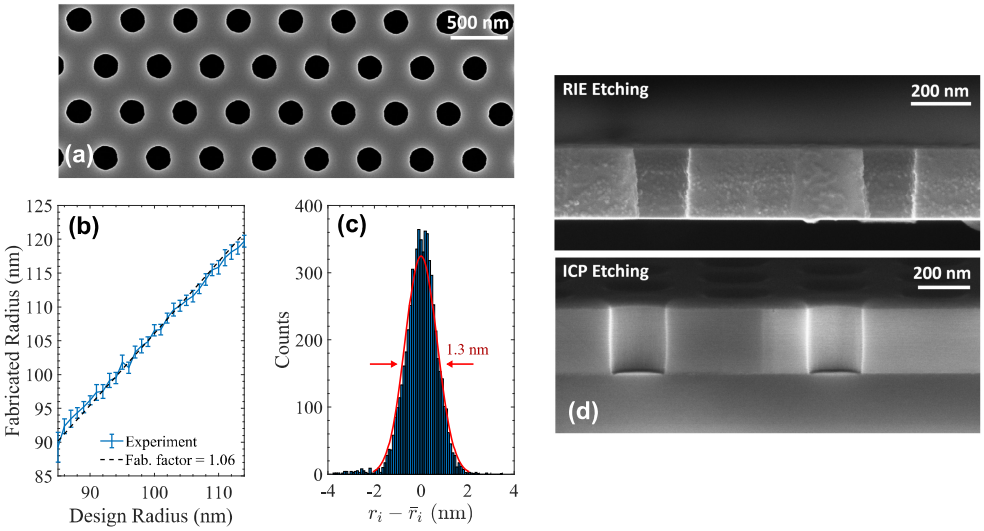

Figure 2.3 | Etching quality of PhC holes. (a) SEM picture of the PhC holes. (b) The radius of the fabricated PhC versus the designed radius used in the e-beam mask. (c) A histogram of the difference between all the radial points and the average radius of the i^{th} hole, summing over all the PhC holes captured in an SEM image. (d) A cross-sectional view of the PhC membrane etching using RIE (top) and the optimized ICP-RIE etching (bottom).

Thus, the fabrication factor was decreased to 1.06-1.1, and PhC holes with low surface roughness and good verticality were routinely fabricated. A comparison between the InP etching process is depicted in Fig. 2.3(d), where a cross-section of the device layer is shown using RIE and ICP etching, respectively.

Overall, standard PhC structures featuring ∼200 nm diameter holes have relatively relaxed requirements, and the fabrication process is stable. A notable exception is the ∼60 nm PhC holes of PhC grating couplers (see Fig. 3.5(a)), which can have irregular shapes and not well-controlled sizes.

2.3.2 Lateral Doping

The doping quality and design are critical for the laser performance defining the Q-factor of the laser cavity, the injection efficiency, and the leakage current. The p- and n-doping is performed via Zn diffusion and Si ion implantation, respectively. This section mainly considers the p-type doping that exhibits high free-carrier absorption and a bad-controlled p-i interface.

The doping profiles can be visualized with SEM as the p- and n-dopants provide enough contrast. Fig. 2.4(a_1) depicts the SEM image of a passive InP cavity.[4] For the passive InP cavity, the p-InP and n-InP doping profiles closely follow the profile of their respective DUV masks.[5] For comparison, the top view of an actual laser device featuring the same doping mask is shown in Fig. 2.4(a_2). For the laser devices, the InP is regrown during BH definition, and a lower material quality is expected, leading to a larger lateral redistribution of the dopants. The n-doping profile is, thus, extended to 0.19 µm; however, the lateral redistribution of p-dopants is both significant and irregular. In particular, three different contrast-level regions are identified, corresponding to different doping levels. Namely, a highly doped region similar to the profile of the passive sample [Fig. 2.4(a_1)], a lower-doped intermediate front that extends to 1 µm, and a last weakly-doped front exhibiting wavy patterns.

The randomness of the wavy front of the p-doping is also illustrated in Fig. 2.4(b), where a waveguide is depicted. Similarly, the doping profile can extend inside the LD and BH regions, leading to higher free-carrier absorption and QW intermixing. The doping-induced optical absorption is the primary determinant of the Q-factor of the laser cavity (see Sec. 6.3), and thus this random lateral redistribution of dopants may be critical for the laser performance. The non-uniform lateral distribution of Zn dopants in InP is attributed to the increased density of defect, e.g., threading dislocations in strained materials that accelerate the diffusion along the defect.

Since the p-doping profile could not be accurately controlled, two variants of the p-doping offset were included, with 1 µm and 1.5 µm p-offset from the center of the LD cavity. The devices featuring the latter doping design did not achieve lasing due to poor injection efficiency, which is related to the low mobility of the holes (for more information, the reader is referred to section **??**). Such a device is shown in the Si camera image depicted in Fig. 2.4(c), where the InP emission from the p-i interface is observed.

In addition, half of the 1 µm p-offset devices were observed to exhibit worse performance or no lasing. This effect is described in Appendix A.1, where the death and threshold statistics of the lasers are given. The non-lasing devices followed a pattern based on the parity of the DUV mask[6] attributed to the misalignment of the DUV mask during the p-doping definition. Although the DUV stepper tool used in this work can provide fine alignment (down to 50 nm), the actual alignment poorer due to the quality of the alignment marks and wafer size limitations. Hence, a misalignment up to 500 nm has been consistently observed in SEM. Details on the doping process are provided in [116], [129]. Overall, the InP emission pattern from the p-i interface ranges between the patterns of Figs. 2.4(c1-c2), where significant InP emission from the BH side corresponds to poorly performing devices.

[4]The device is fabricated on an InP wafer, and the BH definition step in the process flow is omitted.

[5]Systematic measurements showed that the lateral redistribution of Si dopants is 0.14 µm, while the lateral redistribution of Zn dopants is 0.35 µm compared to the DUV mask.[116]

[6]To increase the device density, each p- and n-contact is shared between 4 devices, except for those at the edge of each device group.

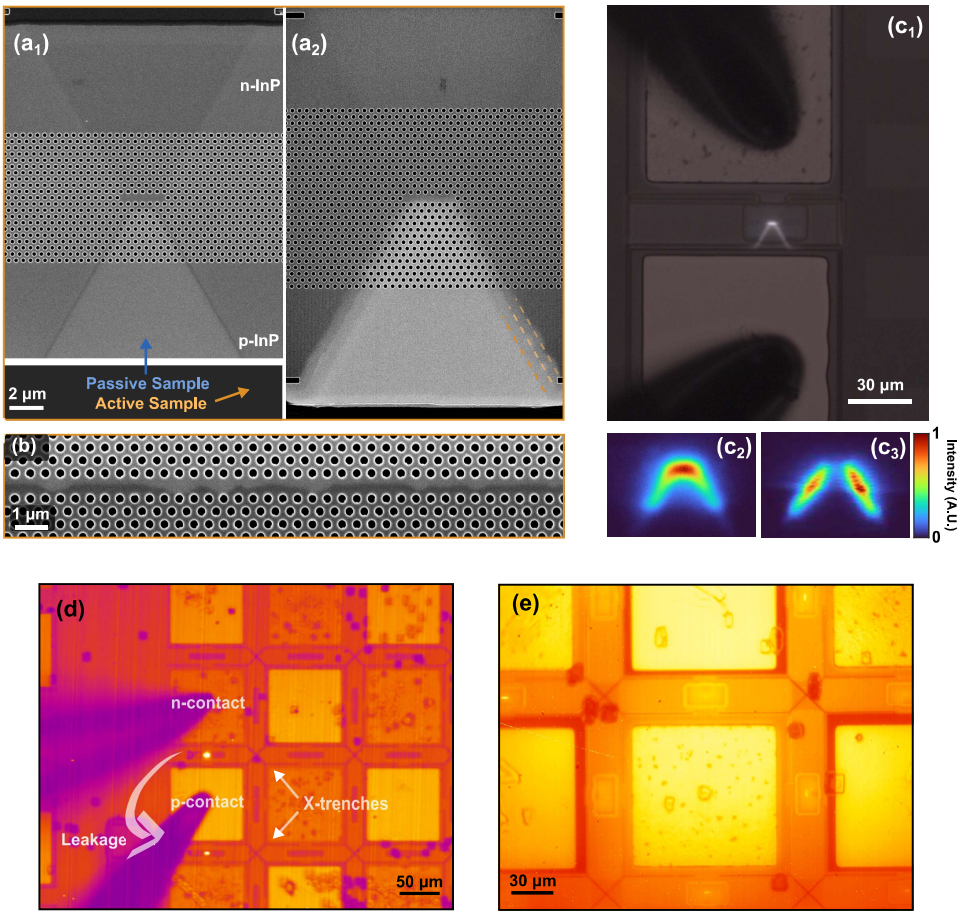

Figure 2.4 | Doping and regrowth. (a) SEM images of a passive (a_1) and an active (a_2) PhC cavity. (b) SEM image of a doped and active PhC waveguide. (c_1) Microscope image of the InP emission from the p-i interface. Heat maps of the InP emission for a large (c_2) and a short p-offset (c_3). (d) Leakage from the i-InP layer results in EL from a neighboring PhC laser. (e) PL emission from different L7 cavities sharing similar BH regions and doping regions.

Early on in the project, it was discovered that significant current leakage was spread over the wafer. In particular, electroluminescence (EL) was observed from all devices sharing the p-contact due to the low resistivity of the intrinsic InP region. The InP has a background n-doping concentration of 10^{15} cm^{-1}. As a result, X-shaped trenches were added to the contacts' isolation trenches for better electrical isolation. Fig. 2.4(d) shows the undesired EL of a neighboring device, where the leakage is passing through the i-InP layer - the edge of this device group has not

been electrically isolated. Leakage current, although suppressed, still occurs between devices that share the same contact. A prominent example is the reduction of the threshold of an L3 laser from 13.2 µA to 10.2 µA by collapsing the neighboring devices using the electrical probes. This experimental finding is inconsistent with an equivalent diagram model since the neighboring laser diodes are reversed-biased, adding to the recurring inability to replicate the observed electrical characteristics of these laterally doped lasers.

2.3.3 BH technology

The BH definition poses one crucial challenge since the etching and regrowth are generally associated with low quantum efficiency and poor yield due to the non-radiative recombination centers and mismatch of the different layers.

High-temperature processing is especially challenging in III-V/Si platforms due to the thermal expansion coefficients mismatch responsible for low material quality. In this process, the InP device layer is below the critical thickness, above which dislocations significantly degrade the material quality.[130] However, high-density post-regrowth defects are found on the wafer and most likely originate from contamination sites at the bonding interface. These defects are regions where no material is grown and can be observed in the microscope pictures of Figs. 2.4(d-e). Although the defect density varies between wafers, it is not considered a major contribution to faults of the intrinsic PhC cavity lasers, where faults are fatal defects.[131] However, longer device components, e.g., InP wire waveguides combined with grating couplers or complete optical links, have a miniscule probability of survival due to the high defect density. Finally, the optical characterization of lasers across the 2" wafer indicates a statistical correlation between good device performance and low-defect density.

Another critical parameter dictating the laser performance is the internal quantum efficiency (IQE). By conducting a series of qualitative photoluminescence (PL) measurements, we observed a random variation of the IQE between devices. In Fig. 2.4(e), a microscope image of a PL setup is shown. The sample is illuminated by a 980 nm LED lamp, and the image is captured by an InGaAs camera. The LED lamp excites the BH regions, and the PL emission can be observed by filtering out the pump via a long-pass filter. Although the illuminated structures feature similar optical cavities (L7s) and doping profiles, the PL intensity largely differs, suggesting a significant variance in the IQE of the different structures. It should also be noted that the bright devices exhibit the lowest laser threshold currents.

Characterizing the IQE variability of the BH regions poses a major experimental challenge. A systematic quantitative investigation has yet to be conducted. Preliminary time-resolved PL measurements conducted by Pawel Holeva et al. showed that the IQE could have an order of magnitude variations between devices. At the same time, a systematic dependence of the IQE on the alignment of the BH structures with respect to the Si substrate was observed. The latter trend is attributed to the linear thermal expansion coefficient mismatch along the different crystal plane orientations.

2.4 Summary

This chapter gives an overview of the basic design of the PhC lasers studied in this project. Furthermore, a brief description of the nanofabrication process was given. Finally, the main fabrication limitations were discussed, focusing on the effect on the PhC holes, the lateral doping, and the BH active region. In particular, it was found that the patterning of the PhC on InP using subsequent ICP etching produces good-quality holes. We also discuss the randomness during the Zn thermal diffusion, which was found to be an essential parameter dictating the performance of the laser. Furthermore, discussions about the systematic p-doping mask misalignment and the leakage current through the InP membrane were included. Finally, we identify a significant variance in the internal quantum efficiency of the individual BH regions via qualitative photoluminescence measurements.

CHAPTER 3

Laser Characterization

This chapter describes the various methods and techniques for characterizing the static and dynamic properties of PhC lasers and passive PhC optical resonators.

3.1 Setup for Laser Characterization

The optoelectronic properties of the PhC lasers were characterized via a micro-electroluminescent setup. The schematic diagram of the setup is shown in Fig. 3.1(a). A semiconductor test system is connected to micropositioning electrical probes to apply a DC voltage on the device under test (DUT). The light leaking vertically from the PhC laser is collected via a 50x long-working distance objective (NA = 0.42) and is coupled to a multi-mode fiber (MMF) via a fixed achromatic lens. The position of the fiber coupler (FC) is controlled via a micropositioning fiber alignment stage. The light is measured using an optical spectrum analyzer (OSA). The sample holder features a thermoelectric cooler (TEC) that can adjust the chip's temperature. The TEC is used only in dedicated experiments since the ambient temperature of the optical lab is maintained at 23 °C. The microscope is also equipped with two different cameras featuring an InGaAs and a Si detector for detecting light at IR and visible-NIR, respectively. 3.1(a) shows an InGaAs camera image using the 50x objective. The image features light emission from a PhC laser. The cameras are mostly used for navigating the chip, while the fiber alignment is done by maximizing the collected power at the OSA.

3.1.1 Data Acquisition and Curve Fitting

Fig. 3.1(b) depicts the collected output power and applied voltage versus the injected current (LIV curve) of a 3-QW L7 laser. The LI curve exhibits a characteristic kink indicating the laser threshold. Since there is no out-coupling scheme for laser light, the collected output power is the light leaking vertically from the cavity that would be considered optical losses in a realistic on-chip communication link. As a result, the collection efficiency of this setup is poor, which severely limits the detection of spontaneous emission occurring before the laser threshold.

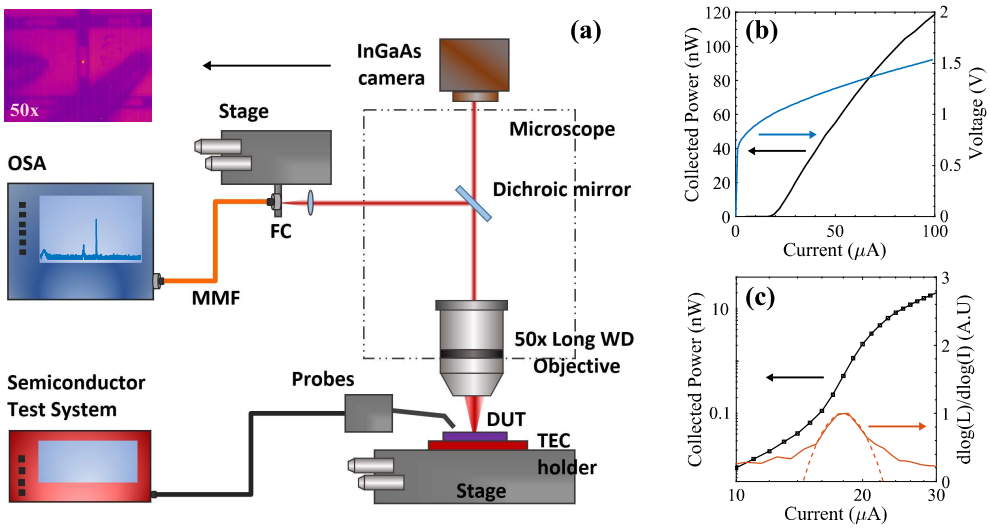

Figure 3.1 | Laser characterization setup and laser threshold. (a) Schematic diagram of the laser characterization setup. A semiconductor test system is used to apply a DC bias voltage to the DUT via electrical probes. The vertically leaking light is collected via a 50x objective and is coupled to an MMF. The collected light is measured using an OSA. (b) Collected output power and voltage versus input current for a typical 3-QW L7 laser. (c) Log-log plot of the input-output curve and its derivative.

Output Power: Since the accurate estimation of the spontaneous emission is important for characterizing the laser, the OSA scanning parameters should be optimized as follows: The OSA spectral scan should be focused around the laser peak, and its parameters should be chosen to maximize the sensitivity (long exposure time and high amplification) and minimize the spectral resolution (wide spectral integration). In such a measurement, the linewidth information of the laser peak is lost, and the peak will exhibit a flat top, which is used to extract the total peak power, and the center peak wavelength.

Laser wavelength and linewidth: An independent measurement should be done to retrieve the linewidth and resonant wavelength of the laser peak. Here, the resolution should be increased at the expense of sensitivity. The detected laser peak results from the convolution of a Lorentzian (device) and a Gaussian (OSA response) lineshape. A Gaussian lineshape is fit to extract the 3dB bandwidth and the center wavelength of the peak. The 3dB bandwidth of the laser peak saturates at the resolution limit of the OSA at the threshold. The total peak power can be extracted by spectral integration; however, such post-processing is inherently less accurate due to the indefinite resolution of the OSA.

Curve Fitting: All curve fittings described in this work were performed using a

nonlinear least-squares solver.[1] This automatic fitting method finds the fitting parameters $\{p_k\}$ of a numerical function $F(\{p_k\}, x)$ that satisfy the relation:

$$min \sum_i [F(\{p_k\}, x_i) - y_i(x_i)]^2$$

where (x_i, y_i) is the experimental dataset. Most fits require a good initial guess of the fitting parameters because fitting can stop at a local minimum. This general drawback can be suppressed using particle swarm optimization algorithms; however, this was not useful to the non-trivial fits of this work like the laser rate equations described in section 4.1.

3.1.2 Determining the Laser Threshold

The laser threshold is defined as the point where the gain equals the losses and is an important parameter that can be used to extract information for the laser.[132] The threshold signifies the transition from the spontaneous emission regime to the lasing regime, and it is typically associated with a kink in the output power.[2] The lasers that are characterized in this work exhibit moderate β-factors, and their threshold can be determined by the LI curve ($\beta \simeq 0.05 \ll 1$).

There are multiple ways to experimentally determine the threshold via the LI curve, all of which take advantage of the steep superlinear jump between the two linear regimes of spontaneous- and stimulated-dominated emission.[136] The most common method is to fit a linear line above the threshold, defining the threshold as the point where the line intercepts $y = 0$. This method assumes negligible spontaneous emission and is accurate for low-β lasers ($\beta < 10^{-2}$); however, it tends to underestimate the threshold of high-β lasers. An improved method relies on performing a two-segment line fit before and after the threshold, which is found at the intercept of these curves. However, fitting before the threshold requires multiple points at the spontaneous emission regime, which is not possible due to the low collection efficiency. In addition, there are inherent difficulties in implementing such an algorithm for automated characterization.

An accurate method for determining the threshold for high-β lasers is extracting the maximum point of the second derivative of the LI curve ($max\{d^2L/dI^2\}$). This threshold estimation method can be implemented via automated fitting algorithms for large-scale characterization.[137] However, it was found to be sensitive to noise, and in many cases, semi-manual fitting and data averaging was required. Another highly-accurate and automated method is the threshold estimation via the maximum

[1] `https://mathworks.com/help/optim/ug/lsqcurvefit.html`

[2] The most notable exception to this rule is the ultra-high β-factor lasers, also known as *thresholdless* lasers,[133]–[135] where the transition to lasing can be identified only by the change of the coherence properties and photon statistics of the emitted light. The most popular method for determining the threshold for such lasers is via the transition from thermal to coherent light observed in auto-correlation measurements.[132]

point of the first-order derivative of the log(L)-log(I) curve,[136] as seen in Fig. 3.1(c). This method was used throughout the project since it is highly robust against noise, and the global maximum of the derivative always coincide with the actual aser threshold. The precision of this method is determined by the injection current's scanning increments. A second-order Taylor expansion around the maximum of the derivative ($max\{dlog(L)/dlog(I)\}$) can be used to increase the precision of the threshold estimation.

All of the above methods require a spectral scan of the OSA around the laser peak. A much faster measurement can be achieved if the total laser power is measured by a photodiode. This method also tends to underestimate the threshold because of the significant spontaneous emission of the higher-order modes. Furthermore, integrating all the emitted light increases the perceived β-factor of the LI curve, since there is significant spontaneous emission from the higher order modes. Using a bandpass filter can alleviate these problems, although any manual tuning of the filter will counterbalance the gains in the measurement time. Finally, a fast threshold estimation can be done using the IV curve; due to the Fermi level pinning at the threshold, an abrupt change in the slope of dV/dI is observed. Thus, the threshold can be found at ($max\{d^2V/dI^2\}$).[138] This threshold estimation method is the industry standard for initial laser screenings avoiding high-cost light detection. Unfortunately, such a change in slope could not be observed routinely since it suffers from large noise due to the bad contact of the probes.

3.2 Laser Characterization Setup for Optical Pumping

During the project, both optically- and electrically-pumped lasers were characterized[3]. For this purpose, the Laser Setup of Fig. 3.1 was modified to incorporate an optical pumping scheme as shown in Fig. 3.2(a), and can be summarized as:

1. A high-power 1310 nm laser diode is used for pumping. Its power is adjusted via a variable optical attenuator (VOA). The solid yellow lines represent single-mode fibers (SMFs).
2. The pump light is split via a 20 dB coupler; The 1% of the pump power is real-time monitored via a power meter (PM), while the rest 99% is used for pumping.
3. The pump is sent to a wavelength division multiplexer (WDM) and then to a fiber polarization controller (FPC). The pump polarization should match the polarization of the QWs for efficient pumping.
4. The pump is coupled to free-space using an FC mounted on a 3-axis kinematic mount. The light is collimated via a lens, and its beam size can be adjusted via a two-lens beam expander (BE). A 50x objective (NA = 0.42) focuses the pump on the DUT.

[3]The electrically-pumped lasers can also be pumped from the top using a pump laser.

5. The objective collects the reflected pump and emitted signal. The pump and signal beams are depicted in blue and red, respectively.
6. The WDM is used to filter the reflected pump from the signal. The spectrum of the DUT is measured via the OSA.

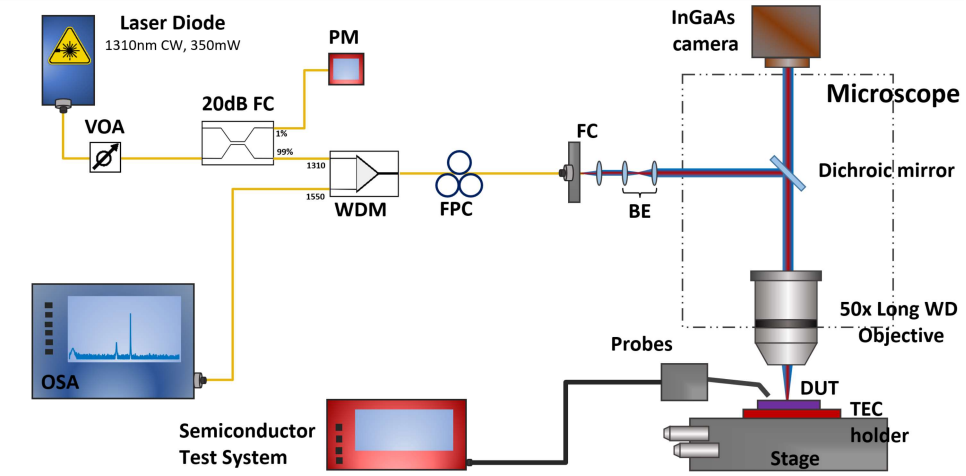

Figure 3.2 | Modified laser characterization setup. (a) Schematic diagram of the modified laser setup for optical pumping; a 1310 nm diode laser is used to pump the DUT. The pump power is controlled via a variable optical attenuator. The same objective is used to focus the pump on the device and to collect the signal. The blue and red light beams represent the pump and the signal, respectively. The pump and signal light are separated using a wavelength division multiplexer.

The alignment of the pump is done by maximizing the collected signal. Since the same objective is used for pumping and collecting, neither the pumping nor the collection efficiency is optimal, rather, the product of the two. The pump laser is focused on the DUT with a spot diameter of $D = 1.22 \cdot \lambda_{pump}/NA = 3.8$ µm. The overlap of the pump's spotsize with the active region is denoted as η_{area}, and should be calculated for each laser ($\eta_{area} \approx A_{active}/D$). A large part of the incident pump light is reflected due to Fresnel reflection (R $\sim$ 30%),[139] while each QW absorbs around 1% of the pump for a single pass.[138] Thus, the effective pump power is calculated as:

$$P_{eff} = \eta_{area}(1 - R)\gamma_{well}P_{in} \tag{3.1}$$

where P_{in} is the incident power on the sample, and γ_{well} is the relative absorption for each QW layer for a single pass of the pump light. In this framework, multiple reflections at the membrane-air interfaces are not included.

At the beginning of the project, the micropositioning fiber alignment stage of Fig. 3.1 was used, exchanging the MMF and FC for an SMF and an angled-polished

connector FC. However, it was found that a small angle of the fiber alignment stage can lead to up to 10 dB of signal loss compared to the MMF collection fiber. The system of lenses described in this section can reduce that difference down to 2 dB and should be used in the future.

3.3 Small-Signal Modulation

This section describes the experimental setup for characterizing the small-signal response of electrically-driven PhC lasers shown in Fig. 3.3.

The applied AC voltage for the small-signal modulation is generated by the vector network analyzer (VNA), while the DC bias voltage defines the operating point of the laser and it is generated by a bias-tee using a high-precision semiconductor test system. The voltage is applied to the DUT using RF probes. All electrical components are coupled via 50 Ω RF cables. The light emitted from the DUT is collected with the same SMF-based optics described in section 3.2. The light is amplified via an EDFA; whose amplified spontaneous emission is filtered out via a band-pass filter (BPF). The light is then split using a 20 dB coupler; 1% of the light is measured using an OSA for real-time signal inspection, while the 99% is coupled to a 70 GHz photodiode (PD). The diode is connected to the VNA's second port to characterize the laser's response.

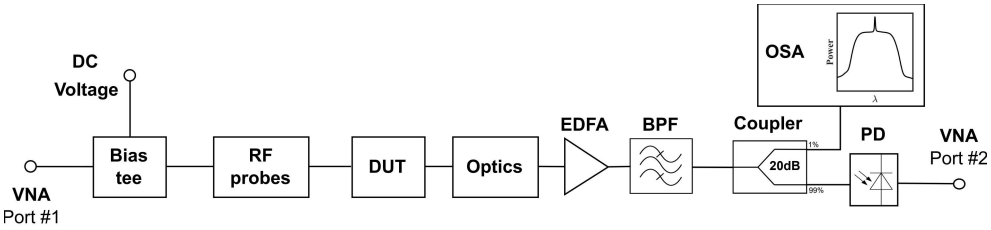

Figure 3.3 | RF Setup for small-signal modulation measurements. The Vector Network Analyzer (VNA) transmits an RF signal that is combined with a DC signal using a bias tee. RF probes are used to drive the DUT. Light emitted from the DUT is collected via a 50x objective and is coupled to an SMF using free-space optical elements. The signal is amplified via an EDFA and filtered using a band-pass filter. Part of the light is coupled to an OSA for real-time spectrum inspection. The majority of the light is sent to a PD connected to Port #2 of the VNA.

The VNA can fully characterize a multi-port network's Scattering (S-) matrix. The elements of the scattering matrix are known as the S-parameters. For a two-port network, the S-matrix is described by:

$$S = \begin{pmatrix} S_{11} & S_{12} \\ S_{21} & S_{22} \end{pmatrix}$$

where S_{11} and S_{22} describe the reflection coefficients for port #1 and port #2, respectively, while the S_{21} and S_{12} are the transmission coefficients. Ports #1 and #2

of the VNA would be the input and output ports, respectively. In this work, we are interested in the S_{21} parameter that describes the frequency response of the DUT; S_{21} can also be thought of as the response of the E-O conversion, where the electrical signal is converted to optical via the DUT. The S_{21} measurement requires a final O-E conversion via the PD; however, the frequency response of the PD is flat at low frequencies ($f < 50$ GHz), and thus it is neglected.

Limitations: This is a delicate measurement where each element can severely affect the quality of the signal. First of all, the quality and the handling of the RF cables are important to minimize reflections. The impedance of the 50 GHz RF probe used in the experiments differs from the standard 50 Ω due to a broken Ground-connection. Most importantly, there is a large impedance mismatch due to the high resistance of the DUT (∼MΩ). Nevertheless, the measurement is very sensitive and robust against noise since the VNA performs a homodyne measurement. As a rule of thumb, output powers above -60 dBm before amplification are required.

The two-port calibration is required to get a physically-meaningful signal with the VNA, and it is done via a Short-Open-Load-Through (SOLT) calibration algorithm.[4] A calibration kit was used to measure the SOL of each port, while the T measurement was done by connecting the ports directly. During calibration, extra adapters were used, reducing the quality of the calibration. More importantly, Port #1 was calibrated after the bias-tee, while Port #2 was calibrated directly. Ideally, the whole system - excluding just the DUT - should have been included in the calibration. Additional technical information is included in Appendix D.

3.4 Characterization of Passive PhC Cavities

At the beginning of the project, it became clear that the etching quality of the PhC holes was not optimal; thus, the FDTD estimations of the Q-factor might not be accurate. As a result, an experimental method to extract the Q-factor of the laser cavities was needed, and a dedicated setup based on cross-polarization resonant scattering spectroscopy was established and optimized by the author. Today, this setup is the main tool for characterizing passive PhC cavities and investigating new cavity designs preceding the fabrication of a complete laser. In this section, the working principle and the realization of the experimental setup are described. Finally, the current limitations and alternative setups are discussed.

3.4.1 Cross-polarization Resonant Scattering Spectroscopy

Measuring the Q-factor of a PhC cavity using cross-polarization resonant scattering spectroscopy was first demonstrated by McCutcheon et al.[140] and has been used extensively ever since.[69],[141]–[143] In this method, the polarization reference frame

[4] https://www.microwaves101.com/encyclopedias/network-analyzer-measurements

of the pump light and the cavity mode is rotated by 45°to couple part of the pump light to the cavity mode while measuring light in the orthogonal polarization in order to filter out the reflected pump from the signal. In this scheme, the cavity is rotated, so the product of the coupling efficiency (pump→mode) and the collection efficiency (mode→cross-polarization of the pump) is maximized, while the reflected pump is filtered out by several orders of magnitude. This method enables the direct measurement of the intrinsic (unloaded) Q-factor; however, the contrast of the mode with the background can be low, especially for high Q-factor cavities.

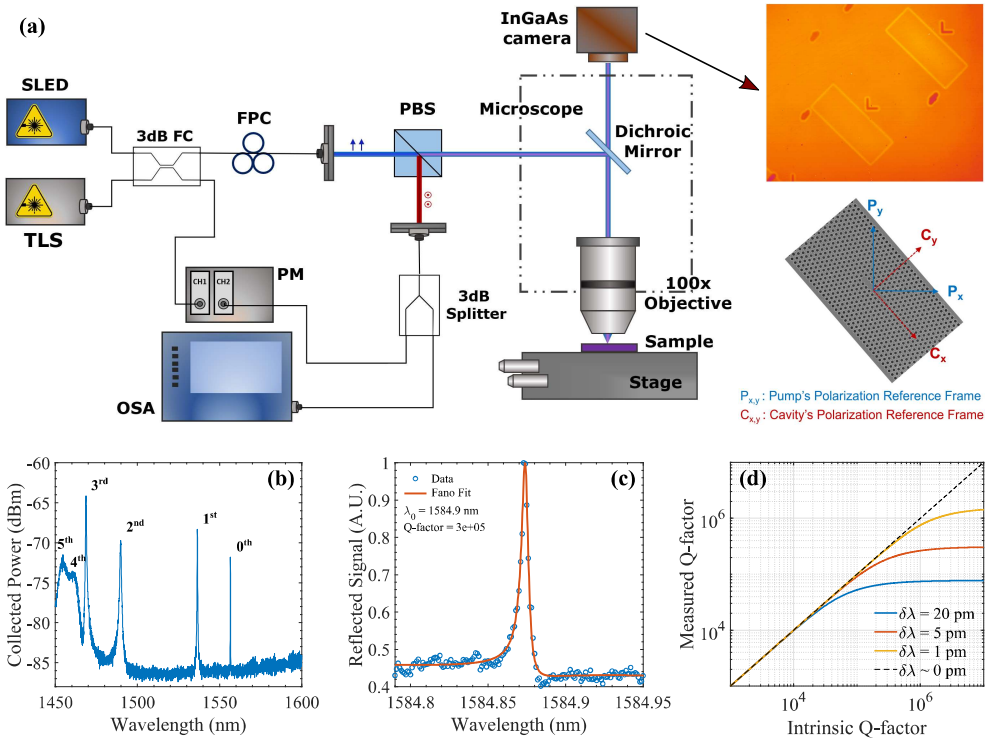

Figure 3.4 | Q-factor measurements. (a) Schematic diagram of the cross-polarization Q-factor characterization setup. The blue and red light beams represent the pump and signal, respectively. (b) Reflected signal of an L7 cavity exhibiting the characteristic mode structure up to five higher order modes. (c) Reflected signal of an H0 cavity emitting in the L-band exhibiting a Q-factor of 300,000. (d) Convoluted (measured) Q-factors versus the intrinsic Q-factors of a resonant mode located at 1550 nm.

Fig. 3.4a shows the experimental setup for Q-factor measurements. The black lines connecting the various instruments and components represent SMFs, while the blue and red beam represents the orthogonally-polarized pump and signal. Pump light from a tunable laser source (TLS) is sent to a Fiber Polarization Controller (FPC) and is coupled to free space; part of the pump light is sent to the power

meter for a reference measurement using a 3dB fiber coupler (FC). The pump light is filtered via a Polarization Beam Splitter (PBS) and is focused on the PhC cavity using a 100x objective lens ($NA = 0.85$). The cavity is rotated by 45°to maximize the peak contrast, and its position is controlled by a micro-positioning stage. The reflected pump and the light leaked from the cavity (signal) are collected and filtered via PBS and another LP. The signal is then measured via the power meter (PM). The PM is triggered by the laser via a BNC cable. For alignment and for measuring low Q-factor cavities, a broadband Superluminescent Diode (SLED) combined with an Optical Spectrum Analyzer (OSA) are used for pumping and detecting, respectively, and are incorporated into the setup via the 3dB FC and the 3dB splitter.

In the scattering spectrum of Fig. 3.4(b), the mode structure of an L7 cavity can be clearly observed. The mode structure is the fingertip of each cavity, and each mode can be studied individually. In the high-Q regime, a preliminary optimization on the lower-Q modes might be required before the high-Q modes are observable.

The scattering spectrum of the fundamental mode of an optimized H0 PhC cavity is shown in Fig. 3.4(c). Since the reflected pump cannot be filtered out completely, the detected signal will exhibit an asymmetric Fano lineshape resulting from the interference of the discrete (Lorentzian) cavity mode with the broadband background reflection of the pump signal.[141] Depending on the phase difference between the two signals, the Fano lineshape can vary from a red- or blue-parity asymmetric lineshape to a symmetric pure or reverse Lorentzian.[144] In order to extract the Q-factor, the scattering spectrum is fitted with a Fano lineshape given by:[69]

$$F(\lambda) = A \cdot \frac{q + \left(\frac{2\,(\lambda - \lambda_0)}{\Delta\lambda}\right)^2}{1 + \left(\frac{2\,(\lambda - \lambda_0)}{\Delta\lambda}\right)^2} + B \tag{3.2}$$

where q is the dimensionless asymmetry parameter, λ_0 is the resonant wavelength, and $\Delta\lambda$ is the linewidth of the mode defined as the Full-Width at Half-Maximum (FWHM). The A and B are the scaling and background constants. The Q-factor is then calculated as $Q = \lambda_0/\Delta\lambda$. The extracted Q-factor for this H0 cavity has been calculated as 270,000 with an estimate uncertainty of ±20,000.[5,6] Adjusting the focus of the objective changes the relative phase between the discrete and the continuous mode, which manifests as the change in the parity of the Fano Lineshape, as shown in Fig. 3.4(c).

The detected signal is a convolution of the response of the instrument performing the wavelength scan and the intrinsic Fano lineshape of the mode.[145] Since higher resolution comes at the expense of a long measurement time, identifying different

[5]The uncertainty is estimated by independently fitting 10 subsequent measurements. Although the scanning parameters are identical, and the goodness of fit is equally good, there is a large variance of the calculated Q-factor.

[6]This sample has been fabricated during the latest part of the PhD project showing the improved quality of the InP etching compared to the sample presented in Sec. 5.3.

Q-factor regimes is important. The OSA and the TLS have a gaussian response function, for the wavelength step is given by the wavelength tuning mechanism of the instruments. Although the minimum step of the OSA is 20 pm, the actual resolution of the instrument is neither well-defined, nor constant throughout the range. In contrast, the resolution of the TLS is better defined and should be constant at the whole range, with a minimum resolution of 5 pm and 1 pm for continuous and step sweep operations, respectively.

The measured (convoluted) Q-factor versus the intrinsic Q-factor of a cavity mode using different resolutions is given in Fig. 3.4(d), where we assume a center wavelength of 1.55 µm, and a Lorentzian lineshape ($q = 0$). The convoluted profile has a Voigt lineshape,[146] with an FWHM of $\Delta\lambda_V = 0.535\Delta\lambda_L + \sqrt{0.217\Delta\lambda_L^2 + \Delta\lambda_G^2}$, where $\Delta\lambda_{V,L,G}$ is the FWHM of the Voigt, Lorentzian and Gaussian profile respectively.[147],[148] The intrinsic Q-factor (linewidth) ranges for a precise measurement using different instrument/operation modes are summarized in table 3.1. The acceptable error range is chosen arbitrarily as a 5% underestimation of the intrinsic Q-factor for resonance at 1.55 µm. As a rule of thumb, the intrinsic linewidth should be at least four times broader than the instrument's resolution.

Table 3.1 | Intrinsic linewidth and Q-factor regimes for different operation modes. The acceptable error range is defined as 5% of the Q-factor ($\lambda_0 = 1.55\mu m$).

Instrument	Resolution Limit (pm)	Linewidth Range (pm)	Q-factor Range (10^3)
SLED/OSA	20	$\infty - 86$	$0 - 18$
TLS sweep	5	$86 - 22$	$18 - 70$
TLS step	1	$22 - 4.4$	$70 - 350$

Limitations of the Setup

The main limitation of the cross-polarization setup is the low contrast of the signal compared to the high background of the reflected pump. The extinction ratio of the background is determined by the polarization scrambling of the scattered background light. This effect is more prominent for high Q-factor resonators since the light coupled in and out of the cavity is weak and comparable to the background. The combination of a low total Q-factor cavity with a high vertical Q-factor is also challenging to identify because it exhibits a broad low-contrast peak.

Choosing a high-NA objective also increases the contrast since more light is coupled to the mode, while the smaller spot size acts as a spatial filter. Thus, one of the first improvements of the setup is to switch from a 50x long-working distance objective (NA = 0.42) to a 100x short-working distance objective (NA = 0.85). The high magnification comes at the cost of 3 dB due to higher absorption in the objective, although this is not critical for this setup. The contrast is also affected by the pump

source. The TLS source achieves higher contrast than the SLED because the laser light is polarized and can be filtered out more effectively. However, the high power of the TLS combined with a low scanning speed can trigger nonlinear effects that distort the Fano lineshape. In such cases, the TLS pump should be attenuated until a good Fano fit is achieved.

Finally, we recently noticed inconsistent contrasts for similar cavity designs fabricated on different chips. The main difference between these samples was a different residual thickness of the SiO_2 layer after membranization. The most prominent hypothesis is that the background levels of the reflected pump can be suppressed by destructive interference between the reflections of the different layers along the epitaxial structure; however, simulations have yet to be performed. If this hypothesis is proven correct, the thickness of the air and SiO_2 between the InP membrane and the Si layer can be optimized for higher sensitivity.

This measurement configuration has been proven to be able to detect ultra-high Q-factors on Si cavities, and thus similar sensitivity should be possible on InP samples. However, for higher than Q-factors higher than 350,000, a high-resolution laser is needed combined with a long free-space Fabry-Perot reference cavity.[143],[149]

3.4.2 Alternative Setups

A promising way to achieve high contrast is to use in-plane ports to measure the loaded-Q of the cavity in the unloaded-Q limit ($Q_{loaded} \simeq Q_{int}$). In this configuration, light is pumped in the cavity via an in-plane waveguide, while the leaky cavity light is collected vertically via the objective allowing the spatial decoupling of the pump and signal. Such configuration has been realized by Noda's group,[150] and NTT[42],[75],[151] resolving ultra-high Q-factors ($\sim 10^6$). This is a promising approach that can be achieved using the PhC grating couplers (GC) developed at DTU,[118],[152] or the C-shaped free-space GCs.[153] During this PhD project, a pilot investigation was performed to test the performance of similar configurations.

Transmission measurements via PhC Grating Couplers

Firstly, a transmission experiment has been performed, where a new design was fabricated to evanescently couple light in and out of an L7 cavity using waveguides and PhC grating couplers as shown in Fig. 3.5(a). The grating couplers and the tapered wire waveguide were designed by Quentin Saudan,[119] who also assisted with the optical experiment.

Initially, a back-to-back transmission measurement was performed to characterize the GCs, as shown in Fig. 3.5(b). The GCs exhibit a low coupling efficiency of -20dB per GC with an FWHM of 35 nm, which limited the SNR. Fig. 3.5(c) shows the transmission spectrum of an L7 cavity. In this measurement, the fundamental and first-order mode could be identified. The bandgap of this PhC structure can also be observed in the spectrum spanning from 1470 to 1600 nm and is identified by the

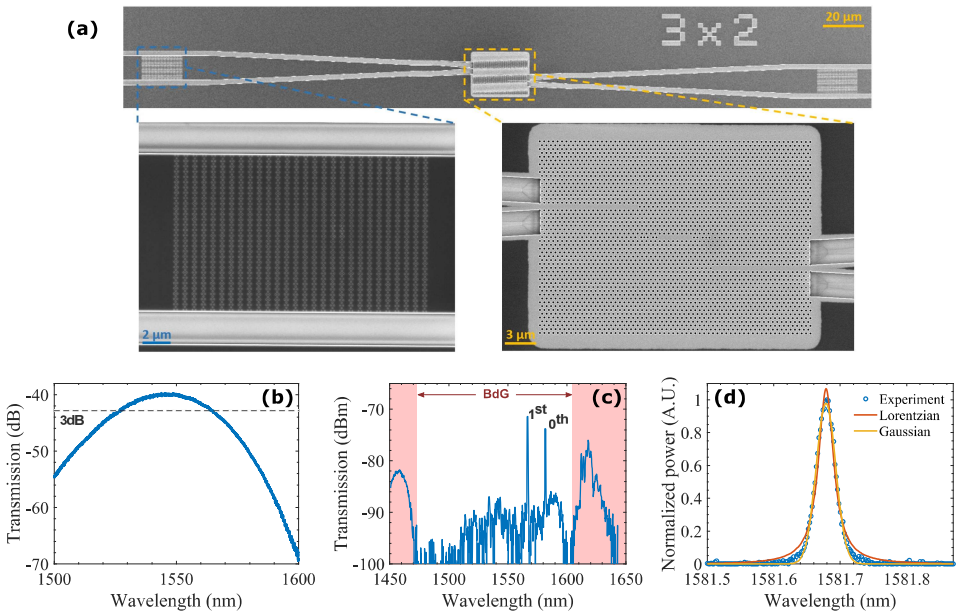

Figure 3.5 | Alternative Q-factor measurement: Transmission. (a) SEM images from an L7 cavity coupled to wire waveguides. (b) Back-to-back transmission of a waveguide coupled to two GCs exhibiting 20 dB loss per GC and an FWHM of 35 nm. (c) Transmission spectrum of an L7 cavity. The PhC transparency region is highlighted in red. (d) TLS scan around the fundamental mode, with superimposed Lorentzian and Gaussian fits.

transparent spectral regions[7] indicated with a red box. In Fig. 3.5(d), a TLS scan around the fundamental mode is shown. The lineshape lies between a Lorentzian and Gaussian distribution, also shown in the plot. This effect is attributed to non-linearities induced by the high injected power, which might also occur at resonant scattering measurements during a TLS step scan; however, here is more critical since high input power is required to compensate for the weak out-coupling efficiency.

Overall, the transmission experiment has an acceptable contrast but a low SNR and a narrow spectral range that depends on the GC performance. The reproducibility of the GCs is an issue because the fabrication process still needs to be optimal, and different GC variations should be included increasing the total number of devices on the chip. Furthermore, each device requires a large area due to the tapering of the wire waveguide. Finally, the alignment of the two fibers is time-consuming relative to alternative methods.

[7] Light in this spectral region can be transmitted between the wire waveguides without the mediation of the nanocavity since there is no PhC bandgap effect.

Pumping via C-shaped Grating Couplers,

More promising results were obtained by a free-space variant of the Q-factor setup, where the pump and collection beam spot positions are decoupled. In this configuration, the pump is coupled to the cavity via a cross-port (X-port) at the weak coupling limit ($Q_{loaded} \simeq Q_{int}$). The pump light is coupled to the chip via a C-shaped GC from the free-space. The signal is collected from the top of the PhC cavity.

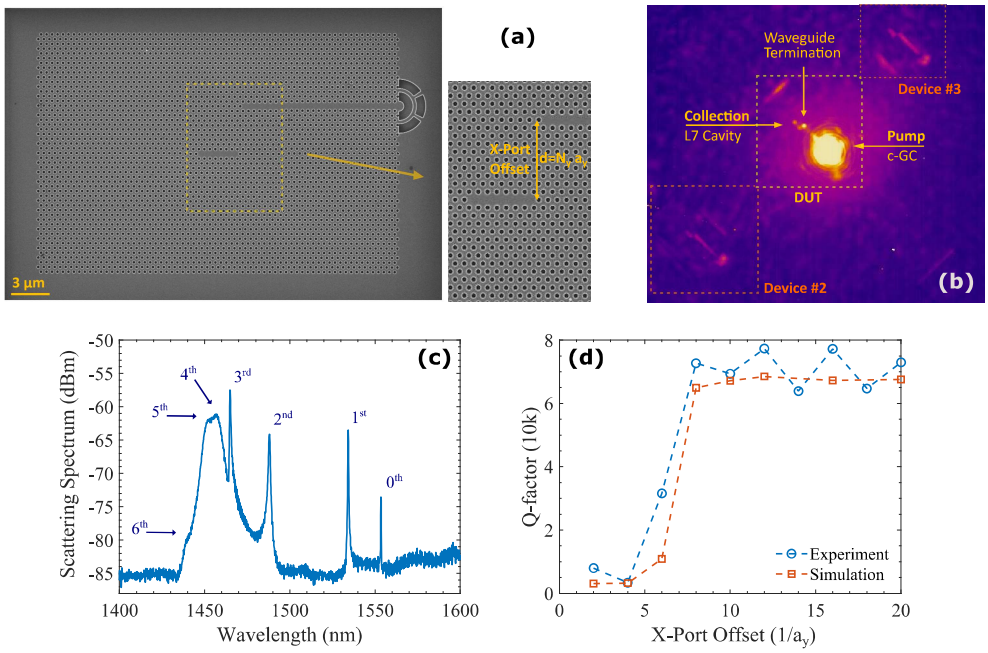

Figure 3.6 | Alternative Q-factor measurement: spatial decoupling of pumping and collection. (a) SEM image from an L7 cavity featuring an X-port and a C-shaped GC for free-space coupling. (b) Microscope image using an IR camera. The scattering patterns indicate the different parts of the device. (c) Scattering spectrum when collected from the top of the cavity ($N_y = 8$). (d) Experimental data and FDTD simulations of the Q-factor versus the X-port offset.

The fabricated device can be seen in Fig. 3.6(a). The W1 is placed along the $K - \Gamma$ direction in the N_y PhC row from the cavity defined as the X-Port Offset. A microscope image is shown in 3.6(b) exhibiting characteristic patterns due to the scattering of the pump light, eg. the GC where the pump is focused, the broadband scattering at the termination of the waveguide, and the light scattered from the L7 cavity. In this measurement, the pump and collection beam spot positions were adjusted independently, and a 50x objective (NA = 0.65) was used for a larger range of movement. During this experiment, cross-polarization filtering was maintained for both arms, limiting collected signal intensity. The scattering spectrum of the L7

cavity is shown in Fig. 3.6(c), where the L7 mode structure can be identified. The contrast of this measurement is the highest among all the investigated methods. Fig. 3.6(d) shows the Q-factor of the fundamental mode as a function of the X-port offset. The experimental data showed very good agreement with the FDTD simulations.

Overall, this method showed great promise and might deem necessary for low-contrast devices such as ultra-high Q designs and low-Q_{tot}-high-Q_v cavities, e.g., doped PhC cavities,[46] and EDC cavities.[128],[154] Future optimizations of the setup should include the removal of the cross-polarization filtering and the exchange of the SMF to a high-NA MMF for the collection arm. Furthermore, the design should be adjusted to a non-terminating W1 for a minimal vertical scattering of the pump light.

Photon Lifetime Measurement

Finally, the ultimate method to accurately measure ultra-high Q-factors exceeding a few million is a photon lifetime measurement,[75],[155] where a time-resolved measurement is used to extract the decay constant of the highest-Q mode. This method relaxes the requirement of the high-resolution TLS and the external reference cavity; however, extracting information for the lower-Q modes by multi-exponential decay fitting should be complicated, if not impossible. As a result, this method has important limitations, but it is valuable for designs with ultra-high Q-factors. Photon lifetime measurements have not been explored during this project.

3.5 Summary

This chapter describes all the different optical characterization methods used during the project and some elements of the data analysis. Specifically, the micro electroluminescent and photoluminescent setups used for the laser characterization are explained in detail, as well as a practical overview of the different methods for determining the laser threshold. Additionally, the radio-frequency measurement setup for the dynamic characterization of the lasers was introduced. Finally, the experimental setup for cross-polarization resonant scattering spectroscopy used for measuring the quality factor of the photonic crystal cavity modes is analyzed, and its current limitations are discussed. Finally, alternative setups for quality-factor characterization were described through pilot investigations.

CHAPTER 4

Laser Modelling and FDTD Simulations

Throughout the project, numerical models and simulations have been used to design the lasers and analyze the experimental results. The laser rate equations used to fit the experimental data is initially described. Secondly, the small-signal analysis used for modeling the laser dynamics is explained. Finally, an overview of the electromagnetic field simulations via the finite-difference time-domain (FDTD) is given. The validity, caveats, and limitations are analyzed for all the above methods.

4.1 The Laser Rate Equations

The laser rate equations is a powerful model of the laser behavior and can be used to extract important laser parameters from the experimental Input-Output curves via standard curve fitting techniques. The laser rate equations is a system of ordinary differential equations that relates the carrier density[1] with the photon density of the optical mode(s). The carriers and photons can be considered interacting reservoirs with different generation and loss mechanisms.

The laser rate equations used in this work are commonly employed to characterize semiconductor lasers and are described by the following relations:[156]

$$\frac{dN}{dt} = \frac{\eta_i I}{qV} - \left[\frac{1}{\tau_r} + \frac{1}{\tau_{nr}}\right] N - u_g g(N) N_p \tag{4.1a}$$

$$\frac{dN_p}{dt} = \left[\Gamma u_g g(N) - \frac{1}{\tau_p}\right] N_p + \Gamma\beta\frac{N}{\tau_r} \tag{4.1b}$$

where N and N_p is the carrier density and photon density of the lasing mode inside the optical cavity.[2] The first term on the right-hand side of eq. 4.1a is a generic term that represents the carrier pumping rate comprised of the electrical injection

[1] In diode lasers, the carriers are electron-hole pairs whose recombination can generate a photon.
[2] Only valid for single-mode lasers. For multi-mode lasing, the model is extended.

efficiency η_i, the applied current I, the elementary charge q, and the volume of the active material V. The second term is a carrier depletion term, where the carriers N are decaying with the characteristic time scales τ_r and τ_{nr}, and τ_p expressing the radiative and non-radiative recombination lifetimes, respectively. The third term represents the stimulated recombination rate that also depletes the carriers. The st. recombination rate depends on the photon density of the optical mode, its group velocity u_g, and the gain $g(N)$. The first term on the right-hand side of eq. 4.1b is a photon generation/loss term proportional to the photon density. The photons are generated via stimulated emission with a rate of $\Gamma u_g g(N)$, where Γ is the confinement factor, and decay with the characteristic photon lifetime τ_p. The last term of eq. 4.1b represents the generation of photons via spontaneous emission, coupled to the lasing mode, and is dependent on the confinement factor, the β-factor and τ_r and the number of carriers. The β-factor is the spontaneous emission factor defined as the fraction of spontaneous emission coupled into the laser mode.

Injection Efficiency and Recombination Rates: The injection efficiency η_i is defined as the fraction of the current that reaches the QW layer, compared to the total applied current as:

$$\eta_i = \frac{I_{act}}{I_{act} + I_{leak}} \tag{4.2}$$

where I_{act} and I_{leak} are the currents that reach the QW layers and the leakage current that recombines outside the QWs, respectively. I_{act} can be further split into I_{ph} and I_{nr}, which are the fractions of the current that lead to radiative and non-radiative recombination inside the active region, respectively. The carrier injection efficiency differs from the internal quantum efficiency that is defined as $IQE = I_{ph}/(I_{ph}+I_{nr}) = \tau_r^{-1}/(\tau_r^{-1} + \tau_{nr}^{-1})$ and is dependent on the gain material quality.

The recombination rates of the second term in eq. 4.1a is an approximation of the more physically accurate terms:[156]

$$AN + BN^2 + CN^3 \simeq \left[\frac{1}{\tau_r} + \frac{1}{\tau_{nr}}\right] N \tag{4.3}$$

where AN is the linear nonradiative recombination term, BN^2 is the radiative recombination term, and CN^3 is the Auger recombination term. The linear non-radiative term stems from trap-assisted electron or hole recombinations due to crystal defects, dopant atoms, and interface dangling bonds that create midgap states. The radiative recombination term depends on the bimolecular coefficient B and represents the optical band-to-band transitions. Finally, the Auger recombination is a three-carrier process where the two electrons collide; one electron is knocked down in the valence band, while the other is sent higher in the conduction band. The later electron thermalizes back to the bottom of the conduction band, releasing the energy as heat. Analogous processes can happen with holes. Auger recombination is increasing rapidly at high current densities. It is prominent in long-wavelength QW lasers, limiting their internal quantum efficiency.

The Gain Model: The probability of a photon of specific energy to interact with the gain medium. Depending on the pumping level, the gain material can absorb or amplify photons within a particular frequency range. Details on the gain spectrum and gain model can be found in Chapter 4 of [156]. In short, the gain depends on the reduced density of states (DOS), defined as the density of electron-hole transitions per unit transition energy and per unit gain region volume. The occupation probability of the electron and holes follow Fermi-Dirac distributions. The maximum gain (or loss) energy spectrum depends on the shape of the DOS. For bulk materials, the DOS exhibits a square root dependence on energy. In contrast, the DOS changes for media with reduced dimensionality, e.g., quantum wells and quantum dots exhibit a step-like and a δ-Dirac distribution shape, respectively. Thus, for QWs, the maximum gain resembles a step-like function that is smoothened by lineshape broadening.

The gain model expresses the gain at the peak of the gain spectrum as a function of the carrier density, which is also used in the laser rate equations. The gain of QWs is successfully modeled using a two-parameter logarithmic function:[156]

$$g(N) = g_0 \cdot \ln\left(\frac{N}{N_{tr}}\right) \tag{4.4}$$

where N_{tr} is the transparency carrier density of the gain material, and g_0 is the gain coefficient. At the transparency carrier density, the stimulated emission rate cancels the optical absorption rate, and thus the intensity of the light remains constant during propagation through the active region.

For bulk materials, the gain curve is better modeled using a linear gain model, $g = g_0(N - N_{tr})$, that also supports analytical solutions to the laser rate equations. The linear gain model is a good approximation for the logarithmic gain model for carrier densities close to transparency. However, the reduced computation time was not deemed sufficiently important to make such an approximation for the strained QWs used in the project. Thus, the logarithmic gain was used.

The confinement factor and group velocity: The confinement factor (Γ-factor) can be understood as a weighting function to define the modal gain or loss accounting for the spatial variation of the energy density ($U \propto \varepsilon(\mathbf{r})|E(\mathbf{r})|^2$) of the optical mode. For a laser, the confinement factor is typically defined as the fraction of the optical energy residing in the gain material over the total energy of the mode. It can be expressed as:[156]

$$\Gamma = \frac{\displaystyle\int_{V_{act}} \varepsilon(\mathbf{r})|E(\mathbf{r})|^2 \mathrm{d}^3\mathbf{r}}{\displaystyle\int \varepsilon(\mathbf{r})|E(\mathbf{r})|^2 \mathrm{d}^3\mathbf{r}} \tag{4.5}$$

where $\varepsilon_i(\mathbf{r})$ and $E(\mathbf{r})$ is the permittivity and the electric field, respectively. For conventional semiconductor lasers, the permittivity terms of eq. 4.5 are typically neglected because of the small difference between the permittivity of the active material

and the effective permittivity of the mode. In PhC lasers, though, such approximation heavily underestimates the confinement factor because of the much lower permittivity of the holes. The confinement factor is used to calculate the modal gain $\Gamma g(N)$.

In addition, the definition of gain/loss assumes a propagating optical field that is amplified/attenuated. For diode lasers, a Fabry-Pérot cavity picture is adopted, where light propagates back and forth in an optical waveguide between two broadband mirrors.

For line-defect 2D-PhC waveguides, the group velocity u_g can vastly differ from the phase velocity due to slow Bloch modes. Thus, the group velocity is extracted from the dispersion relation of the W1 waveguide. Longer LD lasers operate closer to the band edge, slowing down the light and enhancing the light-matter interaction.[157] The Fabry-Pérot model works well down to the shortest PhC cavities,;[158] however, it is vital to calculate the group velocity accurately.

The photon lifetime and quality-factor: The photon lifetime is the characteristic time scale on which the field contained in the cavity decays. The optical field can decay through various loss channels like scattering and absorption during propagation. The photon lifetime can be written as $\tau_p = 1/u_g\alpha_{tot}$, where α_{tot} is the total loss coefficient. The photon lifetime can also be associated with the total Q-factor of the optical cavity as $Q_{tot} = \omega\tau_p$, where ω is the oscillation frequency of the mode. Combining the two leads to the more useful expression:

$$Q_{tot} = \frac{2\pi n_g}{\alpha_{tot}\lambda} \tag{4.6}$$

where λ is the corresponding resonant wavelength in free-space, and n_g is the group refractive index. The total Q-factor is dependent on all the channels that the field can decay to; Taking into account only the most important loss mechanisms, the Q-factor can be written as:

$$\frac{1}{Q_{tot}} = \frac{1}{Q_{int}} + \frac{1}{Q_{dis}} + \frac{1}{Q_{abs}} + \frac{1}{Q_{wg}} \tag{4.7}$$

where Q_{int} is the intrinsic/ideal Q-factor of the designed cavity, Q_{dis} is a limiting factor related to the scattering losses due to disorder, Q_{abs} is related to material absorption, and Q_{wg} is related to a corresponding decay rate if an outcoupling waveguide is added to the design.

The β-factor: The β-factor or spontaneous emission factor is conventionally defined as the fraction of the total spontaneous emission coupled into the lasing mode. Experimentally, the effective β-factor is manifested as the magnitude of the superlinear jump before- and after-threshold and depends not only on the radiative emission to the background optical modes but also on the non-radiative recombinations.[159] In the laser rate equation fitting, we neglect any dependence of the β-factor on the carrier density or the Purcell enhancement.[160],[161]

4.1.1 Laser Threshold Condition

The laser threshold is defined as the condition where the modal gain equals the losses of the optical cavity, $\Gamma g_{th} = a_{tot}$. Using the logarithmic gain model, the threshold current of a laser can be written as:[156]

$$I_{th} = \frac{qV}{\eta_i} B N_{tr}^2 \cdot \exp\left(\frac{\alpha_{tot}}{\Gamma g_0}\right) \tag{4.8}$$

where B is the bimolecular recombination coefficient and N_{tr} is the transparency carrier density. The main assumption of this formula is that the β-factor and the non-radiative recombination rates are negligible. By reducing the active region volume, lowest thresholds can be achieved; however, the confinement factor also decreases. Hence, a characteristic active region volume exist where the threshold is minimal. For maximal miniaturization the optical mode volume should also squeezed to retain high optical confinement factor, while the modal loses should be low.

In the conventional Fabry-Pérot model, losses are split between the average propagation losses $\langle a_i \rangle$ and the mirror losses a_m that take place at the facets of the end-mirrors. In PhC lasers, end-mirrors are not well-defined, and the mirror (scattering) losses are expressed in terms of the intrinsic Q-factor of the cavity. Any loss channel, a_i, can be associated with a corresponding Q-factor, Q_i, using eq. 4.6.

4.1.2 Modified Rate Equations for Optical Pumping

In the optical pumping scheme, the laser rate equations of eq. 4.1 are modified in terms of the carrier pumping rate R_{pump}, i.e., the first term of the right-hand side of eq. 4.1a. The pumping rate for both pumping methods is defined as:

$$R_{pump} = \begin{cases} \eta_i I/qV, & \text{for Electrical Pumping.} \\ \eta_{opt} P_{in}/\hbar\omega_p V, & \text{for Optical Pumping.} \end{cases} \tag{4.9}$$

where η_{opt} is the optical pumping efficiency, P_{in} is the optical incident pump power, and $\hbar\omega_p$ is the energy per pump photon.

4.1.3 Fitting the Laser Rate Equations

The laser rate equations are fitted to experimental data using standard curve fitting techniques (see Sec. 3.1.1). The main limitation of the method is the multiple unknown parameters that need to be fit, the combination of which produces non-unique solutions. Thus, the fitting parameter space is reduced to four quantities, namely, the injection efficiency, the collection efficiency, the Q-factor, and the β-factor, while the rest are considered constants and related to the material properties. In this work, the confinement factor is calculated rigorously via FDTD simulations of the optical field, and the Q-factor is experimentally determined using passive test structures.

The material constants used in the fittings are found in literature and are given in table 4.1. Assuming fixed material parameters for the different devices is an important assumption used for lack of a better alternative. In conventional microscopic laser theory, this is a good assumption, since representative material parameters can be extracted from long devices. In reality, these parameters are expected to greatly differ between small devices, where such an averaging is not reasonable.[3]

Table 4.1 | Material parameters used when fitting the laser rate equations to the experimental results. The parameters are taken from [82].

τ_r (ns)	τ_{nr} (ns)	g_0 (cm^{-1})	N_{tr} (cm^{-3})
2	10	2000	10^{18}

4.2 Small-Signal Analysis

In small-signal dynamics, we consider the response of the carrier and photon reservoir in response to a perturbation. For a sinusoidal current modulation, the transfer function of the laser $H(f)$ is effectively a second-order low-pass filter with a damped resonance close to the cut-off frequency. Due to parasitics effects, an additional pole is added, and the final response function is given by:[156]

$$H(f) = A \cdot \frac{f_r^2}{f_r^2 - f^2 + j\frac{f}{2\pi}\gamma} \cdot \frac{1}{1 + j\frac{f}{f_p}} \tag{4.10}$$

where f_r is the relaxation resonance frequency, γ is the damping factor, and f_p is the parasitic cut-off frequency. The scaling factor A is a fitting parameter since the absolute level of the measured S_{21} response depends on the collected signal's intensity. The resonance frequency is given by:[82]

$$f_r = \frac{1}{2\pi}\sqrt{\eta_i \frac{\Gamma u_g}{qV}\left(\frac{dg}{dN}\right)(I - I_{th})} = D \cdot \sqrt{I - I_{th}} \tag{4.11}$$

where dg/dN the differential gain and D is the D-factor indicating the efficiency of the modulation speed. In this expression, the gain suppression is neglected. Moreover, the damping factor γ in eq. 4.10 is given by:[82]

$$\gamma = K f_r^2 + \gamma_0 \tag{4.12}$$

where γ_0 is the damping offset, and K is the K-factor that is described by:[156]

$$K = 4\pi^2 \tau_p \left(1 + \frac{\epsilon\Gamma}{dg/dN}\right) \tag{4.13}$$

[3] For example, the non-radiative recombination lifetime depends on local defects formed during the epitaxial growth.

where ϵ is the gain compression factor. The K-factor describes the damping of the response and thus is an important parameter for high-speed lasers.

The D- and K-factors are related to the intrinsic laser parameters, and thus its intrinsic response; however, as a semiconductor junction, the laser is expected to exhibit another cut-off frequency f_p from parasitic resistance due to contacts, the capacitance of the junction and the shunt resistance due to possible leakage. This parasitic frequency is associated with the commonly known RC time constant, as $\tau_{RC} = RC = 2\pi/f_p$.

4.3 Finite-Difference Time-Domain Simulations

The optical properties of a PhC cavity, like the mode structure, the quality factors, and the field profiles, are crucial determinants of laser performance, and their calculation requires the solution of the Maxwell equations in arbitrary geometries. Various finite-elements methods can solve the Maxwell equations numerically. In this project, the properties of PhC cavities are simulated using the Finite-Difference Time-Domain (FDTD) method[162] via the commercial software *Ansys Lumerical*.[163] FDTD is a powerful tool used to solve the Maxwell equations in differential form,[164] where the temporal evolution of propagating electromagnetic fields is simulated, and Fourier transforms are used to calculate the spectral response. During this project, 3D FDTD simulations were used to design PhC laser cavities and extract relevant PhC laser parameters in conjunction with experiments. Fig. 4.1(a-b) shows a typical simulation setup for a PhC laser cavity featuring a p-i-n and a BH structure. Typical components of the simulation setup include the PhC structure under test, the simulation domain and mesh, the excitation sources, and the different monitor types.

Materials and PhC structure: First, an InP slab of 250 nm is created, and air holes are periodically placed to create a triangular PhC lattice. The lattice constant a is chosen as 440 nm, while the hole radius r is varied to tune the resonant frequency of the cavity. The refractive index of InP is chosen as 3.17 and is considered constant for all frequencies to decrease the memory requirements of the simulation. In reality, the real part of the refractive index of passive InP is wavelength-dependent, ranging around 3.16 to 3.17 following the Sellmeier formula of Pettit and Turner;[165] however, the samples are slightly n-doped and a higher refractive index is expected.[166] Design optimizations are typically done on passive PhC cavities. The simulations can be expanded to model absorbing materials like p-doped InP using a complex refractive index as discussed in Ch. 5.3, or the effective refractive index of the BH layer as discussed in Ch. 7.2. Furthermore, FDTD simulations are also used prior to fabrication to choose the e-beam PhC mask parameters (a, r) based on the emission peak of the active layer and the membrane thickness of the specific sample.

Excitation source: FDTD simulations require a light source to create an initial electromagnetic field that will excite the system. The simplest source to excite the

modes of an optical cavity is a dipole point source that simulates a quantum emitter. The polarization of the dipole source should match the TE-like modes of the PhC cavity. Thus, a magnetic dipole oriented in the z-direction is chosen as depicted in Fig. 4.1(a). The excitation strength for each mode depends on the overlap of the dipole with the mode, which is an issue only if the dipole is placed on a node of the field. Typically, multiple dipoles are placed at random positions avoiding high symmetry points. Furthermore, the dipole bandwidth can be tailored to match the expected spectral range of the mode structure. In advanced calculations, a single mode can be excited with a sufficiently narrow dipole bandwidth; however, this also means a long excitation pulse requiring longer simulation time.

Domain size and PMLs: The PhC bandgap prevents any light leakage in the lateral direction. However, at least 10 and 8 mirrorholes are needed in the x- and y-direction, respectively, to confine light in-plane, making vertical scattering the only loss mechanism ($Q_{tot} \simeq Q_{ver}$). The simulation domain is truncated using perfectly matched layers (PMLs) to completely absorb incident light, simulating a system with open boundaries. Placing the PML boundaries close to a scattering element, e.g., a PhC hole, can absorb local evanescent fields making the simulation diverge. Thus, the PML was placed one period away from the last PhC hole in the lateral direction. In the vertical direction, the PML should be placed more than $\lambda/2$ away from the membrane [Fig. 4.1(b)], because it can absorb the non-propagating cavity modes and affect Q-factor results. The domain volume is then $D_x D_y D_z$, where D_i is the domain size in the i-direction.

Meshing and index monitor: Lumerical's *FDTD solutions* use a non-uniform mesh that is calculated based on the refractive index variations and whose density can be adjusted. However, the PhC properties stem from the periodicity of the refractive index, and consistent results require identical PhC hole shapes throughout the lattice. Thus, the mesh should be adjusted to feature an integer number of mesh cells per lattice constant in the x- and y-directions. Thus, we define a mesh resolution M_{res}, where the in-plane mesh step is defined as $dx = a/M_{res}$, and $dy = \sqrt{3}a/2M_{res}$. To verify that the meshing follows the periodicity of the PhC lattice, the holes' shape should be inspected via the index monitor shown in Fig. ref4.1(c). The mesh resolution is typically chosen as 14. In the z-direction, the structure is non-periodic (air-slab-air), and the default mesh can be used at a moderate accuracy setting (4 or 5).

Boundary conditions: The electromagnetic field profiles of LD modes follow symmetry conditions as illustrated in [68]. This inherent property of PhC modes can be exploited to significantly reduce computational time. The center of the PhC cavity should be placed in the middle of the simulation region where the symmetry planes of the field profiles are located. In the z-direction, a symmetric boundary condition is used to excite all the TE-like guided modes supported in the triangular PhC lattice. Cavity modes have a specific parity along the x-z and y-z planes, and boundary con-

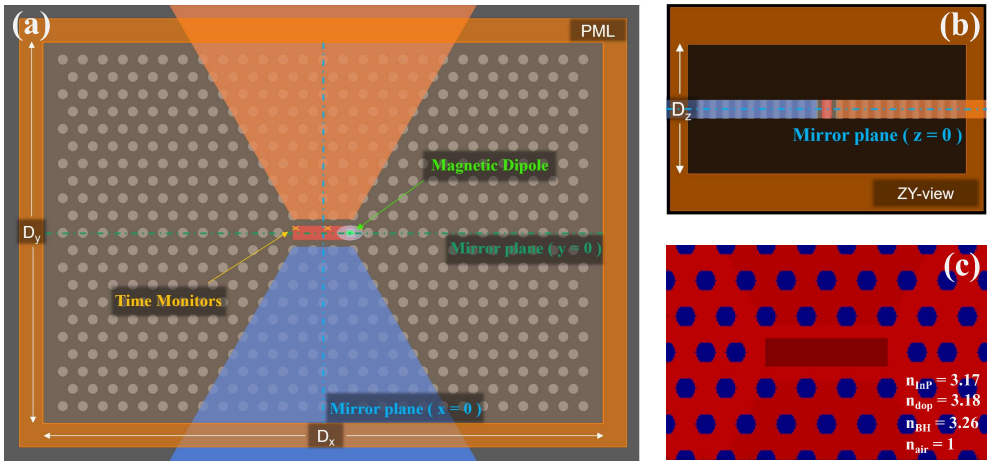

Figure 4.1 | 3D-FDTD simulation setup: (a) The top-view of the simulation setup for a PhC laser cavity featuring a p-i-n structure and a BH region. (b) The ZY-view of the simulation. (c) The index monitor of the device showcasing the meshing and the different refractive index materials.

ditions should be chosen accordingly. The blue and green solid lines in Fig. ref4.1(a) represent the x-z and y-z mirror planes, respectively. The E_y field of the fundamental mode of an odd (even) LD cavity is symmetric (anti-symmetric) with respect to the x-z mirror plane, while the E_x is always anti-symmetric along the y-z mirror plane.[4] Boundary conditions can reduce the computational volume and time by a factor of eight - a factor of two for each plane, but completely suppresses modes of different parity. The in-plane symmetry conditions should be lifted to calculate the complete mode structure.

Q-factor: The Q-factor of PhC cavity modes can be calculated via the FDTD simulations via the built-in *Q-analysis* algorithm. Time monitors are used to measuring the field intensity over time and are placed at random positions in the cavity to avoid nodes of the field. For high-Q PhC cavity modes, the Q-factors are calculated using the slope of the field decay.[5] This is complicated because there are multiple resonant modes interfering. As a result, the field is Fourier transformed in the frequency domain to extract the resonant frequencies. Subsequently, a bandpass filter is applied for each mode, and the time-evolution is extracted by the inverse-Fourier transform of

[4]The definitions of the boundary conditions in FDTD can be found in `https://optics.ansys.com/hc/en-us/articles/360034382694-Symmetric-and-anti-symmetric-BCs-in-FDTD-and-MODE`

[5]For low-Q cavities, the field decays before the end of the simulation, and the Q-factor ($Q = \omega/\Delta\omega$) of each mode is extracted from the spectrum calculated via Fourier transforming the time-domain field signal. The resolution of the spectrum is limited by the total simulation time ($\Delta\omega = 1/\tau_{sim}$). Due to unreasonable computational time, this method is limited to Q-factors below 1000 and, thus, was not used in the project.

the filtered spectrum. In this process, the resonant frequency is calculated with great accuracy even with short simulation times; however, the Q-factor calculation is not as robust, and great care is needed for precise calculations.[167] For better accuracy in the Q-factor, a long simulation time is needed, while the background modes can be suppressed via symmetry conditions. As a rule of thumb, 2 ps are enough to calculate the resonant frequencies. In comparison, above 6 ps are required for calculating the Q-factor in high Q-cavities. For ultra-high Q-factor calculations ($Q > 10^6$), more than 15 ps should be used. For advanced calculations, the excitation source spectrum can be tailored to match the resonant frequency and further suppress the background modes.

Field profiles: A 2D field monitor is positioned at $z = 0$ to extract the field profile of the cavity modes. The field intensity is calculated from the spectrum via a Fourier transform of the time evolution of the electromagnetic field in each position. The initial excitation pulse should be ignored by apodizing the monitor at the start of the simulation - ignoring the first 50 fs is typically enough. Furthermore, the field profiles are accurately calculated even at short simulation times ($\tau_{sim} < 2$ ps), making this simulation much cheaper compared to a Q-factor simulation. The simulation files with 2D monitors are typically large if the profiles of multiple frequency points are calculated. A workaround is to perform a quick Q-factor simulation ($\tau_{sim} = 2$ ps) to extract the resonant frequency of the desired modes and calculate only the desired field profiles in a subsequent simulation.

4.4 Summary

This chapter established the main theory used to model the static and dynamic behavior of the laser. The laser rate equations and the different physical parameters were introduced, i.e., the different recombination rates, the logarithmic gain model, the modal losses with their corresponding quality factor, and the laser threshold condition. In addition, the fundamental small-signal analysis was described to model the laser dynamics. Finally, a description of the finite-difference time-domain method used for simulating the optical properties of the photonic crystal cavities was given, introducing the various simulation components.

CHAPTER 5

Photonic Crystal Cavities for Laser Applications

5.1 Design Parameters of Photonic Crystal Cavities

Matching the resonant frequency of a resonator with the peak frequency of the active material's photoluminescence (PL) is a prerequisite to attaining high-performance lasers. That is particularly important when targeting a specific mode[1] in wavelength-scale PhC cavities since there is a large mode spacing. Tuning the cavity resonance requires adjustments to the PhC parameters, which will cause a deviation from the designed Q-factor. In this section, we investigate the different tuning mechanisms of a PhC cavity mode and the respective Q-factor uniformity.

Four primary parameters affect the PhC cavity resonance: the hole radius, the PhC lattice constant, the thickness of the PhC membrane, and the refractive index.

The hole radius and lattice constant. The main parameters for resonance tuning the PhC cavity design are the hole radius, r, and lattice constant, a. In Figs. 5.1(a_1-a_2), the effect of the (r, a) parameters on the resonant wavelength and Q-factor is illustrated. In this example, a modified[2] L3 cavity featuring a high Q-factor is used as a study case. Increasing the hole radius (lattice constant) will produce a blueshift (redshift) of the resonance due to the respective change in the effective refractive index. These effects counterbalance each other, and a given resonance can be attained with multiple (r, a) combinations. Furthermore, the Q-factor of a mode is also sensitive to the structural properties of the PhC cavity, especially in optimized designs. The sensitivity of the Q-factor on the (r, a) shifts can be considered a measure of design robustness. The absolute change of the Q-factor is much more prominent when shifting the radius compared to the lattice constant. Those effects are clearly illustrated in Figs. 5.1(b_1-ba_2), where a vertical (a_0 = 440 nm) and a horizontal (r_0 = 118 nm) cut of the 2D plots of Figs. 5.1(a_1-a_2) is shown. In

[1] Typically, we target the fundamental mode that exhibits the highest Q/V ratio.

[2] This cavity is modified by shifting the first end-holes away from the cavity by $S_{01} = 0.224a$, following the notation of section 5.2.

particular, the resonant shifts are linear, and the tuning rates $\Delta\lambda/\Delta r$ and $\Delta\lambda/\Delta a$ are calculated as -2.4 nm/nm and 3.5 nm/nm, respectively. The linearity is preserved locally, and the rates are slightly dependent on the mode profile. Furthermore, the relative deviation from the designed Q-factor ($\delta Q/Q_{des}^{(r_0,a_0)}$) is represented in the right

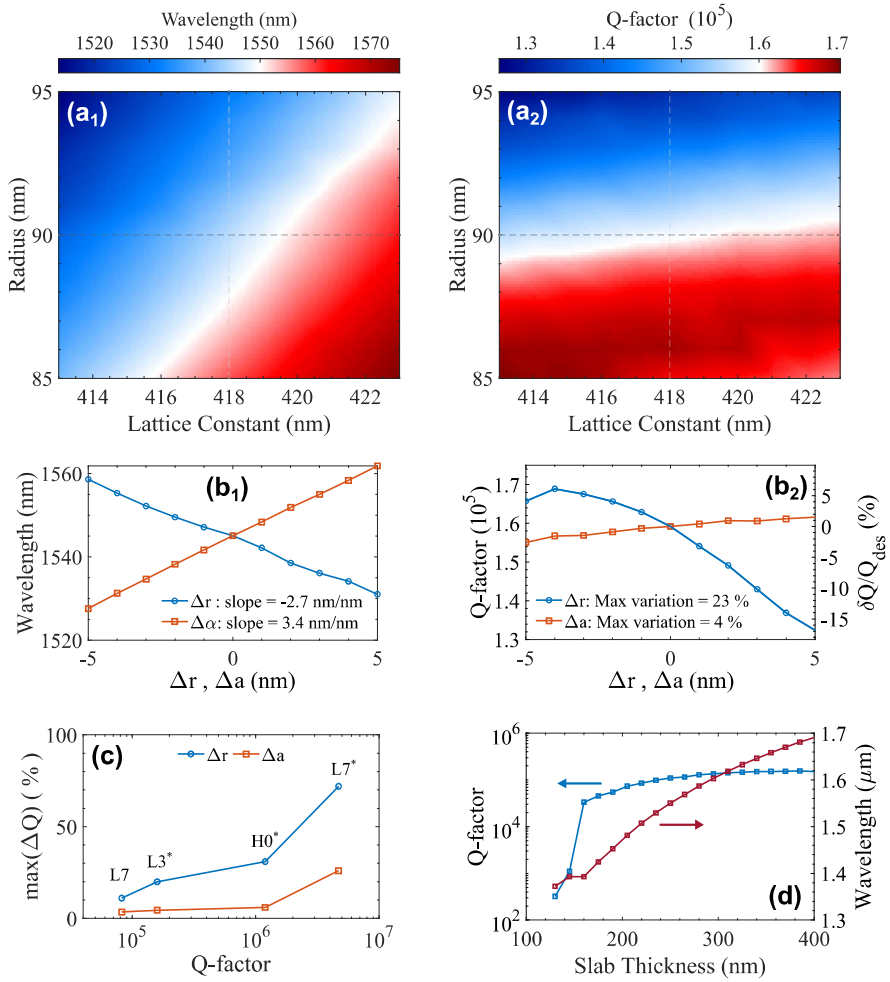

Figure 5.1 | The effect of radius, lattice constant and membrane thickness on the resonance and Q-factor. (a) A 2D plot of the resonant wavelength (a_1) and the Q-factor (a_2) of the fundamental mode of an optimized L3 cavity versus the lattice constant and the hole radius. (b_1-b_2) A horizontal (Δa) and vertical (Δr) cut of figures a_1 and a_2. (c) The maximum relative deviation from the designed Q-factor for a 20 nm resonance tuning for different cavity designs. (d) The Q-factor and wavelength dependence on the PhC membrane thickness.

axis of Fig. 5.1(ba$_2$) further highlighting the sensitivity of the designed Q-factor on radius.

The robustness of the Q-factor on the (r, a) parameters is further investigated by studying four different cavity designs with varying degrees of Q-factor optimization. Fig. 5.1(c) shows the maximum deviation of the designed Q-factor for four cavity designs when shifting the radius or lattice constant to achieve a 20 nm detuning, expressed as $\Delta Q = max\{(Q_{des} - Q/Q_{des})\}$. In particular, a standard L7 cavity and optimized L3, H0, and L7 cavities are considered. The redshift rates, $\Delta\lambda/\Delta a$, for all designs are similar (3.4-3.5 nm/nm), while the blueshift rates, $\Delta\lambda/\Delta r$, are increasing for smaller mode volumes as -2.4, -2.7 and -3.8 nm/nm for the L7s, L3 and H0 cavities, respectively. In all cases, the overall design robustness is inversely proportional to the degree of Q-factor optimization, while the Q-factor is more sensitive to radius shifts. The increased radius sensitivity partially stems from the fact that hole position shifts are scaled with the lattice constant. However, more importantly, it is because the PhC properties scale with $R = (r/a)$.[168] Specifically, for similar $(\Delta r, \Delta a)$ shifts, $\Delta R/\Delta a \ll \Delta R/\Delta r$.

To verify this effect, The bandgap of a triangular PhC structure is simulated using a 2.5D variational FDTD solver. The simulation setup is shown in Fig. 5.2(a), where a broadband source is injected in a wire waveguide. The light propagates through the PhC structure, and the transmission spectrum is measured via a field monitor. Most of the transmitted light is measured in the output wire waveguide.

The transmission spectrum for different PhC hole radii and lattice constants is shown in Fig. 5.2(a) and Fig. 5.2(b), respectively. The dip in the transmission spectrum indicates the projection of the PhC bandgap along the $\Gamma - K$ direction. The PhC bandgap is mainly determined by the (r/a) ratio,,[168] and thus, the radius will affect the bandgap size more than the lattice constant for similar shifts. In addition, the resonant wavelength of the fundamental mode of the optimized L3 cavity is superimposed in Figs. 5.2(b-c), indicating a significant mismatch between the shift of the bandgap's center wavelength and the cavity's resonant wavelength. For a small r/a ratio ($r/a < 0.19$), the bandgap is minuscule, and the modes lie within the band edge resulting in weak lateral confinement.

Overall, in a fabrication process with good control and reproducibility, the PhC hole radius would be fixed with a process flow optimized for a given radius, while the lattice constant would be shifted for tuning. Using the lattice constant as a tuning parameter would produce an extensive tuning range with better Q-factor uniformity. However, precise control of the radius has yet to be achieved since our fabrication process is limited by the etching uniformity across the wafer, while the cleanliness and usage history of the equipment may limit the reproducibility between different fabrication runs. As a result, resonance tuning was performed throughout this project via radius shifts to minimize the risk.

The slab thickness. The membrane thickness of a PhC cavity also affects the modal properties. Fig. 5.1(d) illustrates the resonant wavelength and the Q-factor of an optimized L3 cavity as a function of the slab thickness. The wavelength is approximately

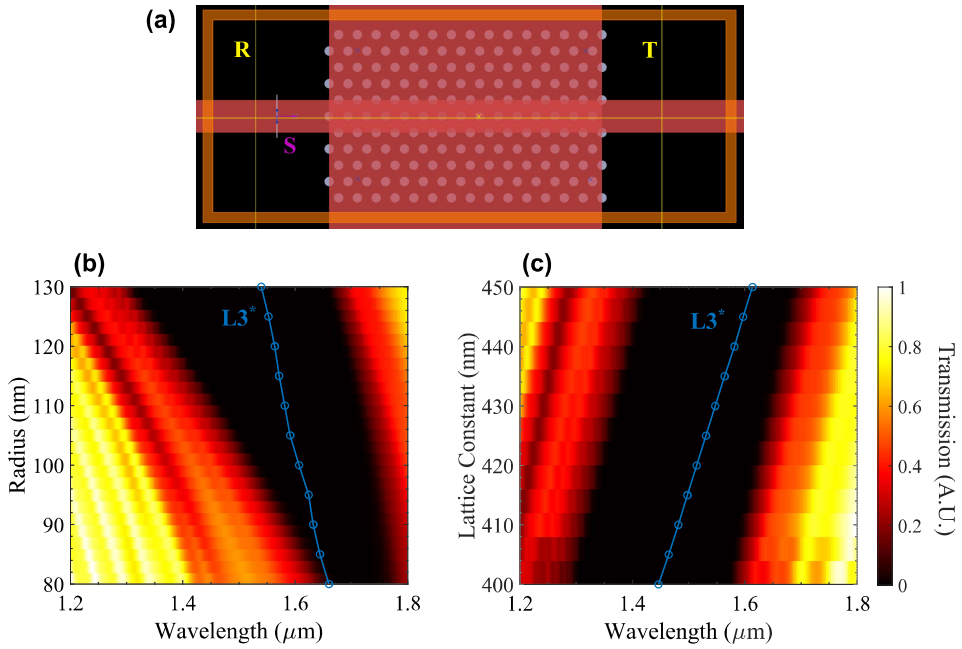

Figure 5.2 | PhC bandgap calculation for different $(\mathbf{r}, \mathbf{a})$ variations. (a) The 2.5D FDTD simulation setup. (b) Transmission spectrum versus the PhC hole radius ($a = 440$ nm). (c) Transmission spectrum versus the PhC lattice constant ($r = 110$ nm). The resonant wavelength of an optimized L3 cavity is drawn in blue.

linear around a slab thickness of 250 nm and is estimated as $\Delta\lambda/\Delta t_{slab} \sim 1.5$ nm/nm. The slab thickness varies across the wafer, exhibiting a wafer uniformity of 10 nm due to variations during growth. As a result, the membrane thickness is measured via ellipsometry, and the PhC design parameters (r, a) are adjusted accordingly to tune the cavity. The slab thickness does not drastically affect the Q-factor; however, a minimum thickness exists below which the bandgap is minuscule, and the PhC modes will be weakly guided ($t_{slab} \gtrapprox \lambda/4n_{eff}$).[169] On the other hand, a thicker membrane will extend the profile in the z-direction, reducing the confinement factor.

The refractive index. The refractive indices of the materials constituting the PhC structure are chosen based on the application. In our process, we are working on air-suspended PhC membranes, where the high- and low-index dielectric materials are InP and air, respectively. As a result, the refractive index is not considered a design parameter. However, the active material can substantially change the refractive index locally (see sec.7.2), which can change the dispersion of a PhC waveguide and significantly change the resonance of a PhC cavity. Furthermore, doping can also slightly increase the material's refractive index; however, this effect is typically

neglected.[3] For completeness, the wavelength shift rate due to the refractive index of the high-index dielectric material n_d is included in table 5.1 ; however, its practicality is limited since the effective index is dependent on the mode profile overlap with the different materials, and no global design rules can be applied.

The effect of all PhC parameters on the resonant wavelength is listed in 5.1. These numbers are based on L7 cavities. The blueshift due to radius shift is more prominent for shorter cavities, while the rest of the tuning rates are nearly cavity-independent.

The mirror losses for an L7 cavity are expected to be lower than 0.25 cm^{-1}

Table 5.1 | Design guide for resonance tuning. Approximate rates of resonance shift for PhC cavity modes.

$\Delta\lambda/\Delta r$	$\Delta\lambda/\Delta a$	$\Delta\lambda/\Delta t_{slab}$	$\Delta\lambda/\Delta n_d$
-[2.4, 3.7] nm/nm	3.5 nm/nm	1.5 nm/nm	4.65 nm/0.01

5.2 Quality Factor Optimization

Optimizing the Q-factor of the laser cavity is necessary for achieving low-power consumption as the laser threshold strongly depends on the total Q-factor of the cavity. The loaded Q-factor of a cavity should be designed to match specific application requirements; however, the intrinsic (unloaded) Q-factor of in-plane PhC cavities should always be maximal since vertically-leaking light is considered undesired optical loss. This section describes the optimization method used to achieve ultra-high Q-factors in PhC cavities.

For high Q-factor in small mode volume PhC cavities, the light should be gently confined as described in the seminal work of Akahane et al..[50] The term gentle confinement is understood as a slowly-varying electric field distribution of the cavity mode, with an envelope resembling a Gaussian function. Such mode profiles exhibit suppressed low spatial frequency components, i.e., field components that cannot be confined vertically by the total internal reflection at the slab-air interfaces. Optimizing the shape of the mode profile can be achieved by tapering the PhC mirror-holes in LD,[42],[50] or nanobeam cavities,[170] or by varying the lattice constant of a W1,[72],[73] of a modified PhC lattice,[171] or of a nanobeam wire waveguide,[172] to create an effective potential that supports modes with gaussian-like envelopes.

However, realizing ultra-high Q-factors by modifying the field profile in real space is increasingly hard for small cavities, and a systematic optimization method is needed. An extension of the gentle confinement principle is directly minimizing the field components within the light cone. An intuitive method is to visualize these leaky field components, identifying the leaky regions, and subsequently modifying the PhC environment in order to suppress the leakage as described by Nakamura et al..[173]

[3] Doping mainly affects the imaginary part of the refractive index due to free-carrier absorption.

This method was employed to increase the Q-factor PhC cavities throughout this project and was crucial to realize lasing of few-cell PhC cavities. Fig. 5.3 depicts the Q-factor optimization of an L3-InP-based cavity that was required to realize an electrically-driven L3 laser.[46] The optimization steps of this method are:

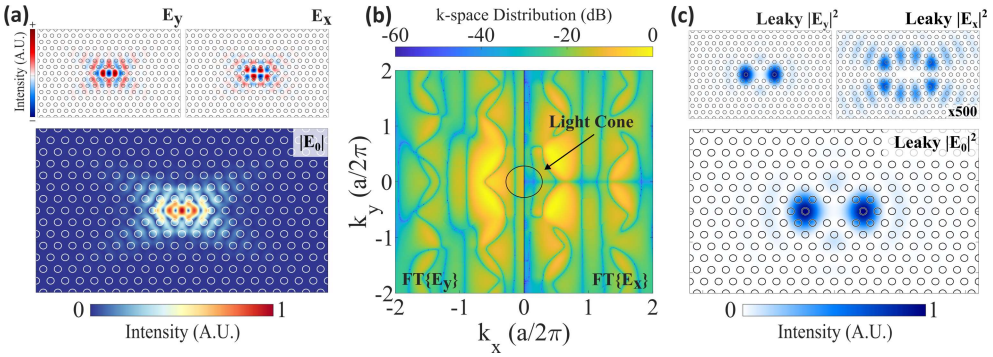

Figure 5.3 | Visualization of the leaky field components. (a) The electric field profile $|E_0|$ of an L3 cavity (bottom), and the E_y (top left) and E_x (top right) components. The PhC holes are outlined in black. (b) The k-space distribution of the E_y (left) and E_x (right) is obtained by a 2D Fourier transform. (c) The leaky field components of the $|E_y|^2$ (top left), $|E_x|^2$ (top right) field obtained by an inverse Fourier transform of the light that lies within the light cone. The leaky part of the mode profile $|E_0^{leaky}|^2$ (bottom).

1. The electric field profile is calculated via 3D-FDTD simulations. The electric field profile $|E_0|$ of the fundamental mode of a standard L3 cavity is shown at the bottom of the figure of Fig. 5.3(a). The PhC lattice constant, radius, and slab thickness were chosen as 440 nm, 120 nm, and 250 nm, respectively, to realize a resonant wavelength at 1550 nm. The y- and x- components of the electric field are shown $E_{y,x}$ are depicted at the top left and top right figures of Fig. 5.3(a), respectively.

2. The $E_{y,x}$ field profiles are transformed in the reciprocal space (k-space) using a 2D fast Fourier Transform (FT), as shown in Fig. 5.3(b). Due to momentum conservation, light components within the light cone are coupled to the radiation modes ($|k_{||}| < 2\pi/\lambda_0$) and leak out of the cavity. These are considered the leaky field components.

3. The leaky field components of FT$\{E_{y,x}\}$ are transformed back to the real space using a 2D fast Inverse FT as depicted in Fig. 5.3(c), where the top-left and top-right figures show the leaky part of the E_y and E_x components. The bottom figure shows the total leaky field $|E_0^{leaky}|$, which reveals the leaky region of the structure.

4. The PhC holes positions in the vicinity of the leaky region are optimized to maximize the Q-factor. The Q-factor optimization is done using successive

scans of the position of a single hole. This step completes one optimization round.

5. Steps 1-4 are repeated to reveal and modify the PhC environment around the next leaky region.

The leaky field profile of the standard L3 cavity reveals that the principal radiation loss comes from the scattering of the E_y at the first mirrorhole[4]. This is also in accordance with the conventional FP picture,[65],[174] where light propagates along the W1 waveguide and is scattered at the first mirror-hole. However, after this initial optimization round, it is difficult to predict which PhC mirror-hole position should be adjusted, and the visualization of the leaky field is crucial.

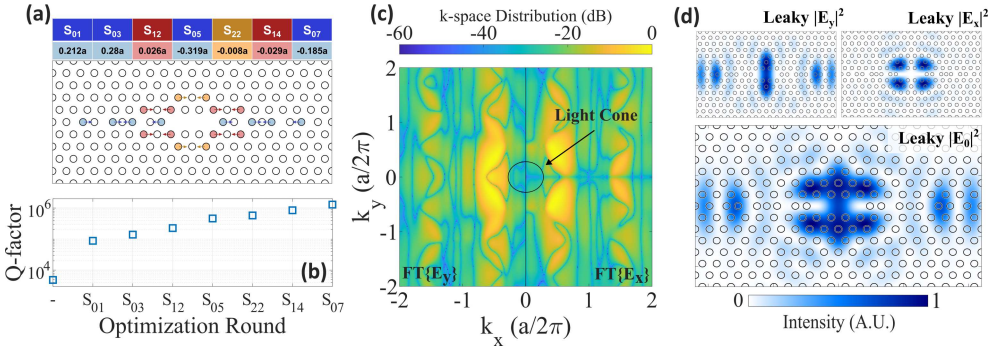

Figure 5.4 | Q-factor optimization of an L3 cavity. (a) Optimized positions of seven symmetrical PhC holes for ultra-high Q-factor. The shift of the j$^{\text{th}}$ hole in the i$^{\text{th}}$ row is denoted as S_{ij}. (b) The Q-factor after each subsequent optimization round. (c) The k-space distribution of the E_y (left) and E_x (right). The leaky field components of the $|E_y|^2$ (top left), $|E_x|^2$ (top right), and $|E_0^{leaky}|^2$ (bottom), after the 7$^{\text{th}}$ optimization rounds.

Fig. 5.4(a) depicts all the PhC holes that are shifted to optimize the Q-factor of an L3 cavity. The optimal hole position shifts are included in Fig. 5.4(a) and are denoted as S_{ij}, where i represents the number of PhC row away from the cavity, while j is the hole number from the center of the $x-z$ symmetry plane. S_{ij} are positive when holes are shifted away from the $x-z$ plane along the $K-\Gamma$ direction.

The Q-factor was improved from 5000 to $1.1 \cdot 10^6$ after seven optimization rounds, as shown in Fig. 5.4(b). Furthermore, the electric field profile and the mode volume are not significantly altered; however, the components that lie within the light cone are significantly suppressed as depicted in Fig. 5.4(b), where the k-distribution for both is E_y and E_x is illustrated. Fig. 5.4(c) shows the leaky field components, where the leakage from the E_y and E_x field is comparable and extended over a wider region, making it hard to predict which hole position can be optimized.

[4]The leaky field intensity of E_x of Fig. 5.3(c) is scaled (x500) to be comparable with the E_y field.

The field profile simulations require both high resolution and a large domain size because the resolution of the field profile in the reciprocal space is inversely proportional to the domain size in real space ($\Delta k_i \propto 1/D_i$). At the same time, the range of the calculated k-space is inversely proportional to the real-space resolution as $K_i \propto 1/\Delta x_i$. Nevertheless, these simulations are cheap since the mode profile and the resonance frequency can be calculated accurately without requiring the long simulation times typically needed for precise Q-factor calculations.

Generally, this optimization method is intuitive and substantially decreases the total simulation time by narrowing down the number of PhC holes that need to be adjusted in each optimization round. Moreover, the process is deterministic, which is disadvantageous since it leads to a local maximum of the Q-factor. Increasing the randomness using particle swarm optimization algorithms[175] can be a workaround while still benefiting from identifying the leaky region. However, the most significant improvement to this method is to bypass the expensive Q-factor maximization in each optimization round by building an algorithm based on minimizing the k-space components in the light cone that require only cheap field profile calculations.

Alternative Q-factor optimization techniques have also proven very successful. Ultra-high Q-factor cavities have been designed[176] and demonstrated[143] using the guided-mode expansion method[177] combined with a genetic optimization algorithm.[178] In addition, heterostructure cavities with Q-factors in the order of one billion have been designed using deep-learning.[179] However, the value of such advanced algorithms may be limited since technological challenges in InP processing, doped-induced losses, and application requirements are expected to hinder the realization of ultra-high Q-factor cavities in realistic devices.

A better approach is to optimize a different figure of merit to target specific laser characteristics, e.g., the laser threshold. For example, inverse design by topology optimization[180] has been used to maximize the local density of states rather than the Q-factor. With this approach, a dielectric cavity design exhibiting deep sub-wavelength confinement and moderate Q-factors has been realized[181] and was experimentally demonstrated,[154] achieving a two-orders of magnitude higher Q/V ratio, than regular PhC cavities. The same principle can be applied in lasers, where the figure of merit should involve decreasing the active material volume while maintaining high Q- and Γ-factors.

5.3 The Effect of Disorder and Doping

The Q-factor of a laser cavity quantifies the temporal confinement of the photons and is a parameter that affects the laser threshold, the linewidth, the modulation speed, and the outcoupling efficiency. The total Q-factor of a cavity is determined by all the different loss channels, like scattering due to fabrication imperfections and material absorption. There are multiple demonstrations of Si-based PhC cavities exhibiting ultra-high Q-factor and wavelength-scale mode volumes enabled by the maturity of CMOS processing.[42],[74],[75],[143],[182] In contrast, the Q-factor of InP-based

PhC cavities was limited to a few 10,000 due to fabrication imperfections,[183],[184] and only recently high-Q PhC cavities have been realized, surpassing the 100,000 milestone.[185],[186] Furthermore, the Q-factor of electrically-driven PhC devices is expected to be limited by doping-induced optical absorption; however, this effect has been greatly overlooked in the literature. This section investigates the effect of disorder and doping on InP-based PhC cavities.

Initially, Monte Carlo (MC) simulations were conducted to get a quantitative understanding of the effect of the disorder. The radius of each hole constituting an L3 cavity was randomly varied using a standard deviation $\sigma_r = 1.5$ nm, the typical value extracted from SEM. Three different cavity L3 designs optimized for different Q-factor, and an ensemble of 40 cavities for each design was considered. All cavities were centered around 1550 nm. Fig. 5.5(a) shows the average Q-factor of the cavities, including disorder and its standard deviation (std.). Furthermore, the standard deviation of the resonant wavelength is also shown. As a reference, the Q-factor of the unperturbed design is given. The comparison shows that the cavities optimized for higher Q-factor are more sensitive to disorder, limiting the highest attainable Q-factor. In contrast, the resonant wavelength seems reasonably robust, showcasing a minimal standard deviation of 0.75 nm.

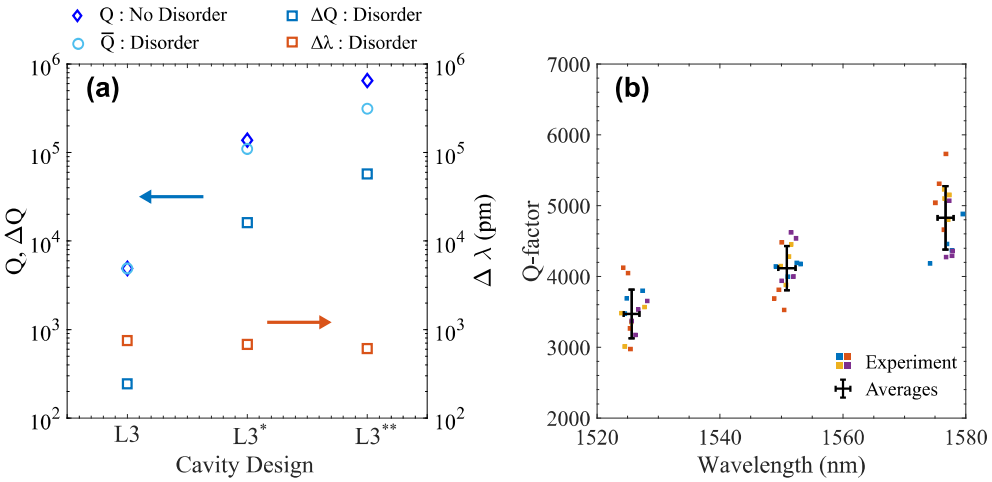

Figure 5.5 | Disorder of L3 cavities. (a) Simulated characteristics of different L3 cavity designs using Monte Carlo simulations ($\sigma_r = 1.5$ nm). (b) Q-factor as a function of the resonant wavelength for the fundamental mode of fabricated L3 cavities.

Secondly, the Q-factor and the resonant wavelength of standard L3 cavities were measured as shown in Fig. 5.5(b). In this experiment, the design was detuned by shifting the radius of the PhC. Sixteen identical designs placed in four different regions on the chip were measured. The Q-factor std. is 450, which is very close to the MC simulations, while the std. of the resonant wavelength was found to be 1.3 nm, which is higher than the value found by the MC simulations. However, the spread of the

resonant wavelength is similar in experiment and simulations, which suggest that this discrepancy is due to the limited number of measured devices. The low Q-factors of the standard L3 cavities make them robust for this level of disorder.

To generalize and quantify the effect of disorder and doping, another experiment was conducted, where the Q-factor of LD cavities of various lengths was measured. Fig 5.6(a) depicts the spectrum of an L9 cavity measured by cross-polarization resonant scattering spectroscopy as described in section 3.4. Fitting a Fano lineshape to the experimental data, the Q-factor of the cavity was calculated as 93,000 ($Q = \lambda_0/\Delta\lambda$). However, the Q-factor was expected to be 213,000 from FDTD simulations, indicating significant loss due to fabrication disorder. Furthermore, the effect of doping in an LD laser was studied by characterizing LD cavities featuring the p-i-n doping profile similar to that of the PhC laser structures. Fig. 5.6(b) shows the Q-factor of LD cavities of different lengths. The blue, orange and yellow markers indicate the Q-factor of simulated, undoped, and doped PhC cavities.

The total Q-factor of a PhC cavity is dependent on the different loss mechanisms and can be written as:

$$\frac{1}{Q_{tot}} = \underbrace{\frac{1}{Q_{int}} + \frac{1}{Q_{dis}}}_{1/Q_v} + \frac{1}{Q_{abs}} \tag{5.1}$$

where Q_{int} is the theoretical Q-factor extracted by FDTD simulations, Q_{dis} represents the disorder Q-factor associated with the scattering losses due to structural imperfections, and Q_{abs} is the Q-factor associated with optical absorption due to p-doping. For undoped cavities, $Q_{abs}^{-1} = 0$, and the total Q-factor equals Q_v, representing the vertical Q-factor of a fabricated cavity. For doped cavities, the optical absorption due to n-dopants is neglected since the n-doping absorption coefficient is expected to be much lower than this of p-doping.[21]

Equation 5.1 was used to quantify the effect of disorder and doping in undoped and doped cavities. First, a fit on the undoped cavities using the simulated data and a cavity-length independent value for Q_{dis}. The solid red line of Fig. 5.6(b) shows the theoretical fit, where Q_{dis} is estimated at 120,000, which is dependent on the surface roughness and disorder of the etched PhC holes. Consecutively, Q_{abs} was extracted from fitting Eq. 5.1 on the experimental data of doped cavities and the previously calculated Q_{dis}. The solid red line of Fig. 5.6(b), Q_{abs} was estimated at 21,000 and is dependent on the proximity of the doping profile and the doping concentration. Both fits show good agreement of the theory with the experimental data. However, the Q-factor of shorter cavities is overestimated since the field overlaps more with the holes enhancing the scattering losses due to disorder. Furthermore, the Q-factor of doped L8 and L9 cavities could not be measured due to low contrast, i.e., a broad resonant peak (low-Q_{tot}) hidden in the background due to poor coupling efficiency (high-Q_v).

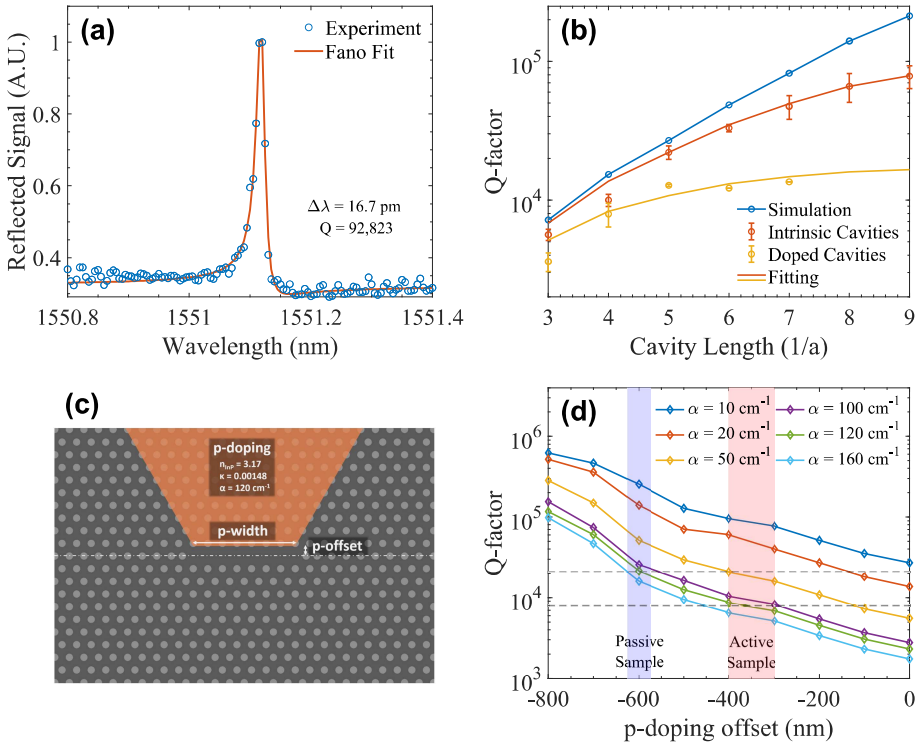

Figure 5.6 | Q-factor optimization of an L3 cavity. (a) Optimized positions of seven PhC holes for ultra-high Q-factor. The shift of the j$^{\text{th}}$ hole in the i$^{\text{th}}$ row is denoted as S_{ij}. (b) The Q-factor after each subsequent optimization round. (c) The k-space distribution of the E_y (left) and E_x (right). The leaky field components of the $|E_y|^2$ (top left), $|E_x|^2$ (top right), and $|E_0^{leaky}|2$ (bottom), after the 7$^{\text{th}}$ optimization rounds.

Using the experimentally determined Q_{abs}, the p-doping absorption coefficient can be estimated via 3D-FDTD simulations. Fig. 5.1(c) shows the simulation setup, where an optimized L7 cavity[5] features the p-doping profile whose offset from the cavity center can be varied. The p-InP has been modeled using a complex refractive index $\tilde{n} = n + i\kappa$, where n and κ are real and imaginary parts of the refractive index, respectively. The imaginary part of the refractive index can be written as $\kappa = \alpha\lambda/4\pi$, where α is the absorption coefficient of the p-doping.[187] The absorption coefficient depends on the doping level.[188] In our fabrication process, we aim for a doping density of 10^{18} cm^{-3}; however, a direct measurement of the doping density has not been conducted. As a result, the simulations were performed for various absorption coefficients, as shown in Fig. 5.6(d), where the Q-factor of the cavity versus the

[5]The first mirror hole was shifted ($s_{01} = 0.225a$) to increase the Q-factor to 1 million. For realistic doping levels, $Q_{abs} \ll 10^5$, thus, Q_{abs} is extracted directly from the simulations as $Q_{tot} \simeq Q_{abs}$.

doping offset is illustrated. The Q-factor drops drastically as the p-doping profile approaches the cavity center, resembling a tri-exponential decay, that is related to the mode profile overlap with the lossy p-InP region.

The shaded blue and red region of Figure 5.6(d) shows the expected range of the p-doping offset for the passive and BH samples, respectively. The p-doping profile offset for the passive samples has been determined as 600 nm corresponding to a p-doping absorption coefficient of 120 cm^{-1} ($\kappa = 0.00148$), which suggests that the p-doping density is higher than expected. Finally, the internal absorption loss of the laser cavity is calculated. Using SEM imaging on active cavities, the p-doping offset was estimated at 350 nm,[6] leading to a Q_{abs} of 8,000. This corresponds to an average internal modal loss a_i of 17 cm^{-1}, calculated using the expression:[73]

$$Q_{abs} = \frac{k}{a_i} = \frac{2\pi n_{eff}}{a_i \lambda} \tag{5.2}$$

where k is the wavevector, n_{eff} is the effective refractive index, and λ is the resonant wavelength of the mode. The effective refractive index is calculated as 3.37.

Overall, the total Q-factor of the *intrinsic* laser cavities is limited by the p-doping and should be around 8,000. Such a high absorption loss limits the output power and increases the threshold current, before dropping the Q-factor further by adding an output waveguide. As a rule of thumb, we have observed that the total Q-factor of cavities should exceed 4,000 to achieve lasing.[7] The Q-factor increases exponentially with the doping offset; however, the leakage current increases as well, and an optimum p-doping distance should exist. Furthermore, the doping concentration has yet to be optimized since the wafers are doped on a wafer level, and massive resources should be expended on fabrication and testing.

5.4 Summary

In this Chapter, the properties of PhC cavities were studied. Firstly, a numerical investigation was conducted on the effect of the PhC radius, lattice constant, and slab thickness on the PhC cavities. Furthermore, as a design guide for PhC cavities. Furthermore, the Q-factor optimization method used throughout the project was established; this method is based on the visualization of the leaky components method, and its advantages and disadvantages were given. Finally, the effect of the disorder and the doping losses were quantified. In particular, we showed that the intrinsic Q-factor of the passive cavities was capped at 120,000 due to fabrication imperfections; however, the doping-induced losses are the main limitation for optical cavities used in laser applications. The absorption coefficient of the p-InP was also determined at 120 cm^{-1}.

[6] The p-doping profiles is extended on the BH samples and features some random wavy patterns at the p-i interface, as discussed in section 2.3.

[7] This estimate was deduced from the shorter standard LD device that achieved lasing (L4) for 1QW and 3QWs lasers.

CHAPTER 6

Electrically-driven Photonic Crystal Lasers

In this chapter, the properties of electrically-driven PhC lasers are described. The results include the static and thermal properties, the comparison between optical and electrical pumping, and the leakage current.

6.1 Static Characteristics

The static properties of the PhC lasers were characterized at room temperature using the Laser Setup described in section 3.1. Fig. 6.1 shows the static characteristics of an L3-based laser. The intrinsic Q-factor of the PhC cavity has been increased to about a million using the optimization process described in section 5.2. In Fig. 6.1(a), the power of the collected output light versus the injected current and the drive voltage versus the injected current (LIV-curve) is depicted. The inset of 6.1(a) shows the output power around the laser threshold. The device exhibits an ultra-low threshold current of 10.2 µA, extracted by the superimposed two-line segmented fit. The device also operates at CMOS-compatible drive voltage. Comparing the IV characteristics of similarly designed PhC lasers from NTT shows that our lasers have lower resistance, which is likely related to the addition of the InGaAs layer under the p-contact, increasing its quality or to a higher level of doping.

The laser is single-moded, emitting around 1540 nm. In Fig. 6.1(b), the laser spectrum at a pumping current of 100 µA is shown. The laser wavelength and linewidth evolution with respect to the injected current is depicted in Fig. 6.1(c). In the spontaneous emission regime, the resonant wavelength blueshifts due to the carrier-filling effect.[189] Above the threshold, the quasi-Fermi levels are pinned, and the wavelength redshifts due to heating induced by optical power circulating the cavity. Similarly, the linewidth saturates at the laser threshold, limited by the resolution of the OSA.

Finally, the differential resistance of the laser as a function of the current is illustrated in Fig. 6.1(d). The differential resistance ranges from a few to tens of kΩ. At low injection currents, the differential resistance can reach up to 100 kΩ, while for large input currents, it saturates to around 4 $k\Omega$. The differential resistance is

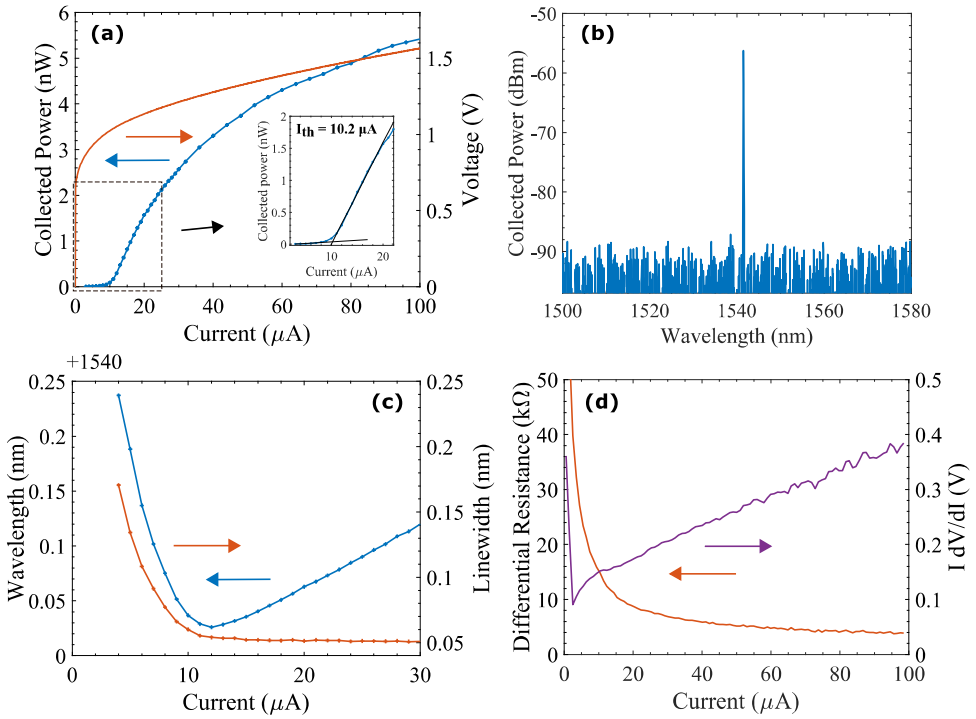

Figure 6.1 | Electro-optical characterization of an L3-type laser at continuous-wave room-temperature operation. (a) Collected output power and applied voltage as a function of injected current. Inset: A two-segment line fit for calculating the laser threshold current. (b) The laser spectrum at 100 µA injection current. (c) The center wavelength and the linewidth of the emission peak as a function of the injection current. (d) The differential resistance and the scaled differential voltage (IdV/dI) as a function of the laser current.

useful since it can be used to estimate the injected currents applied from an AC voltage source during the RF modulation of the laser. Furthermore, IdI/dV is plotted against the injected current, where an apparent kink is observed around the threshold. The applied voltage is the sum of the resistive components of the device and the internal quasi-Fermi level separation. Above the threshold, the quasi-Fermi level separation is constant, and thus the slope of IdI/dV is decreased.[110],[190]

For this first generation of devices, an efficient outcoupling scheme was omitted to increase the device density. In addition, the complexity is reduced since there is no need to decouple the intrinsic Q-factor from a loaded Q-factor, which enables robust analysis of the laser performance. On the other hand, the external quantum efficiency and the wall-plug efficiency cannot be measured directly. The low collected power also prohibits sensitive measurements like intensity-noise and linewidth measurements. The second generation of devices should include cavity designs with far-field and Q-factor optimization,[141] or output waveguides connected to miniaturized Bragg

gratings,.[153] In the third generation of devices, evanescent coupling to a Si output waveguide should be included.[44],[45]

6.2 Thermal Properties

The temperature is an important parameter that affects laser characteristics like the laser threshold, the slope efficiency, and the service life of the laser. Since computer chips can reach high temperatures, it is crucial to characterize the thermal behavior of lasers intended for on-chip applications. A series of measurements were conducted to understand the thermal properties of the laser in terms of self-heating and with respect to ambient temperature. Fig. 6.2(a) shows the L-I characteristic curve of an 3-QW L7 laser for different heat sink temperatures. Lasing is observed up to 79 °C, which is the limit of the TEC used in these experiments.

The laser resonant wavelength shows a linear dependence with temperature, as depicted in Fig. 6.2(b). The 1-QW and 3-QW lasers show a similar slope of 0.11 nm/K and 0.10 nm, respectively. The observed linear increase is attributed to a corresponding increase of the refractive index.[191] Subsequently, the laser wavelength shift under varying injected currents can be used to estimate the self-heating of the laser. Fig. 6.2(c) depicts the calculated temperature increase of the active region, exhibiting less than 8.5°C heating at 150 µA with a slope of 84 K/mA for both 1-QW and 3-QW lasers. Such minimal self-heating is another advantage of the BH technology since InP has much higher thermal conductivity than the InGaAsP active region ($k_{\mathrm{InP}} \simeq 68$ W m^{-1}K^{-1}; $k_{\mathrm{InGaAsP}} \simeq 4.2$ W m^{-1}K^{-1}).[192] The source of self-heating was initially thought to be related to the dissipated power due to ohmic heating; however, it was later proven that it is mainly generated by the high optical power density circulating the cavity, as is discussed in the following Sec. 6.3. Furthermore, smaller lower-power lasers operate at lower effective temperatures, like the L3-cavity laser of Fig. 6.1 that exhibited a reduced self-heating with a slope of 43 K/mA.

As the ambient temperature increases, the Auger non-radiative recombination and the carrier leakage becomes more prominent,[193],[194] while the gain drop.[156] Therefore, the laser threshold current is also increased, which is of major importance since it determines the operating point of the laser for a given application. The threshold current dependence on the temperature is commonly described using the empirical relation:[195]

$$I_{th}(T) = I_0 \cdot exp\left(\frac{T}{T_0}\right) \tag{6.1}$$

where I_0 and T_0 are fitting parameters for a characteristic threshold current and a characteristic temperature, respectively. T_0 quantifies the sensitivity of the threshold to the temperature. Fig. 6.2(d) depicts the laser threshold evolution as a function of temperature in a semi-logarithmic scale. Equation 6.1 shows a good fit with the experimental data, and a characteristic temperature of 35 °C was extracted for both 1-QW and 3-QWs lasers. Such value is at the low end of InGaAsP-based laser

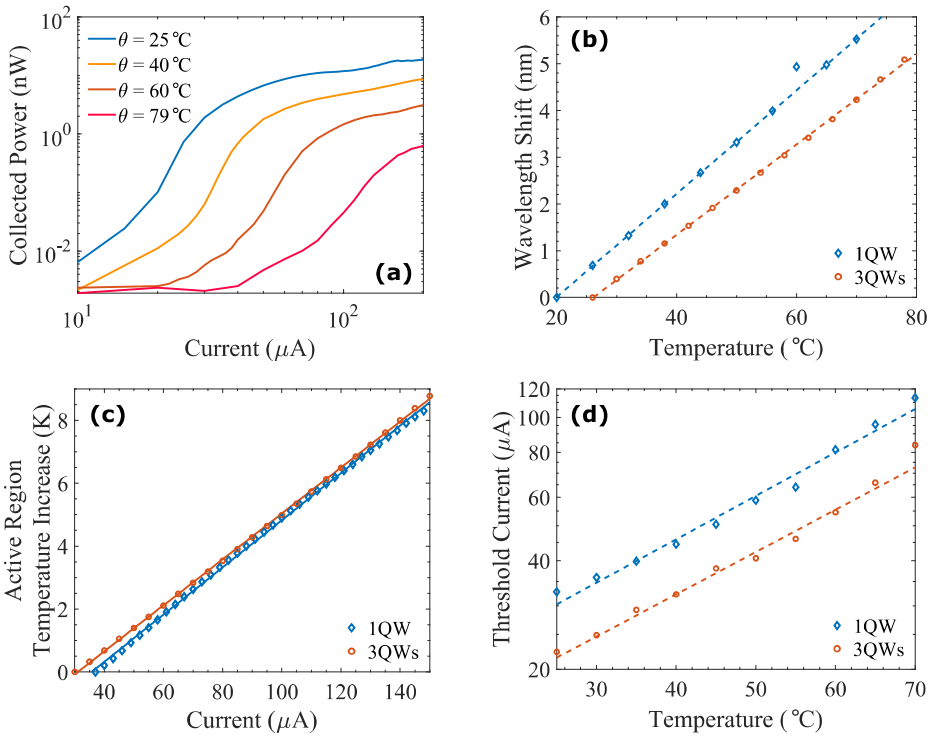

Figure 6.2 | Thermal behavior of PhC lasers. (a) Measured L-I curve of an 3-QW L7 laser for various heat sink temperatures. (b) Laser wavelength shift with respect to temperature. (c) Estimated active region temperature as a function of the injected current. (d) Threshold current dependence on heat sink temperature.

diodes,[156],[196] and is ascribed to the low heat conductivity of the air-suspended PhC membrane and the high carrier density operation. The heat dissipation can be improved by embedding the PhC membrane in a low-index material, like polymer or glass.[44],[197]

6.3 Injection Efficiency and Leakage Current

Compared to conventional long-wavelength and nanobeam lasers with vertical doping,[44] laterally-doped 2D PhC lasers exhibit a relatively low injection efficiency, η_i, estimated at around 1-10%,[45],[82] which can be related to high leakage current due to the lateral doping geometry. This hypothesis is confirmed in this section, which consists of three independent investigations.

6.3.1 Comparison Between Optical and Electrical Pumping

Firstly, we compare the laser performance under optical and electrical pumping of the same laser. Fig. 6.3(a) depicts the L-I-V and the L-L input-output curves of an L5 laser. A 1310 nm laser was used to pump the DUT using the same collection objective (the experimental setup described in section 3.2). By normalizing the L-I and L-L curves in terms of the laser threshold, we observe a saturation effect after the threshold for the electrical pumping. This effect is attributed to a reduction of η_i with current. In addition, the resonant wavelength evolution is illustrated in Fig. 6.3(b). The matching blueshift below the threshold indicates a similar carrier filling rate; however, the redshift rates diverge above the threshold, attesting to a corresponding mismatch in η_i. The increased redshift rates during opt. pumping is due to increased heating induced by the high-intensity field circulating the cavity, while ohmic heating is negligible.

The laser rate equations were fitted on the experimental input-output curves for both pumping schemes as shown in Fig. 6.3(c). For the fits, the same laser parameters were used. Namely, the confinement factor was calculated as 4%, and the effective index as 3.5. The transparency carrier density was chosen as $8.7 \cdot 10^{17}$ cm^{-3} while the rest of the material parameters are given in table 4.1. Following the findings of section 5.3, the Q-factor is chosen as 8000 and was used to calculate the photon lifetime as $\tau_p = Q\lambda/2\pi c$ where λ is the laser wavelength, and Q is the total Q-factor of the laser cavity.

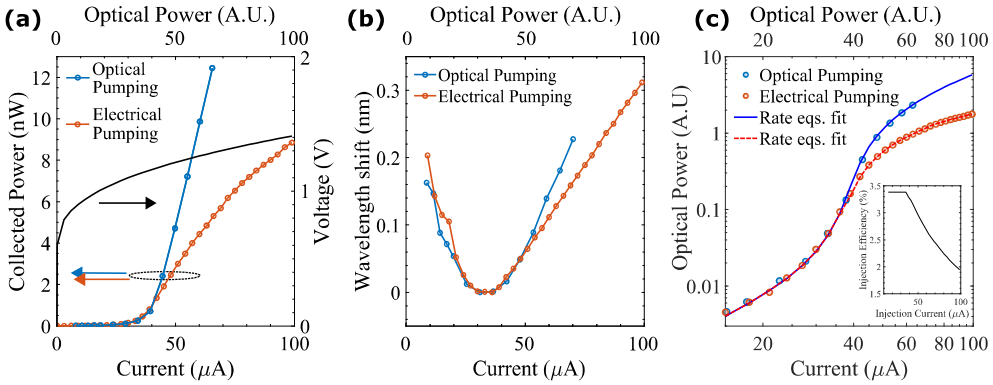

Figure 6.3 | Comparison between electrical and optical pumping. (a) LIV and LL curves of an L5 laser. (b) Spectral evolution of the laser peak. (c) LI and LL curve in a logarithmic scale. A fitting of the conventional and the modified rate equations for the optical and electrical pumping, respectively, is superimposed. The inset illustrates the evolution of the injection efficiency for electrical pumping.

A good agreement between the conventional rate equations fitting and the L-L characteristic, where the β-factor was calculated as 3% and is on par with previous studies using the same rate equations model.[82],[157] In contrast, the rate equations

could not accurately describe the behavior after the threshold in any parameter combination, which is associated with a voltage-dependent reduction of the injection efficiency. Thus, the rate equations were modified by introducing a current-dependent η_i shown in the inset of Figure 6.3(c). The injection efficiency is extracted as 3% and is reduced to a third of its original value. This injection efficiency drop has been observed consistently, especially close to the turn-on voltages of the QW barrier and the InP layer, which are 1.1 V and 1.3 V, respectively.

The injection efficiency is lower than this of previously demonstrated laterally doped 2D PhC lasers by Matsuo *et al.* [82],and significantly lower than the 1D nanobeam laser demonstrated by Crosnier *et al.* [44]. The later example has a different carrier injection geometry and does not feature a BH active region. As a result, a higher material quality is expected since no regrowth steps are performed, nor ion damage during doping, leading to a high internal quantum efficiency (IQE). By not utilizing a BH structure, the active material size is large, defined by the nanobeam waveguide, leading to a high threshold current. On the other hand, the injection efficiency of laterally doped lasers is reported to be around 10%, which is higher of what we report here. This is due to the non-optimal device quality of this particular L5 laser, including the BH quality and the randomness in the doping-induced losses. Comparatively, the BH lasers reported on Sec. 7.3,[1] exhibit high injection efficiencies above 10 %, with the best device reaching up to 35%.[2] As a result, the lower material quality of this device is absorbed by the injection efficiency fitting parameter.

6.3.2 Leakage Current and InP Emission

To further investigate the effect of the low injection efficiency, the optical spectrum of the laser at various pumping levels is shown in Fig. 6.4(a). The spectra reveal significant spontaneous emission in the higher-order modes, even at low pumping. Above threshold, the spontaneous emission is mostly clamped; however, as the injection current and the applied voltage increase, a peak at 950 nm is observed ascribed to InP emission.[3] The emission pattern of the InP electroluminescence (EL) was also identified via regular confocal microscopy imaging. Fig. 6.4(b) shows a microscope image of a working laser taken via an IR camera featuring an InGaAs detector. The same laser is imaged using a Si detector camera, as shown in Fig. 6.4(c). Due to the large bandgap of Si, the QW emission is not absorbed, and only the emission of the InP is detected.

Fig. 6.4(d) depicts a spatial mapping of the InP emission. The EL of InP closely resembles the p-doping profile indicating significant recombination close to the p-i interface due to the low mobility of the holes. A sketch of this mechanism is illustrated

[1] These lasers are fabricated on a different, less defective region of the same 2" wafer.

[2] All the above rate equation fits assume the same material parameters, including this of [82].

[3] We should also note that the InP emission strength is heavily underestimated since the collection of the vertically-scattered light is optimized for the light of the fundamental mode. In addition, there is no cavity effect for the InP emission, and we expect most light to be emitted in-plane.

in Fig. 6.4(e), where the flow of electrons and holes are depicted in blue and orange, respectively, and are radiatively recombined either in the BH or close to the p-i interface. This effect is more pronounced for larger p-offsets, where the unwanted recombination region does not overlap with the optical cavity, and lasing is impossible. However, such an effect has yet to be reproduced by drift-diffusion simulations using commercial software tools.[114],[198]

The spectra of Fig. 6.4(a) also reveal the modal structure of the L5 cavity that agrees well with the 3D-FDTD simulated spectrum shown at the upper part of the plot. A Lorentzian lineshape is fitted for each peak as shown in Fig. 6.4(e). The resonant wavelength and the cold cavity Q-factor are extracted from the fits, and their theoretical and experimental values are given in table 6.1. Although the resonant wavelength shows a very close agreement with the theory, the Q-factor is slightly underestimated mainly because of the convolution of the instrument response of the OSA.

Table 6.1 | Experimental and simulated mode structure of an L5 laser. The resonant wavelengths and Q-factor of the first seven modes of an L5 laser.

Mode Order	$\mathbf{6^{th}}$	$\mathbf{5^{th}}$	$\mathbf{4^{th}}$	$\mathbf{3^{rd}}$	$\mathbf{2^{nd}}$	$\mathbf{1^{st}}$	$\mathbf{0^{th}}$
$\lambda_{\mathbf{exp}}/nm$	1340	1411	1424	1435	1441	1504	1544
$\lambda_{\mathbf{sim}}/nm$	1336	1406	1421	1435	1440	1502	1544
$\mathbf{Q_{exp}}$	326	176	338	191	917	1545	-
$\mathbf{Q_{sim}}$	558	229	539	226	1054	1914	7664

6.3.3 Threshold Reduction by Electrical Isolation

The LEAP lasers developed by NTT,[40],[45],[82] are completely isolated from neighboring devices by selectively removing the InP layer around the PhC membrane and the contacts. This might provide better electrical isolation compared to our lasers, for which each contact is shared between four devices. The DTU mask was designed assuming that the leakage current will be negligible for biases lower than the turn-on voltage of InP, which is expected to be around 1.31 V. Furthermore, using an equivalent circuit, we can also see that the immediate neighboring devices form a loop connected in parallel but with one diode placed reverse polarity.

This hypothesis was tested when a need to decrease the threshold of the L3 laser presented in Sec. 6.1 arose. When first characterized, the L3 laser exhibited a threshold of 13.2 µA. A decision was made to further electrically isolate the laser; this was done by mechanically severing the PhC membrane of the neighboring devices using the electrical probes. A microscope picture of the destroyed devices is shown in Fig. 6.5(a). During the destruction of the PhC membranes, debris landed on top of the L3 cavity, diminishing the vertical quality factor. Although the coupling efficiency

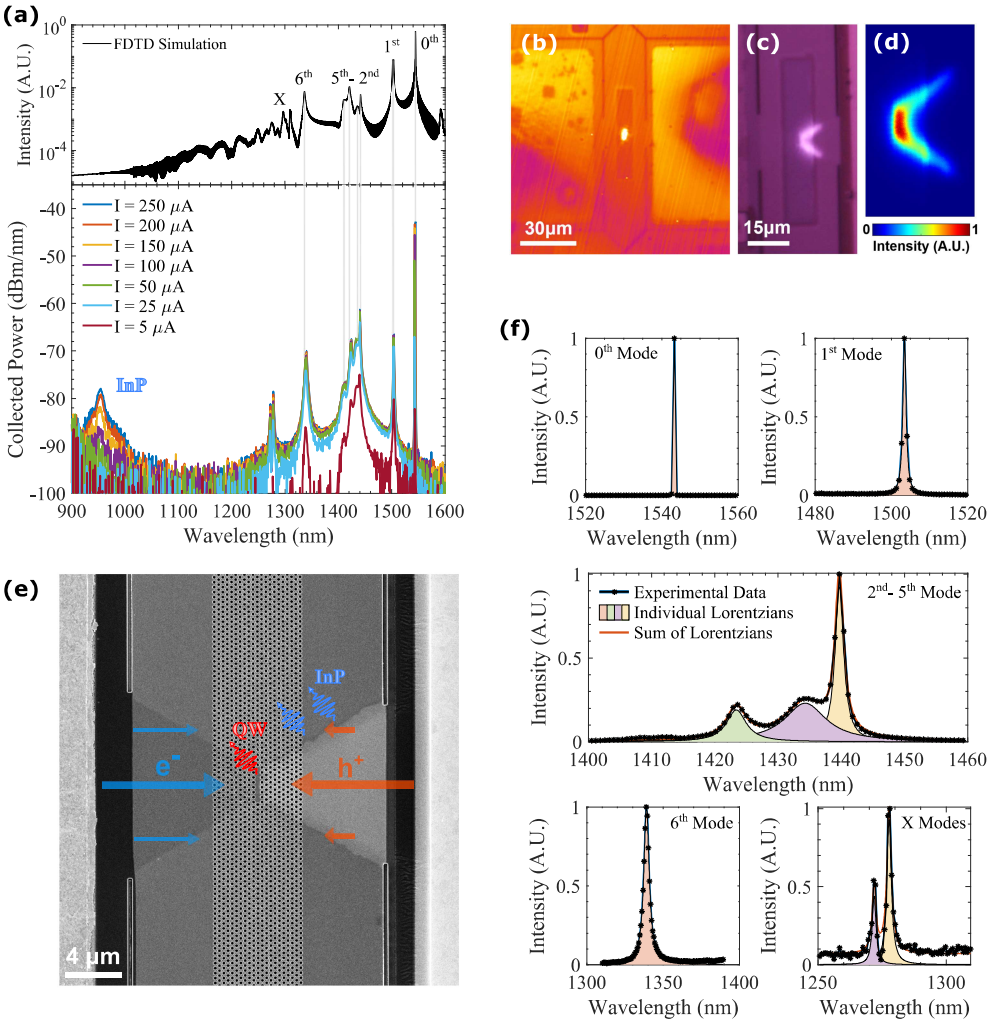

Figure 6.4 | Emission spectrum and leakage current. (a) Spectrum of an L5 laser under various pumping levels and its simulated spectrum. (b) Microscope image of a working laser captured by an InGaAsP camera. (c) Microscope image of a working laser captured by a Si camera. (d) Heatmap of the InP emission outlining the p-doping profile. (e) Colored SEM image illustrating the flow of electrons and holes and their radiative recombination at the BH and the p-i interface. (f) The emission spectrum of each PhC mode with superimposed Lorentzian fittings.

to the collection objective increased by an order of magnitude, no lasing could be observed. The chip was taken back to the cleanroom. After a series of soft wafer

cleaning[4] in conjunction with mechanical steering, the debris was removed from the cavity, and the Q-factor was restored.

After cleaning, lasing was achieved again with a reduced threshold of 10.2 µA. The LI characteristics before and after the electrical isolation and the final cleaning can be seen in Fig. 6.5(b). The threshold reduction corresponds to a substantial increase in the injection efficiency of 30 %, which is increased from 5% to 6.5%. Looking at the IV characteristics after the electrical isolation, we observe a minimal increase in the resistance; however, the threshold voltage remains at around 1.08 V with a disparity of 10 mV. This result proves that significant leakage is expected even at biases below the turn-on voltage of InP. It might also explain the significant injection efficiency increase for smaller active regions discussed in Sec. 7.3.

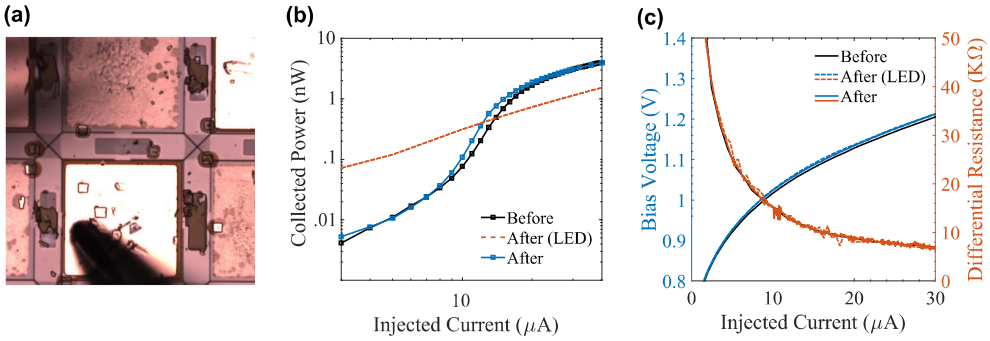

Figure 6.5 | Threshold reduction by electrical isolation. (a) Increased electrical isolation by physically breaking the PhC membrane of the neighboring devices using the electrical probes. Debris landed on the PhC cavity. (b) LI characteristics before, after the electrical isolation, and after the device's cleaning. (c) IV characteristics and differential resistance.

Electrical simulations using drift-diffusion and equivalent circuit models have yet to replicate the leakage in the structure, along with the effect of minimal injection efficiency for large p-doping offsets (see Secs. 2.3).

6.4 Summary

In this chapter, we investigated some of the static characteristics of 2D PhC lasers. In particular, the general static optoelectronic behavior of the lasers was established. Then, the thermal characteristics of the lasers were studied, showing that although the lasers are based on suspended membranes, there is minimal self-heating under operation. This heating depends on the intensity of the optical power circulating the cavity, while ohmic heating is negligible. Furthermore, we showed that the laser

[4]The cleaning was done by submerging the chip consecutively in Acetone-Ethanol-IPA-DI water.

performance significantly deteriorated at increased ambient temperatures, placing these lasers at the lower end of long-wavelength lasers in terms of thermal sensitivity. Finally, a comparison between optical and electrical pumping of the same device revealed that the injection efficiency drops as the voltage and applied current increase. This effect was caused by an increased leakage current manifested in the form of InP emission from the p-i interface. High leakage current is expected even at low applied biases and was verified by better isolating a device leading to a 30 % increase in the injection efficiency.

CHAPTER 7

Lasers with Varying Buried Heterostructure Length

In this chapter, we study the laser characteristics for different active material sizes by systematically varying the buried-heterostructure length. In particular, the confinement factor, the doping losses, the laser wavelength, the threshold, and the dynamic properties are studied.

Another important objective of this investigation is the further reduction of the laser threshold. A literature study for all reported laterally-doped PhC lasers failed to uncover any correlation between threshold current and active region size. Most notably, in the work of Takeda et al. [42] different few-cell LD cavities were studied where the active material matches the cavity length; however, no trend in the laser threshold was apparent. This was also found in our fabricated lasers where the L2 and L1 lasers exhibited much higher thresholds than their longer counterparts.[1] This result can be explained by the randomness in the diffusion of the p-dopants; more specifically, if the cavity length matches the doping width, there will be higher losses in smaller cavities, imposing a lower limit in the miniaturization process. To understand this effect, a dedicated experiment was conducted where the BH and doping length were varied in a fixed L7 optical cavity.

7.1 FDTD Simulations

Firstly, 3D-FDTD simulations were conducted to estimate the confinement factor for the different modes and the modal gain and modal losses of the fundamental mode. In the simulations, an L7 cavity was considered, while the BH and matching doping length are varied given in units of the PhC lattice constant. The BH width remains constant at 400 nm. The refractive index of the InP and BH is 3.17 and 3.26, respectively, while the absorption coefficient of the p-InP region is 120 cm^{-1}.

[1] For all the above demonstrations the doping profile width matches the BH length, similar to the schematic diagram of Fig. 2.1(a).

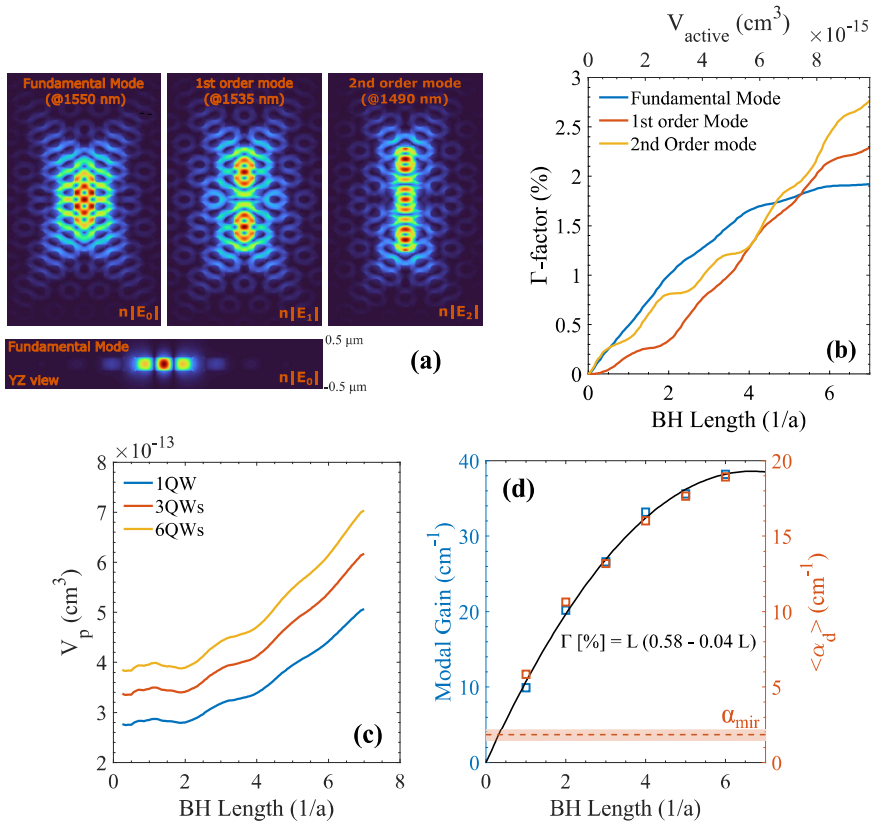

Figure 7.1 | Simulations of L7 cavity with varying BH length. (a) Scaled electric field profiles of the fundamental, first, and second order modes. Bottom: Cross-sectional plot of the fundamental mode. (b) The confinement factors of the different modes for varying BH length. (c) Photon volume of the fundamental mode versus the BH length for different quantum well numbers. (d) Modal gain (Γg_0) and doping losses versus the BH length.

The field profiles of the fundamental and the first- and second-order modes are shown in Fig. 7.1(b), where the field profile is weighted with the refractive index as $n(\vec{r})|E(\vec{r})|$, which is the quantity that is used in mode overlap calculations (see eq. 4.5). Furthermore, the resonant wavelength of each mode is also given; the mode spacing is practically constant under resonance tuning, e.g., by shifting the PhC hole radius. Fig. 7.1(c) illustrates the confinement factor for the different modes. The evolution of the confinement factors exhibits bumps that follow the anti-nodes of the field. Comparing the magnitude of the confinement factors, we observe that the fundamental and second-order modes have an anti-node at the center, while the first-order mode has a node at the center. The fundamental mode is more spread outside the line defect, and thus the confinement factor is lower at longer BH lengths. Furthermore, we should note that the BH width is finite at 400 nm, occupying most

of the high-index region of the line defect. As a result, the confinement factor of the higher-order modes shows bumps corresponding to the anti-nodes of the field. In contrast, the confinement factor of the fundamental mode is increasing smoothly as all anti-nodes of the field are integrated.[2] Finally, an increase in the β-factor and the side-mode suppression ratio (SMSR) is expected for smaller BH lengths due to the difference in the modal confinement factors.

Reducing the active region volume is crucial to achieving ultra-low threshold currents. However, this will also reduce the confinement factor and, thus, the modal gain. A figure of merit analogous to the mode volume for lasers is the photon volume defined as $V_p \equiv V/\Gamma$.[174] Minimizing the photon volume is crucial for high-efficiency, low-power consumption applications, since the modulation efficiency of a laser is inversely proportional to the square root of V_p (see eq. 4.11). The photon volume of the fundamental mode as a function of the BH length is plotted in Fig. 7.1(c), where active regions with different numbers of QWs are considered. The BH length decrease leads to a similar reduction of V_p, reaching a flat bottom at shorter BH lengths. Finally, the difference in V_p for multiple QWs tests the validity of the conventional assumption of constant field intensity in the z-direction expressed as $\Gamma = n_{QWs}\Gamma_{1QW}$, where n_{QWs} and Γ_{1QW} is the number of QWs and the confinement factor per well, respectively. In reality, the transverse electric field inside the membrane resembles a gaussian distribution, and an explicit calculation of the confinement is needed.[3]

For the fundamental mode, the modal gain and modal loss due to doping are plotted against the BH length in Fig. 7.1(d). The doping length is taken equal to that of the BH. The modal gain, Γg_0, is calculated using the simulated confinement factor scaled with the gain coefficient g_0 whose value is chosen as 2000 cm^{-1}. The modal loss is calculated from the Q-factor using eq. 5.2. The modal gain and modal losses can be approximated using the same quadratic function but with different scaling factors. For completeness, the mirror-losses are plotted against the BH length and calculated using eq. 5.2 and the Q-factor of an undoped L7 cavity. The increase of the Q-factor due to the high refractive index of the BH is considered negligible.

7.2 Effective Index of the Buried-Heterostructure

In Sec. 5.1, the effect of the PhC hole radius and the refractive index on the resonant wavelength was discussed. However, an additional redshift of the resonance was observed for the fabricated lasers compared to the passive PhC cavities. This redshift is caused by the high refractive index of the epitaxial layers of the BH, which has been previously neglected. In addition, this effective refractive index change will significantly impact the dispersion of the LD waveguides, drastically changing the

[2] For the fundamental mode, the anti-nodes of the field along $y = 0$ stem from the symmetric (across $x = 0$ parity plane) E_y profile, while the anti-nodes at $y \neq 0$ stems from the anti-symmetric (across $y = 0$ parity plane) E_x profile. A direct analogy can be found in L3-type cavities [68].

[3] In this calculation, the InP membrane is 250 nm thick, and the QWs are based on an 8 nm thick QW sandwiched between 10 nm thick barriers.

oscillation condition for the Fano Lasers. As a result, it is crucial to quantify the effective refractive index of the BH. To reduce the computation requirements, we model the sub-wavelength features of the BH epi-structure using the effective medium theory where the effective permittivity is given by:[199]

$$\varepsilon_{eff} = \sum_i f_i \varepsilon_i \tag{7.1}$$

where f_i and ε_i is the relative thickness and the permittivity of the i^{th} layer. For the BH slab, $f_i = t_i/t_{tot}$ where t_i is the thickness of the i^{th} layer and t_{tot} is the total slab thickness. The refractive index is given by $n_i = \sqrt{\varepsilon_i}$ and was expected to be 3.17, 3.26, and 3.6 for InP, the QW barrier, and the QW, respectively. Using eq. 7.1 the effective index of a single-QW n_{BH} is estimated as 3.2. However, this approach failed to replicate experimental results, and of series of measurements in conjunction with FDTD simulations was performed to quantify the effective index of the BH experimentally.

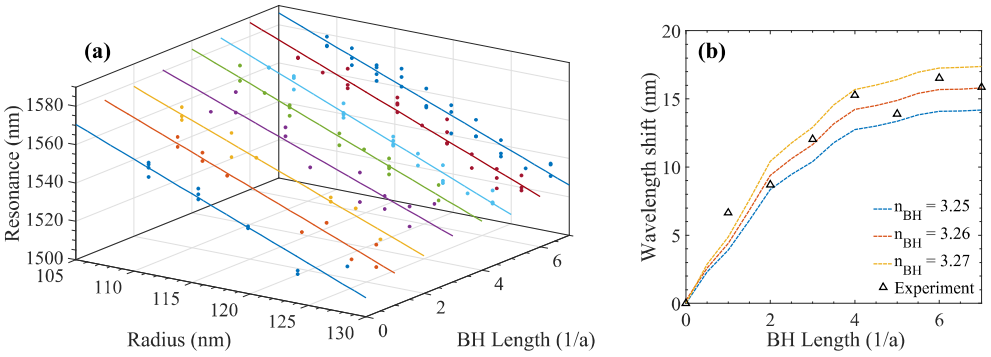

Figure 7.2 | BH effective refractive index. (a) Resonance as a function of PhC hole radius for L7 cavities of different BH lengths. (b) Resonance shift for different BH lengths.

Firstly, the resonant wavelength of the fundamental mode of reference L7 cavities with varying radii was determined via cross-polarization scattering spectroscopy (see Sec. 3.4). Secondly, the resonance was extracted from the emission of an ensemble of L7-based devices featuring different BH lengths and PhC radii as illustrated in Fig. 7.2(a). Since the statistical variation of the PhC resonance due to the disorder of the PhC holes ($\sim$ 5 nm) is much larger than the variation of the resonance due to carrier filling effects ($<$ 0.5 nm), both lasing and non-lasing light emitting devices were considered. The mean relative resonance shift for the BH cavities compared to the passive L7 cavities is shown in Fig. 7.2(b). The comparison between the experimental results with 3D-FDTD simulations shows that the effective index of the BH is 3.26.

The reference L7 cavities were also used to assess the quality of the fabrication process of the chip. The intrinsic Q-factor of the fundamental mode of the L7 cavity

was found to be very close to the simulations (Q = 75k ± 10k), verifying that the fabrication imperfections do not affect the properties of the L7 cavities.

7.3 Threshold Characteristics and sub-μA Lasing

Following the FDTD simulations, 1-QW lasers comprised of an L7 cavity with various BH lengths are fabricated. In particular, the active material size is chosen as L_{BH}x400x8 nm^3, where L_{BH} is the length of the BH. For simplicity, the length of the BH is expressed in terms of the PhC lattice constant (a_{PhC} = 440 nm). The lasers were tested at room temperature and CW pumping and are identified by their respective BH length size, e.g., a BH5 laser corresponds to an L7 cavity laser featuring a 5x440 nm long BH region.

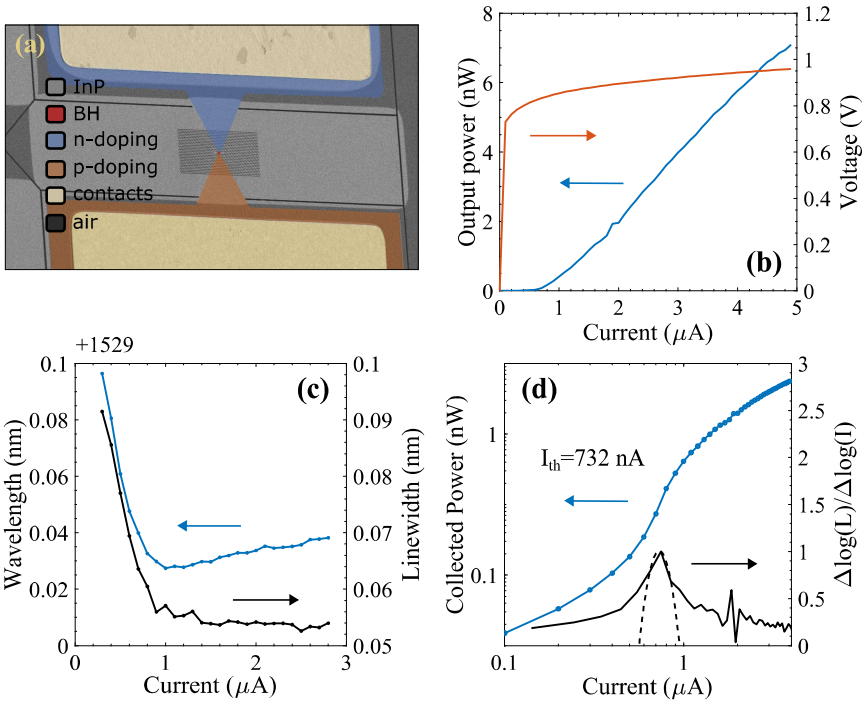

Figure 7.3 | Static characteristics of BH1-L7 laser. (a) Bird's-eye view colored SEM image of the device. (b) LIV characteristic of the BH1 laser. (c) Peak wavelength and linewidth as a function of injection current. (d) LI curve in logarithmic scale and its first-order derivative.

Fig. 7.3(a) illustrates an artificially-colored SEM image of a BH1 laser. The characteristic LIV curve of the laser is shown in Fig. 7.3(b), exhibiting a sub-μA threshold current and a sub-V threshold voltage. Fig. 7.3(c) depicts the peak wavelength and

linewidth as a function of the injected current. Both quantities exhibit the typical laser behavior, e.g., linewidth reduction and carrier clamping at threshold. In Fig. 7.3(d), the LI curve is plotted in a logarithmic scale. Due to the high β-factor, the maximum of the first order derivative, $\mathrm{dlog}(L)/\mathrm{dlog}(I)$, was used to extract the laser threshold, as described in Sec. 3.1.2. The accuracy of the laser threshold estimation is bound by the spacing of the injection current sweep (100 nA); the accuracy is increased by fitting a second-order Taylor expansion around the maximum, and the threshold current was calculated as 732 nA. To the best of our knowledge, this is the lowest threshold current for semiconductor lasers in CW-RT operation to date.

Furthermore, the effect of the active material size on the laser performance is investigated. Fig. 7.4(a) shows the LI curves of lasers with different BH lengths, pumped up to 5 times the threshold. Apart from the BH2 and BH4, most BH lasers exhibit similarly good performance. In particular, the threshold increases monotonically with the BH length. Also, the differential efficiency drops as the doping losses increase following $\eta_d \propto \eta_i \alpha_{mir}/(\alpha_{mir} + \alpha_d)$,[156] which is another advantage of the reduced doping losses of the BH1 laser.

The thresholds of the BH lasers were extracted numerically and are plotted in a semi-logarithmic scale against the BH length in Fig. 7.4(b) with theoretical fits of eq. 6.1. Merging all the constants of eq. 6.1 into one characteristic linear current density term, J_0, the threshold current can be written in a simplified form as:

$$I_{th} = \frac{J_0 L_{BH}}{\eta_i} \exp\left(\frac{a_{mir} + a_{dop}}{\Gamma g_0}\right) = \frac{A_d J_0 L_{BH}}{\eta_i} \exp\left(\frac{a_{mir}}{\Gamma g_0}\right) \tag{7.2}$$

where L_{BH} is the BH length, η_i is the injection efficiency a_{mir} represent the mirror-losses and a_{dop} represent the doping-induced absorption losses. Since the absorption losses exactly scale with the modal gain (see Fig. 7.1(d)), $\exp\left(a_{dop}/\Gamma g_0\right) = A_d$, where A_d is a constant, scaling the characteristic current density J_0.

According to eq. 7.2, the threshold current should increase linearly when $a_{mir} \ll \Gamma g_0$. On the other hand, a characteristic length will exist where the threshold is minimized, below which the mirror-losses dominate, and the threshold increase exponentially. Such a characteristic length has not been observed in our experiments, indicating that further BH miniaturization is possible. Two solutions of eq. 7.2 have been superimposed on Fig. 7.4(b), where the mirror-losses, doping induced losses and modal gain are taken from Fig. 7.1(d), while the characteristic current density is 150 nA/a_{PhC}. The injection efficiency is 35% and 9% for the blue and orange lines, respectively. The observed trend in threshold cannot be replicated with the assumption of constant injection efficiency. Contrary to conventional wisdom, the injection efficiency seems to increase for smaller BH lengths, although a reduction of η_i would be expected due to an increased current density requirement and a larger leakage current.

The injection efficiency and the β-factor for the BH lasers were calculated using the conventional rate equations. The modal losses were chosen based on the 3D-FDTD simulations of Sec. 7.1. The material parameters are given in table 4.1. Fig.

7.4(c) shows the injection efficiency for the different BH lasers, which also confirms a reduction of η_i for longer BH lasers. Furthermore, the BH2 and BH4 lasers are also outliers in terms of the injection efficiency, and should be undervalued compared to a better-quality device. The trend of the injection efficiency is not well understood yet, but the main hypothesis is that it is dependent on the threshold voltage. In particular, Sec. 6.3 discussed the experimental observation of an increased leakage current well below the turn-on voltage of InP, that also scales with the applied voltage and the injected current. Since the IV characteristics of a laser are typically decoupled to the LI curve, the value of the threshold current is positively correlated with the applied voltage at the threshold.

The β-factor exhibit a two-fold decrease for longer BHs, starting from 2% for the BH1 and dropping to 1% for BH7. This β-factor reduction is attributed to the relative confinement factor suppression for the higher-order modes, which also led to an increased SMSR for the BH1 laser. The latter effect is illustrated in Fig. 7.4(d), where the spectra of the BH1 and BH7 lasers are shown. In particular, the BH1 laser exhibit a 5 dB increase in the SMSR for the first- and second-order modes compared

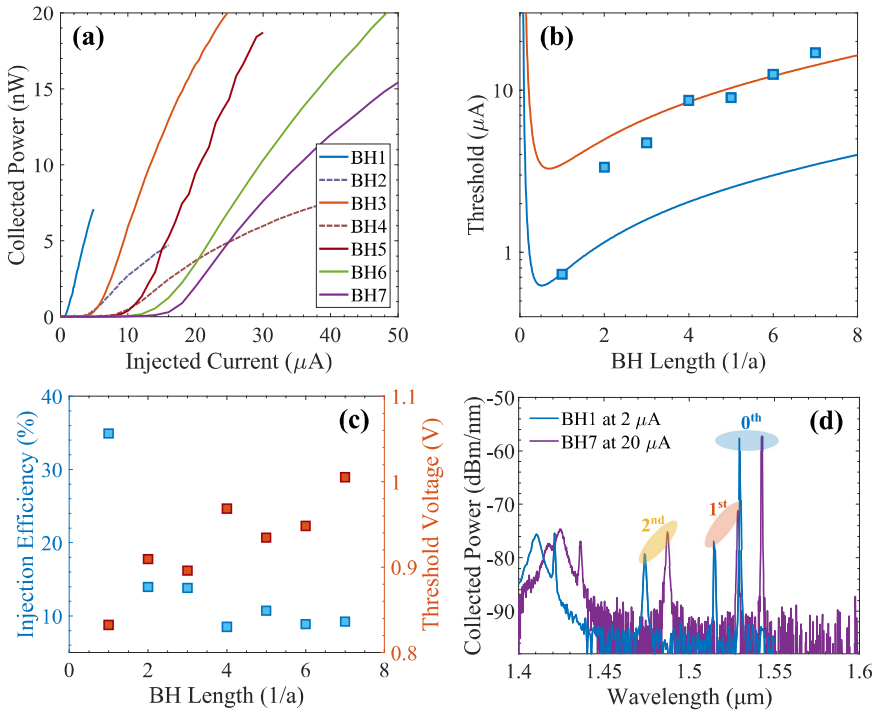

Figure 7.4 | L7 lasers with different active material sizes. (a) LI curves for different BH lengths. (b) Threshold current versus BH length and analytical solutions. (c) Calculated injection efficiency and applied voltage at the threshold. (d) Spectra of BH1 and BH7 lasers.

to its BH7 counterpart.

7.4 Dynamic Characteristics

One of the main applications of in-plane PhC lasers is on-chip and chip-to-chip communication, which would be realized via direct modulation. Thus, it is vital to understand the dynamic properties of these lasers. In this section, the dynamic characteristics of the BH lasers are studied via small-signal modulation analysis. For these experiments, a low-power AC component is applied - in addition to a DC component - to the laser, and the frequency response of the laser is recorded. The DC signal is applied using a bias-tee, while the AC signal is generated via a vector network analyzer that is also used to measure the frequency response of the laser. Details on the experimental apparatus are given in Sec. 3.3.

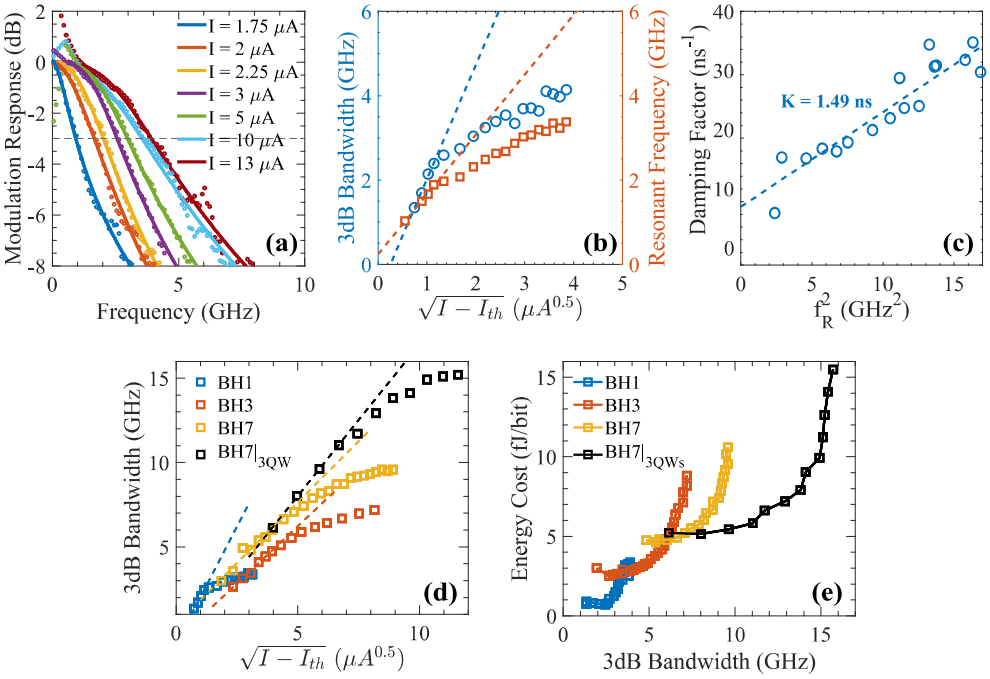

Figure 7.5 | Small-signal analysis of BH lasers. (a) The modulation response of the BH1 laser for different pumping levels. (b) The 3-dB bandwidth and the resonant frequency are plotted against the square root of the injected current above the threshold. (c) The damping factor versus the squared resonant oscillation frequency. (d) The 3-dB bandwidth evolution for different BH lasers. (e) The energy cost per bit as a function of the 3-dB bandwidth for different BH lasers.

Fig. 7.5(a) shows the modulation response of the BH1 laser for different pumping

levels. The modulation response exhibits the characteristic bandwidth increase for higher pumping levels—the response function of eq. 4.10 was fitted to the experimental data and is superimposed using solid lines. The fitted frequency response was used to extract the resonance frequency, the damping factor, and the scaling parameter A to renormalize the data and extract the 3-dB modulation bandwidth. Due to the significant damping, the parasitic frequency pole can play an important role in the fit, and thus it was considered constant, assuming an RC constant of 5 ps.[82]

The 3-dB modulation bandwidth, f_{3dB}, and the resonant frequency, f_r, for the BH1 laser are plotted against the square root of the injected current minus the threshold current in Fig. 7.5(b). The slope of f_{3dB} and f_r represent the modulation efficiency and the D-factor, respectively; both are used to quantify the efficiency of the modulation bandwidth increase as a function of the output power. The definition of the D-factor is given in eq. 4.11. Furthermore, the K-factor of the laser is extracted from the slope of the damping factor and the square of the resonance frequency as shown in Fig. 7.5(c). From these fits, the D- and K-factor are calculated as 44.8 GHz $\text{mA}^{-1/2}$ and 1.5 ns, respectively, while the modulation efficiency is 68.6 GHz $\text{mA}^{-1/2}$. The modulation efficiency of the laser is multiple times higher than observed for high-speed VCSELs,[200],[201] further attesting to the potential of PhC lasers for low power-consumption computer-com applications. Yet, the efficiency drops for modulation speeds above 3 GHz due to damping. Although high damping can be beneficial to the signal quality in data transmission,[202] it also limits the maximum intrinsic modulation bandwidth of the laser, which can be expressed as $f_{3dB}^{max} = 2\pi\sqrt{2}/K$. For the BH1 laser, the maximum intrinsic bandwidth is capped at 6 GHz.

Table 7.1 | Small-signal modulation characteristics of L7 lasers.

L7 cavity laser	Modulation Efficiency (GHz $\text{mA}^{-1/2}$)	D-factor (GHz $\text{mA}^{-1/2}$)	K-factor (ns)
BH1	68.6	44.8	1.49
BH3	48.8	43.4	0.72
BH7	41.5	34.4	0.18
$\text{BH7}|_{3QW}$	60.2	35.5	0.16

Similar small-signal analyses were conducted for the BH3, BH7, and a 3QW-based BH7 laser previously presented in [203]. The 3-dB bandwidth versus the square root of the bias current above the threshold for the different BH lasers is illustrated in Fig. 7.5(d). The modulation efficiency, the D-factor, and the K-factor for the different lasers are compared in Table 7.1. For the 1QW samples, the D-factor trend agrees well with eq. 4.11 since it scales with the injection efficiency and the inverse photon volume, further highlighting the advantage of the BH miniaturization. On the other hand, there is a smaller increase in the D-factor than expected from theory, indicating that the smaller lasers indeed operate at higher carrier densities and lower differential gain. The 3QW laser should be operated at a higher differential gain; however, the

D-factor is very similar to its 1QW counterpart, which suggests that it should feature a lower injection efficiency. In addition, the K-factor trends also agree with the theory as it increases for smaller BH lasers due to the longer photon lifetimes (see eq. 4.13). The 3QW laser exhibits the smallest K-factor due to the high-differential gain. A modulation bandwidth of 15 GHz was obtained, a value comparable to state-of-the-art long-wavelength VCSELs,.[201] The parasitics limit the modulation bandwidth since, according to the K-factor, an intrinsic bandwidth of 55 GHz is expected. The behavior of the 3QW-BH7 laser agrees well with previously demonstrated results.[40],[82] For completeness, the S_{21} traces are shown in Fig. D.2.

Although the modulation bandwidth is significant, the energy cost per emitted bit is also a crucial figure of merit of a transmitter that will essentially determine the employment of PhC nanolasers in real-life on-chip applications. The energy cost per bit is estimated as:[204]

$$EC = \frac{IV}{1.3 f_{3dB}} \tag{7.3}$$

where f_{3dB} is the 3-dB bandwidth of the small-signal response function. The energy cost per bit for the different BH lasers is plotted against the 3-dB bandwidth in Fig. 7.5(e), showing that the BH1 laser can operate at the standard processor clock rates of 2-3 GHz,[14] with an energy cost less than 1 fJ bit^{-1}. In practice, this corresponds to an average energy cost below 0.5 fJ bit^{-1} on the transmitter side since an equal number of '0' and '1' bits is used for non-return-to-zero modulation. Comparatively, longer BH lasers can achieve higher data rates but at an increased energy cost. However, it is energetically favorable to achieve a given data rate by multiplexing multiple shorter, lower-threshold lasers. For example, the energy cost for achieving a data rate of 6 GHz is 4 fJ bit^{-1} and 5 fJ bit^{-1} when using a BH3 and a BH7 laser, respectively, compared to the 2 fJ bit^{-1} needed when employing two BH1 lasers.

7.5 Summary

This section systematically investigated the laser performance to the active material size. L7 lasers with varying BH lengths were simulated, confirming that the doping losses scale with the modal gain for matching BH and doping lengths. The effective refractive index of a 1QW BH was determined by combining experiment and theory.

Furthermore, the LI characteristics of the BH lasers were compared, exhibiting a threshold current increase as a function of the BH length that does not agree with conventional semiconductor laser theory. Combined with rate equation fittings, we showed that the injection efficiency drops for longer BH regions which can be attributed to the increased leakage current due to higher applied bias, higher material quality, and a uniform doping profile plaguing longer devices. The BH1 device exhibited a threshold of 732 nA, which is the record for lasing at room temperature.

In contrast, the trend of the threshold curve suggests that further miniaturization is possible.

Finally, the dynamic properties of the BH lasers were characterized, exhibiting high modulation efficiency and high damping that limits the maximum modulation bandwidth. Nevertheless, we showed that a minimal energy cost of 1 fJ bit^{-1} at data rates of 3 GHz is possible.

CHAPTER 8

Photonic Crystal Fano Lasers

This chapter presents work aiming at demonstrating electrically-driven Fano lasers. The Fano laser offers unique modulation possibilities,[89],[90],[94] enhanced coherence,[93] and robustness to feedback[91] making it a favorable design for compact laser sources intended for on-chip applications. Although the realization of optically-pumped Fano lasers with,[93],[94] and without[92] the buried-heterostructure (BH) technology has been successful, electrically-pumped Fano lasers have yet to be demonstrated. In this investigation, we focus on the 2D-PhC Fano laser designs based on an H0 nanocavity studying the properties of the Fano cavities and Fano lasers.

8.1 Design and Simulations of the Fano Cavity

The Fano laser cavity design studied in this project is illustrated in Fig. 8.1(a) and consists of a semi-open PhC line defect waveguide, a broadband mirror, and a narrowband Fano mirror. The termination of the waveguide acts as the broadband mirror created by the photonic bandgap effect. An H0 nanocavity (NC) is side-coupled to the waveguide, acting as a narrowband Fano mirror. The reflectivity of the Fano mirror stems from the interference between the discreet NC mode and the continuum of waveguide modes. Therefore, the Fano mirror reflectivity strongly depends on the resonant wavelength of the NC mode, ω_{nc}. Fig. 8.1(b) shows the amplitude of the Fano mirror reflectivity as a function of the frequency detuning normalized to the total decay rate of the field from the NC, γ_{tot}.[1] A line defect cavity is created between the broadband and the narrowband Fano mirror, as depicted in the sketch of Fig. 8.1(c). For an optimal effective cavity length, the resonant frequency matches the frequency of the NC mode, and maximum reflectivity is achieved.

[1] For this calculation, the nanocavity resonance was chosen as 1.55 µm, and the total cavity and intrinsic Q-factor were chosen as 1,000 and 100,000, respectively. The optical decay rate for the i loss channel is given by: $\gamma_i = \omega_{nc}/2Q_i$. Details on the Fano laser theory can be found in [95].

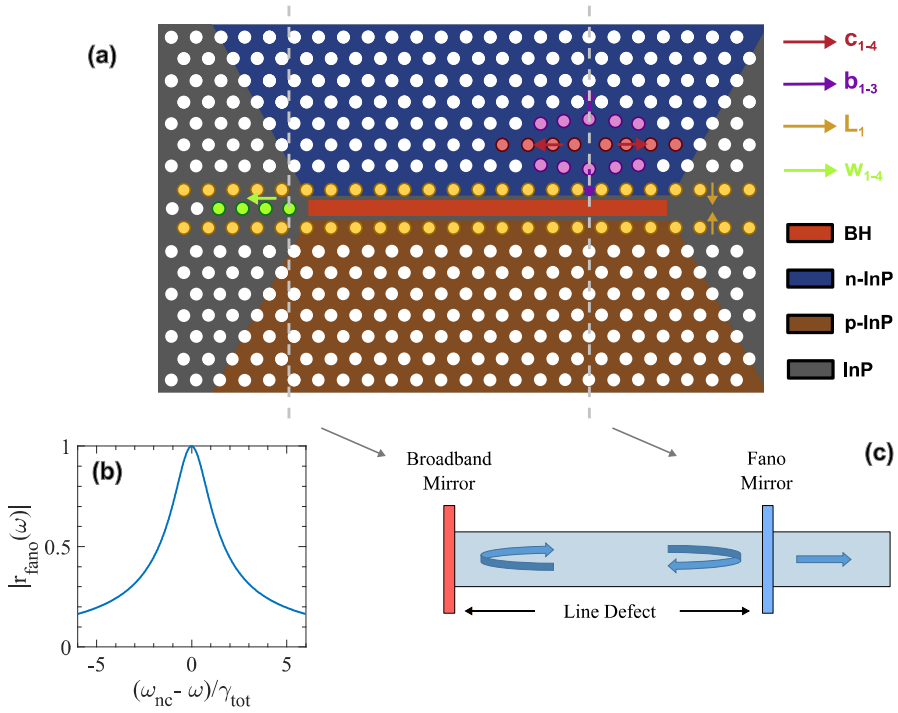

Figure 8.1 | Fano cavity design. (a) Schematic diagram of a Fano laser design based on an H0 nanocavity. The PhC holes whose position deviates from the lattice are colored and named depending on their functionality. Similarly, the intrinsic, doped, and BH active regions are color-coded. (b) The amplitude of the Fano mirror reflectivity as a function of the frequency detuning from the resonant frequency of the nanocavity. (c) A sketch illustrating the Fano cavity formation.

The process of designing a Fano cavity can be summarized in four steps. Firstly, a nanocavity with a high intrinsic Q-factor and appropriate resonant wavelength is designed.[2] The NC is strongly coupled to a broadband waveguide. Then, a conventional broadband mirror is added by terminating the waveguide. The distance between the conventional broadband mirror and the Fano mirror determines the length of the line defect part of the optical cavity. Finally, the reflectivity of the Fano mirror is optimized by a series of optimizations that aim to meet the oscillation condition. The series of optimizations include the position shift of the surrounding PhC hole rows to the waveguide (L_1 parameter), shifting the mirrorholes at the termination of the waveguide (w_1-w_4), and changing PhC hole radius r and lattice constant a. A schematic diagram of a Fano laser is illustrated in Fig. 8.1(a), where all the hole position shifts are color-coded based on their functionality. Furthermore, the InP slab is

[2]The resonant wavelength should match the emission wavelength of the active region for maximum efficiency.

color-coded for the different materials, e.g., the BH and the intrinsic and doped InP regions that constitute the final Fano laser design.

Firstly, a Fano cavity design based on a uniform InP slab is used as a study case to understand the effect of the different types of hole-position optimizations. The design was optimized by Yi Yu targeting optically-pumped InP membranes embedded with InAs quantum dots with a central emission wavelength of 1570 nm. Thus, the refractive index of the InP membrane can be considered uniform, chosen as 3.17. The detailed design parameters are given in Appendix E. The magnetic field profile, $|H|$, of the Fano mode is shown in Fig. 8.2(a), where we observe that the field is strongly localized in the nanocavity. For maximum Fano mirror reflectivity, the NC is strongly coupled to the waveguide, and the optical mode is localized not only in the NC, i.e., as in the under-coupled case, but also in the LD waveguide, where the BH active region will be selectively placed.

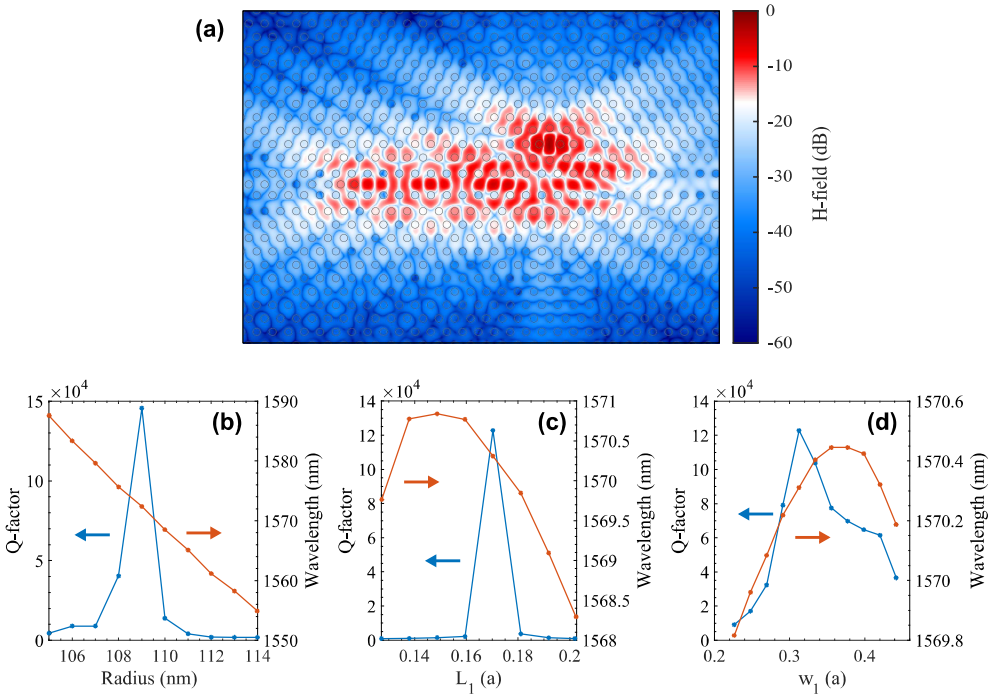

Figure 8.2 | FDTD simulations of the Fano cavity. (a) Magnetic field profile ($|H|$) of the Fano mode. The PhC holes are outlined in black. (b-d) The Q-factor and the resonant wavelength as a function of (b) the PhC hole radius, (c) the shift of the PhC holes row sub to the line-defect waveguide, and (d) the shift of the first mirror-hole terminating the waveguide.

Fig. 8.2(b) shows the Q-factor and the resonant wavelength of the Fano mode as a function of the PhC radius. The resonant wavelength of the Fano mode follows

the resonance of the NC. Thus it is linearly dependent on the hole radius. The Q-factor and the resonance of an isolated NC mode have already been discussed in Sec. 5.1. For this design, the intrinsic Q-factor of the nanocavity is higher than 400,000. However, the Q-factor of the Fano mode is lower and much more sensitive to radii shifts since the reflectivity of the Fano mirror strongly depends on the resonant frequency between the two right-propagating waves.

Secondly, in Fig. 8.2(c) the L_1 parameter is swept, which largely affects the Fano mode's Q-factor. In particular, changing L_1 will strongly affect the phase due to the change in the waveguide dispersion. Specifically, increasing L_1 will redshift the dispersion of the waveguide, and it is a method used extensively for dispersion engineering, i.e., to design slow-light waveguides without perturbing the hole radius.[205] Notably, L_1 also changes the coupling strength of the waveguide to the nanocavity, which is the major contributor to the change of the Q-factor of the Fano mode. During this parameter optimization, care should be taken to achieve a high Q-factor, while the NC is strongly coupled to the waveguide. For instance, a high Q-factor can be attained in the weak-coupled regime, but the field will be strongly localized in the NC and not in the LD waveguide. Additionally, we observe a slight change in the resonant wavelength, which is determined by the local perturbation of the H0 field and the satisfaction of the resonant condition.

Finally, Fig. 8.2(d) depicts the change in Q-factor and resonant wavelength as a function of the position shift of the 1st mirrorhole of the broadband mirror. The first mirrorhole position affects the vertical scattering of the light, as discussed in Sec. 5.2. Thus, gentle confinement is achieved by moving it away from the LD cavity. In contradiction to conventional LN cavities, the optimal shift is found at $0.31a$, instead of the typical $0.25a$, found during the Q-factor optimization of LN cavities, suggesting that the hole position is not only optimized for the scattering from the mirrorhole, but also for tuning the phase of the light reaching the Fano mirror. In particular, the w_1 parameter also affects the mirror phase and the penetration depth in the broadband mirror, thus the effective cavity length.[158] This can also be observed in the resonant wavelength of the Fano mode that varies around the H0 resonance and is expected to lead to different Fano mirror reflectivity.[95]

The Effect of the BH and Doping

After a few failed experimental attempts to realize an electrically-driven Fano laser, FDTD simulations were used to study the elements that might affect the Fano Laser cavity design. In particular, the effect of the BH and doping was studied.

In those failed attempts, a central assumption was that an optimal radius would exist regardless of the effective index of the BH. This assumption was tested by a series of simulations, where a BH was included in the semi-open waveguide. Fig. 8.3(a) shows the Q-factor versus the PhC design radius for different effective indexes of the BH. The plot shows that the optimal design radius is getting smaller to counterbalance

the redshift of the W1 dispersion due to the increased BH index;[3] however, the maximum Q-factor also decreases. The maximum Q-factor depends on the maximum Fano mirror reflectivity that is reduced due to the decrease in the coupling strength of the NC to the waveguide (see eq. 8.1). Interestingly, a broad region with sufficiently high reflectivity to support lasing exists for radii away from the optimal radius. Since the maximum Q-factor depends on the BH length, the Fano design was tailored for a BH with an effective index of 3.2 and a center wavelength of 1550 nm to match the fabricated 1-QW samples.[4] The design parameters of this Fano laser are given in Appendix E.

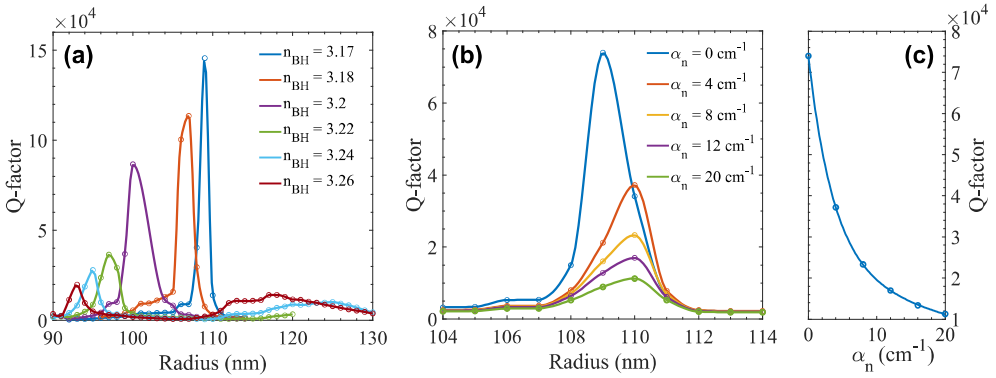

Figure 8.3 | Simulated Q-factor of Fano cavities including the BH and doping. (a) Q-factor of the Fano mode as a function of radius for various BH effective indexes. (b) Q-factor of the Fano mode as a function of the radius for different absorption coefficients of the n-doping. (c) Maximum Q-factor as a function of the absorption coefficient.

Finally, the effect of doping was studied. For the electrically-driven Fano laser design, we place the nanocavity at the n-doped side of the waveguide since a significantly lower free-carrier absorption of n-dopants is expected. Fig. 8.3(b) depicts the Q-factor of the Fano mode over the designed radius for different n-doping absorption coefficients. In this simulation, the n-doped region is modeled using a complex refractive index similar to Sec. 5.3.

The maximum reflectivity of the Fano mirror is calculated via coupled mode theory as:[95]

$$|r_{fano}^{max}| = 1 - \frac{Q_{tot}}{Q_{nc}} \simeq \frac{Q_{wg}}{Q_{nc}} \tag{8.1}$$

[3] Generally, including a higher index material, i.e., the BH, in the PhC waveguide, will redshift the dispersion of the waveguide similarly to a positive L_1 shift.

[4] For this calculation, we used eq. 7.1, where the mode profile of the line-defect waveguide is considered uniform. The latest experiments showed that the effective BH index is closer to 3.26 for 1-QW BHs - for a line-defect cavity based on a 235 nm thick membrane. Thus, we believe that the latest Fano cavity design is not optimal.

where Q_{nc} is the unloaded Q-factor of the nanocavity (NC) that is dependent on the vertical scattering and absorption losses of the cavity as $Q_{nc}^{-1} = Q_i^{-1} + Q_d^{-1}$, where Q_i and Q_d are the Q-factor of the intrinsic NC and the doping-induced losses, respectively. Thus, the total quality factor of the loaded NC Q_{tot} can be written as $Q_{tot}^{-1} = Q_{nc}^{-1} + Q_{wg}^{-1}$, where Q_{wg} depends on the coupling strength of the NC to the waveguide. In the case of no doping, a high maximum reflectivity is easier to achieve since the intrinsic Q-factor of the NC can be orders of magnitude higher than the loaded Q-factor, which is in the order of several hundred. However, when doping is introduced, the maximum reflectivity drops, making phase matching critical.

Fig. 8.3(c), depicts the maximum Q-factor of the Fano cavity as a function of the absorption coefficient of the n-doped region. The maximum Q-factor closely follows a bi-exponential reduction, illustrated in the solid blue line, originating in the increased optical loss in the H0 nanocavity where most of the field resides and the decrease of the Fano mirror reflectivity.

Discussion

FDTD simulations showed that the Fano Cavity design is susceptible to parameter variations, like the PhC hole radius and the L_1 parameter. The phase condition cannot be tuned independently using a specific parameter which will also affect the Q-factor of the Fano mode via other mechanisms, e.g., the scattering of the broadband mirror or the change in the coupling strength of the NC with the waveguide. Nevertheless, lasing in the Fano mode should be possible even when considering the effective index of the BH and high absorption coefficients for the n-doping region. On the other hand, lasing will be possible only in a narrow range of PhC radii, making the control of the fabricated hole radii even more crucial.

8.2 The Q-factor of the Fano Cavity

The Q-factors of fabricated Fano cavities were measured using cross-polarization scattering spectroscopy. The Fano cavities were fabricated on a passive InP chip, and the PhC radius between the different designs was varied. Four copies of each design were placed in different locations on the chip to get information about the statistics and the robustness of the Fano cavity design.

Fig. 8.4(a) shows the scattering spectrum of a typical Fano cavity, where multiple peaks are observed. While most peaks are broad, one is narrow, exhibiting a Q-factor above 10,000. Using FDTD simulations, the only mode exhibiting a high Q-factor is the Fano mode which suggests that the mode we observe is indeed the Fano mode. The mode structure of the Fano cavity can be seen in the simulated spectra superimposed in Fig. 8.4(a). The simulated data are plotted in arbitrary units. The intensity of the collected signal of each mode is dependent on the overlap of the far-field pattern to the objective, the Q-factor of the mode, and the positioning

of the pump spot. Similarly, the intensity of each mode in the simulated spectrum depends on the monitor's position. Comparing the two spectra, we identify many similarities in the mode structure, especially for the Fano mode and its surrounding peaks; however, the comparison is not conclusive.

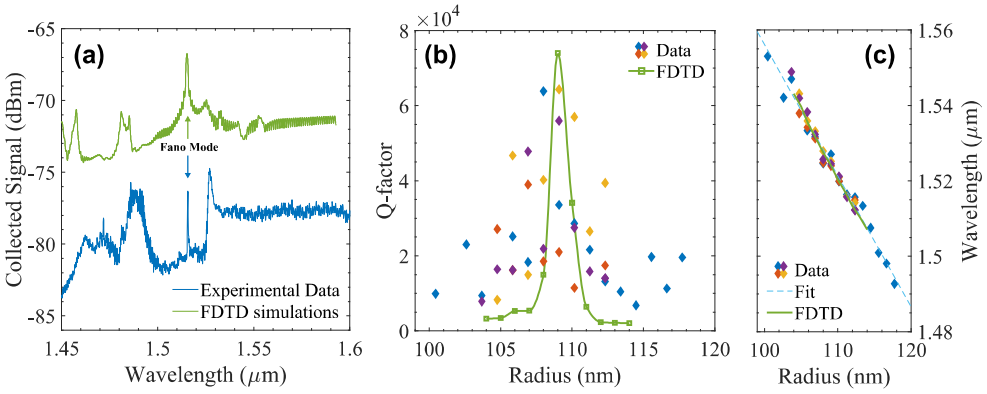

Figure 8.4 | Q-factor measurements on Fano cavities. (a) Experimental and simulated spectra of a Fano Cavity. (b) Q-factor of the Fano mode as a function of the PhC hole radius. (c) Resonant wavelength of the Fano mode as a function of PhC hole radius. The different colors of the markers in (b-c) represent the four identical groups of devices placed at different positions on the chip.

Another indication that the narrow mode is the Fano mode comes from the measurement process. Namely, the pump spot was focused on the H0 nanocavity to achieve the maximum signal-to-noise ratio (SNR) during measurement.[5] Interestingly, some signal from the Fano mode was also detected when the pump spot was focused on the broadband mirror, which acts as a scattering element to couple light in the mode. In contrast, the signal from the Fano mode vanished when the pump was focused on the LD part of the cavity. This pump spot alignment selectivity suggests that the measured mode is the Fano mode, since it mostly 'leaks' from the H0 cavity where the field is strongly localized, and secondarily from the first mirrorholes of the terminated waveguide, as shown in Sec. 5.2.

In Fig. 8.4(b), the Q-factor of the Fano mode is plotted against the PhC hole radius and is compared to the Q-factor extracted from FDTD simulations. Interestingly, there is a significant mismatch between the experimental and simulated Q-factor of the Fano mode. Firstly, the Q-factor is much less sensitive to the designed radius than predicted using FDTD simulations. In particular, the Q-factor of the Fano cavities is higher than 10,000 for a wide range of radii, supporting lasing over a wide range of wavelengths. This is also in accordance with fabricated Fano laser devices that achieved lasing in a broader range of radii than what was predicted by FDTD.

[5] Here, the SNR corresponds to the contrast between the collected signal and the background reflected pump as explained in detail in Sec. 3.4.

Secondly, the Q-factor variance for identical designs is much larger than the typical Q-factor variance of conventional LN cavities. Both of these effects can be attributed to the random disorder-induced changes to the phase condition. In other words, the disorder may severely inhibit the Q-factor of a design with optimal PhC hole radius, but may also increase the Q-factor of Fano cavity designs with non-optimal PhC radius.

Finally, Fig. 8.4(c) depicts the resonant wavelength of the Fano mode for the different radii. The simulation results are superimposed, showing a very good agreement with the experimental results. The rate of the resonance blueshift with respect to the radius is similar to the blueshift rate of the typical H0 cavity, which is in the order of 3.7 nm/nm. In addition, the variance of the resonant wavelengths between identical devices is 5 nm, which is in accordance with the typical variance of the conventional LN cavities.

Discussion

The effect of disorder on the Fano cavities fundamentally differs from that of conventional LN cavities. As described in Sec. 5.3 the disorder generally limits the Q-factor of LN cavities. However, the disorder can be beneficial for the Q-factor of the Fano mode, achieving Q-factors of several tens of thousands for designs that should be limited to the few thousands regime. Additional investigations are needed to understand these effects further. Firstly, future samples should include intrinsic nanocavities to eliminate any uncertainty in identifying the Fano mode. Secondly, the mismatch between the theory and experiments should be addressed via dedicated Monte Carlo simulations that take into account the disorder. However, faster simulation methods should be used since the FDTD method is computationally heavy.

We should also notice that when the optimal phase condition of the Fano mirror is not met, the Fano reflectivity is small and light escapes from the semi-open waveguide. Thus, only 'good' Fano cavities can be measured using cross-polarization scattering spectroscopy. This stems from the inherent limitation of the setup to detect low Q-factor modes while the vertical Q-factor remains high. This is especially important for the Fano cavities, where, in a 'bad' Fano cavity, the Q-factor will be in the order of 1,000 due to the strong coupling with the WG, while the vertical collection efficiency will still be dependent on the intrinsic Q-factor of the cavity. As a result, future test structures should include alternative coupling schemes similar to the ones described in Sec. 3.6.

8.3 Electrically-driven Fano Lasers

Electrically-driven Fano lasers were fabricated on the same chip as the LD lasers. The Fano lasers were based on the 1-QW design targeting a lasing wavelength of around 1550 nm. A schematic diagram of the devices is depicted in Fig 8.1. The Fano lasers

comprise a side-coupled H0 nanocavity, forming a cavity in the LD waveguide that is $12a$ long, where a is the PhC lattice constant chosen as 460 nm. The Fano lasers feature a BH active region that is selectively placed in the LD waveguide. The doping profile matches the length of the active region. The nanocavity is placed on the side of the n-doping region.

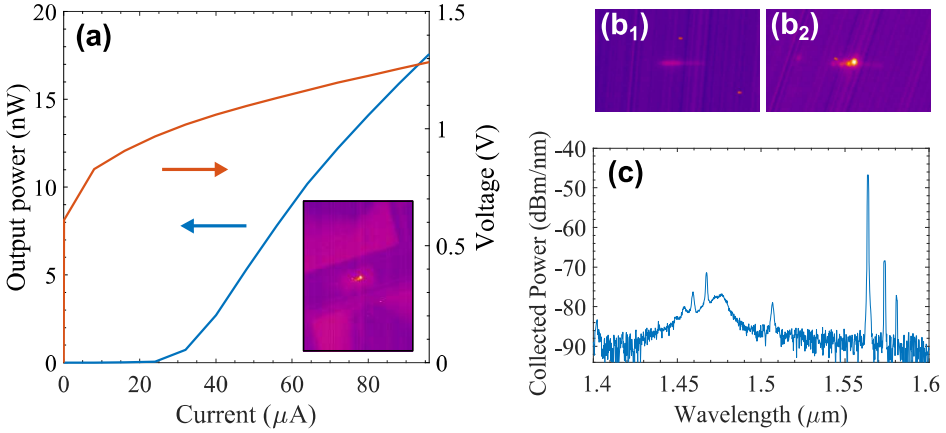

Figure 8.5 | Electrically-driven Fano laser. (a) Collected power and applied voltage as a function of the injected current. Inset: Microscope picture of the laser. (b_1) Electroluminescence from a non-lasing device. (b_2) Emission from a lasing device. (c) The spectrum of the Fano-Laser.

In Fig. 8.5(a), the LIV curve of a Fano laser featuring a BH region of length $11a$ is depicted. The collected output power of the Fano laser exhibit a characteristic kink at 28 µA, where lasing is achieved. The inset of Fig. 8.5(a) shows the microscope picture of the laser taken from an IR camera. The emission pattern of the Fano Laser shows that the laser light is emitted predominantly from the H0 nanocavity, which indicates that the lasing mode is the Fano mode. Figs. 8.5(b_1-b_2) further illustrate this effect. In particular, Fig. 8.5(b_1) shows the electroluminescence of a Fano design that did not achieve lasing. From the emission pattern, the high-intensity BH region is identified, as is the semi-open waveguide, where the propagating light scatters vertically due to disorder. In contrast, Fig. 8.5(b_2) depicts a Fano laser, whose emission profile clearly suggests that most of the light is emitted from the nanocavity which is in accordance with the mode profile depicted in Fig. 8.3(a).

Fig. 8.5(c) shows the laser spectrum over a broad wavelength range captured using a detection bandwidth of 1 nm for improved sensitivity. The spectrum also exhibits multiple high-intensity peaks, especially near the lasing mode. Identifying the Fano mode is usually done by comparing the laser mode structure with that extracted from FDTD simulations. However, such a comparison is inconclusive since multiple unidentified modes are present. More importantly, a few high-intensity side modes can be observed next to the lasing mode. To further understand the behavior

of the Fano laser devices of different BH lengths is compared.

BH Length Variations and Analysis

Fano lasers with various BH lengths were fabricated. In particular, a sweep of the PhC radius over a 30 nm range with a spacing of 1 nm was performed for three different BH lengths, namely, for BH9, BH11, and BH17, where the numbers indicate the BH length normalized to the PhC lattice constant. We should notice that for the BH9 design, the doped region does not overlap with the H0 nanocavity.

Fig. 8.6(a) shows the threshold current of Fano lasers with varying PhC radii and BH lengths, where a minimum is observed. Since random fabrication imperfections (e.g. in the IQE, and the doping) are likely to affect the threshold, more statistics is needed to conclude that this minimum is due to the optimal PhC radius of the design. However, out of all fabricated devices, lasing occurred only for a narrow set of radii, which suggests that the Fano mirror enables lasing, eliminating the possibility of a mode-gap PhC cavity formed by the BH region, like the LEAP lasers of NTT described in Sec. 1.3.1.

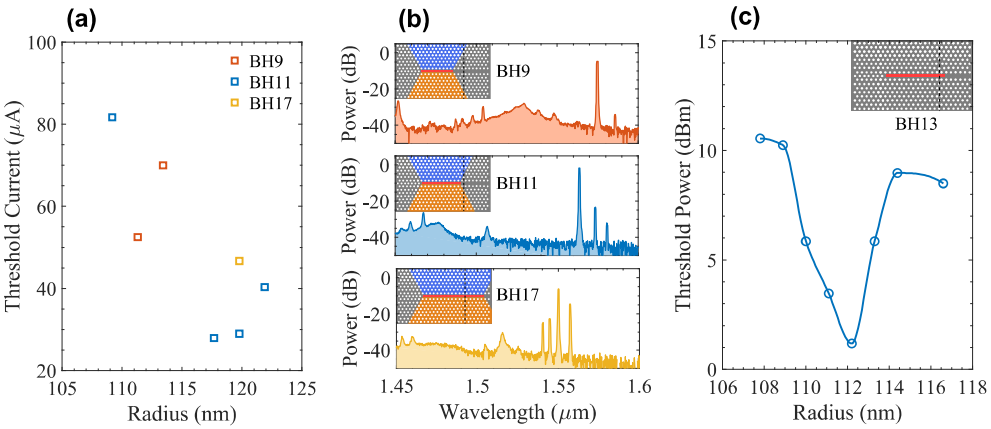

Figure 8.6 | Electrically-driven Fano lasers of different BH lengths. (a) Threshold current of Fano lasers of different PhC radius and BH length. (b) The typical laser spectra for BH9, BH11, and BH17 lasers are accompanied by the schematic diagram of each device. (c) The total incident optical power at the threshold for optically-pumped (undoped) Fano lasers, accompanied by a schematic diagram.

The typical spectra of the BH Fano lasers are shown in Fig. 8.6(b). The three lasers have a different PhC radius that translates the modes spectrally. However, the mode spacing remains constant. The number and prominence of the high-intensity side modes increase with the BH length, suggesting it plays a role in the formation of the mode structure. A similar behavior was observed in undoped optically-pumped BH Fano lasers, although the alignment of the SMF beam spot used for pumping and

collection acts as a spectral filter. As a result, we conclude that the strange modal structure stems from the BH, while the effect of doping is negligible.

Finally, the threshold of optically-pumped devices demonstrated a clear minimum in terms of PhC radius. Fig. 8.6(c) shows the incident optical power at the threshold for undoped BH13 Fano lasers. The solid blue line is a guide for the eye. This is a consistent phenomenon since similar behavior was found in other groups of optically-pumped Fano lasers. Finally, the existence of a minimum in the threshold of optically-pumped Fano lasers suggests that the minimum observed in the threshold of electrically-pumped Fano lasers is not an artifact and will be reproduced in future samples.

Discussion

Electrically-driven Fano lasers were realized, and multiple indications suggest that the Fano lasers lase in the Fano mode. However, more measurements and statistics are required to confidently claim that lasing mode is not formed via the mode-gap effect of the BH waveguide.

Most importantly, passive Fano Cavities and intrinsic H0 nanocavities must be included in future samples to compare the lasing wavelength with the corresponding Fano and H0 modes. Secondly, we observe that the collected power for the 1-QW Fano lasers is as low as their LN counterparts. In particular, the collected power level of the lasers is at the limit of the sensitivity of our measuring equipment used to do more advanced measurements, like the laser linewidth or the relative intensity noise. As a result, efficient outcoupling schemes should be targeted in future designs.

8.4 Summary

This section describes the preliminary investigations toward achieving electrically-driven Fano Lasers. Firstly, 3D-FDTD simulations were conducted to understand the design principles behind FL cavities, while the effect of doping and the effective BH index was discussed. The numerical investigations confirmed that lasing in electrically-driven Fano devices is possible if the nanocavity is placed in the n-doped region. However, the n-doping and BH region severely reduce the Q-factor of the Fano mode, making the design exceptionally susceptible to hole radius variations.

In addition, Q-factor measurements were performed where the Fano mode was identified. A statistical analysis of the Fano cavity designs verified that the Q-factor is sensitive to disorder, exhibiting a significant variance in the Q-factor of the optimal design. Simultaneously, disorder acts beneficially on the Q-factor of non-optimal designs, increasing the Q-factor far beyond what deterministic FDTD simulations predict. This critical mismatch between theory and experiment should be investigated further via Monte Carlo simulations.

Finally, a preliminary investigation of electrically-driven Fano lasers was conducted. In particular, successful lasing was observed, although we cannot verify that

the lasing mode is the Fano mode using the laser spectra. However, the emission pattern and narrow radius range of lasing devices strongly indicate that the lasing mode relies on the Fano mirror and might indeed be the Fano mode. In the future, these investigations should be extended to the characterization of intrinsic H0 nanocavities to directly identify if the lasing mode matches the resonance of the fundamental mode of the intrinsic H0 cavity.

CHAPTER 9

Conclusion and Outlook

This last chapter concludes the thesis by summarizing the main results and achievements, as well as providing an outlook.

9.1 Conclusion

The aim of this project was the realization and study of electrically-pumped photonic crystal lasers. This goal was not only achieved but record-breaking results were accomplished by demonstrating the first sub-µA threshold laser at room temperature and in continuous wave operation. Furthermore, this work contributed to the further understanding of the physical mechanisms governing photonic crystal lasers and also to the available characterization techniques.

During this work, we investigated and established new experimental methods. An experimental setup for cross-polarization resonant scattering spectroscopy was established, enabling the direct experimental measurement of the intrinsic quality factor of photonic crystal cavities. Significant time was spent on understanding the limitations and optimizing the setup leading to a novel characterization of doped photonic crystal cavities. This measurement setup was critical for this project but is also utilized in a variety of other experimental activities of our group. In addition, radio-frequency modulation measurements of laser dynamics were conducted, establishing the experimental procedure. These measurements offer the possibility of characterizing the lasers using their small-signal response, accessing information unavailable using the typical input-output curves. Finally, electroluminescence and photoluminescence measurements were established, which enabled the qualitative understanding of the fabrication limitations of our lasers.

Significant research was directed on characterizing the quality factor of photonic crystal cavities intended for laser applications. A systematic numerical investigation of all the photonic crystal parameters affecting the resonant wavelength and the quality factor of the lasing mode was conducted. Furthermore, a numerical optimization method of the quality factor was established based on the visualization and subsequent minimization of the leaky field components. Finally, an experimental investigation of intrinsic and doped photonic crystal cavities was conducted to quantify the effect of

disorder and doping on the quality factor of the actual laser cavities. By comparing the experimental results with numerical simulations, we concluded that the quality factor of the laser cavities was limited by the doping-induced optical losses leading to a maximum quality factor of 21,000. Moreover, we measured the absorption coefficient of the p-doping region to be 120 cm^{-1}, which was not measured before. We believe that this novel characterization technique will be influential in the field of photonic crystal lasers in the future.

The experimental demonstration of electrically-driven photonic crystal lasers featuring a buried-heterostructure active region and a lateral carrier injection scheme was realized. The electro-optical properties of these lasers were characterized, along with their thermal characteristics. In particular, the lasers exhibited minimal self-heating below 10 K under typical operating conditions. The comparison of different laser showed that the level of self-heating is determined by the optical intensity confined in the cavity, while the ohmic losses were negligible. However, the lasers were found to be sensitive to ambient temperature increase, and were found to have a characteristic temperature of 35 °C for both 1-QW and 3-QWs lasers. Moreover, by conducting a series of independent experiments, we identified the leakage current as the primary limiting mechanism of the injection efficiency. In particular, a comparison between optical and electrical pumping showed that the injection efficiency is reduced with the injected current and applied voltage, while electroluminescent measurements showed significant InP emission from the p-i interface due to the low mobility of the holes. Thus, a trade-off between the doping-induced optical losses and the injection efficiency was identified when varying the offset of the p-doping region. Finally, significant leakage suppression was observed when isolation trenches were included, even at low bias voltage.

Then, a systematic investigation of the size of the buried-heterostructure active region was conducted. Numerical simulations showed that the doping-induced absorption losses scale with the modal gain, allowing efficient miniaturization of the active region. Fabricated L7 lasers with varying active region lengths showed that the laser threshold trend does not follow the established macroscopic laser theory. The injection efficiency decreases with the threshold voltage. This experiment also led to the demonstration of the semiconductor laser with the world's smallest threshold current to date. In addition, the small-signal analysis showed that photonic crystal lasers feature high modulation efficiencies, although the damping limits the maximum modulation bandwidth. Lasers with smaller active region were found to have higher damping, while the 3-QW laser's performance agreed well with previous demonstrations in the literature. However, smaller lasers are energy efficient, and an energy cost below 1 fJ/bit was estimated for typical processor clock frequencies.

Finally, a preliminary investigation towards the realization of the first electrically-driven Fano laser was conducted. FDTD simulations of different Fano cavities showed that the Q-factor of the Fano mode is very sensitive to all design parameters. Specifically, the effect of radius in combination with the BH effective index and doping was studied, showing that lasing is possible but at a very narrow range of designed radii where the oscillation condition is maximally satisfied. Secondly, Fano cavities

fabricated on passive InP chips were characterized using cross-polarization scattering spectroscopy. The Q-factor of the Fano mode was characterized for designs with radii, revealing a significant sensitivity to the fabrication disorder. Finally, successful lasing was observed from multiple Fano laser devices. Several indications suggest the devices lase in the Fano mode; however, comparing the laser spectra with simulations was inconclusive and more measurements are required.

9.2 Outlook

The photonic crystal lasers demonstrated in this work have the potential for high-efficiency low energy consumption devices for future on-chip optical interconnects. However, there are numerous possibilities for improvement in the fabrication and laser design, which can lead to better performance. The primary performance-limiting processes stem from the p-doping definition, the leakage current, and the quality of the active material.

Better control of the p-doping profile is needed, and a systematic investigation should be conducted to find the optimal distance between the p-i interface and the center of the cavity. Furthermore, new characterization methods should be employed to assess and optimize the p-doping level. The leakage should be further suppressed by electrically isolating the devices. In particular, the electrical pads should not be shared between devices. In addition, new photonic crystal cavity designs featuring isolation trenches should be employed to reduce the leakage at the expense of higher resistance. Most importantly, drift-diffusion simulations should be performed to replicate and understand the experimental findings. Successful electrical simulations will expand our knowledge of the properties of the nanolasers and facilitate better designs in the future.

Furthermore, direct measurement and statistics of the internal quantum efficiency of the buried heterostructure active regions are required. The quality factor investigations showed that the fabrication disorder does not limit the laser performance. Thus, statistical investigations should be performed on optically-pumped devices to eliminate doping-induced uncertainties. Such systematic investigation can help assess the control over the quality of the buried heterostructure.

For the quality-factor measurements of passive cavities, designs with input waveguides should be included, while the signal collection should be done from the top of the optical cavity using a high numerical aperture objective. Similarly, linewidth and quantum noise measurements are limited by the collected laser power and could not be performed during the project due to poor collection efficiency. Out-coupling schemes should be included in the designs for the second generation of devices. However, since the buried-heterostructure wafers tend to exhibit high defect density, the coupling schemes should be limited to compact wavelength-scale grating couplers and optimized design cavities featuring high quality-factors and optimized far-field patterns for high coupling efficiency to the objective. In the third generation of devices,

Silicon-on-Insulator waveguide circuitry and on-chip optical links should be targeted since most of the required technology has already been developed.

New designs for electrically-driven photonic crystal lasers should be explored to achieve a higher degree of miniaturization and lower energy consumption. In particular, novel designs should be developed using topology optimization targeting ultra-small active regions while maintaining high confinement and quality factors. Novel 1D nanobeam laser designs featuring a buried heterostructure and lateral carrier injection should be explored, as they have better heat sinking and mechanical stability. Finally, electrically-driven Fano lasers should be demonstrated by auxiliary characterization of the intrinsic nanocavities, while the Fano cavities should be redesigned to increase the out-coupling efficiency enabling advanced measurements, like linewidth and THz modulation, that require high output power.

All in all, photonic crystal nanolasers are strong candidates for on-chip optical interconnects. The photonic crystal platform offers strong spatial and temporal confinement of light, enabling the required miniaturization of the laser sources for low-power consumption, high-efficiency lasers. The primary limitations of their performance stem from the quantum efficiency of the active material and the doping geometry that leads to poor injection efficiency and optical losses. However, these limitations are not fundamental, and careful design and optimization of the fabrication process can alleviate these issues. Since silicon photonics have already been introduced to commercial products for chip-to-chip communication, integrating sophisticated optical interconnects on-chip is the next natural step. Ultra-low power consumption lasers are the centerpiece of this sustainable technology of the future that will transform computing.

APPENDIX A

Statistics on PhC lasers

Complementing Sec. 2.3 and Sec. 7.3, a laser mapping for the horizontal devices of Group 1, is shown in Fig. A.1(a) highlighting the variance in the threshold. We should also notice that every second device does not work - an effect observed consistently across multiple wafers - associated with the parity of the p-doping profile. Group 1 has four different doping profile parities since each contact is shared between four devices. Thus, a misalignment of $(\Delta x, \Delta y)$ in the DUV mask will affect each parity group differently.

In Fig.A.1(b), a sketch to explain this effect is drawn, where the BH and the doping profile are drawn in red and orange, respectively. For comparison, a perfectly aligned DUV mask is outlined with a black dashed line. In this example, the mask is misaligned more in the x-direction, showcasing that each parity group will be affected differently. In particular, groups I and IV will be critically misaligned, and the device will not lase due to the recombination of the carriers outside of the BH (see Sec. 6.3). Devices in group III will achieve lasing, although the doping losses will be larger, while group II will exhibit the best performance. A good estimate for the optimal and critical p-doping offset has yet to be identified. The DUV mask misalignment is a systematic error that kills half of the devices in each wafer and should be addressed.

Furthermore, statistics on the threshold current of the BH lasers of Ch. 9 are provided. In Fig. A.1(c), the laser threshold is plotted against the BH length. For shorter BH lengths, less available gain and the nonidealities in the device quality can critically hinder the device performance - thus, a smaller number of devices achieve lasing. For the same reason, smaller devices that achieve lasing have a higher probability of exhibiting good performance. On the other hand, longer BH lengths provide more gain, while the nonidealities of the device are averaged out, leading to a higher yield but worse characteristics. Unlike the DUV mask misalignment, the variance of the threshold stems from random defects in the BH material or doping. Despite the significant variance in the threshold, the resulting trends can be trusted, assuming that the best devices' performance is indicative of a pristine device fabricated using an optimized process flow of high uniformity and high yield.

Finally, the threshold current is plotted against the laser wavelength as shown in Fig. A.1(d). For highly-efficient low-threshold lasers, the resonant wavelength of the laser cavity should maximally overlap with the PL peak. In practice, however,

we observe a uniform distribution suggesting that the limiting factors in the laser performance are the randomness of the doping-induced losses and the IQE of the individual devices.

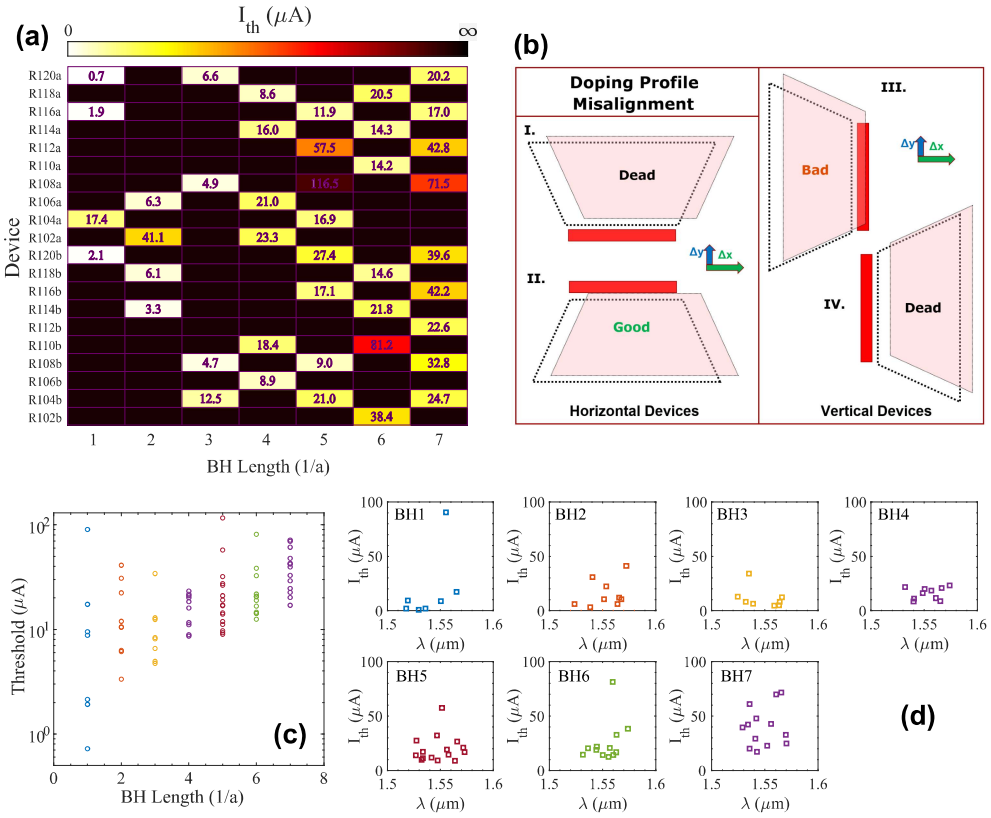

Figure A.1 | Threshold and death statistics of PhC lasers. (a) Threshold mapping for the Horizontal Lasers of Group 1. (b) Sketch of the DUV mask misalignment for the p-doping profile creating four distinct doping variants due to the shared doping profile. (c) Statistics on the threshold current versus the BH length. (d) Threshold current as a function of the central laser wavelength.

APPENDIX B

Optical Links using Photonic Crystal lasers

A preliminary investigation on Optical Links was also conducted. The optical links are based on PhC laser diodes (LD) coupled to a PhC waveguide leading to a photodiode (PD) forming an on-chip optical link. Fig. B.1(a) shows a picture of the laser setup featuring four magnetic probes to independently apply a DC bias on the LD and the PD. A microscope picture of an optical link is illustrated in Fig. B.1(b). A schematic diagram of the device is depicted in Fig. B.1(c); the LD consists of an optimized L5 laser coupled to a W1 that is placed three PhC rows away from the center (cavity) row. The loaded Q-factor is 7,000. The light propagates through a waveguide made of a line defect and is led to a PD that consists of a 13.2µm long BH region with a matching doping profile. To measure the photocurrent, the PD is operated in reverse bias.

Fig. B.1(c) depicts the LIV characteristic of the LD, where the light was collected via a 50x objective. A clear transition to lasing is observed around 55 µA. For comparison, the measured PD current is plotted as a function of the LD current in Fig. B.1(d) for various reverse biases. As the reverse bias increase, the number of collected carriers increase; however, there is no dependence of the photocurrent on the output power of the LD.

Part of the reason is found in the non-optimal loaded Q-factor, which can be expressed using eq. 4.7, where Q_{wg} is the Q-factor related to the coupling strength of the cavity and the waveguide. Although, the intrinsic Q-factor of the cavity should exceed 100,000, Q_{wg} strongly depends on the PhC radius and can vary from 5,000 to 10,000 depending on the enlargement factor of the PhC holes. Furthermore, the coupling to the waveguide is severely hindered by the doping losses that were initially neglected. In particular, the actual unloaded Q-factor - where the doping losses are included - is estimated at 8,000, and thus the coupling efficiency to the waveguide should be close to 50% since $\eta_c = Q_{wg}^{-}/Q_{tot}^{-1}$.

Nevertheless, the low coupling efficiency to the W1 does not fully explain why no photocurrent was observed. To understand this, we should consider the dispersion of the W1 waveguide. In Fig. B.1(e), the lasing peak is superimposed on the EL

spectrum of the PD when forward-biased at 700 μA. The densely-spaced peaks of the PD spectrum reveal the band-edge of the W1 of the BH. Due to disorder, random optical cavities can be created at the slow-light regime,[122] above which a sharp cutoff in the transmission is observed.[206] The fundamental mode of a line-defect cavity is blueshifted compared to the band-edge while asymptotically reaching it for longer cavity lengths.[157] This also holds true for the L5 spectrum of Fig. B.1(e). However, the dispersion of the W1 is strongly affected by the existence of the BH region. In contrast, the dispersion of a passive W1 waveguide is expected to be blueshifted by more than 10 nm. As a result, the laser light is expected to be beyond the slow-light regime of the passive waveguide and experience minimal transmission. In future designs, the dispersion of the passive W1 should be engineered to compensate for the redshift caused by the BH.

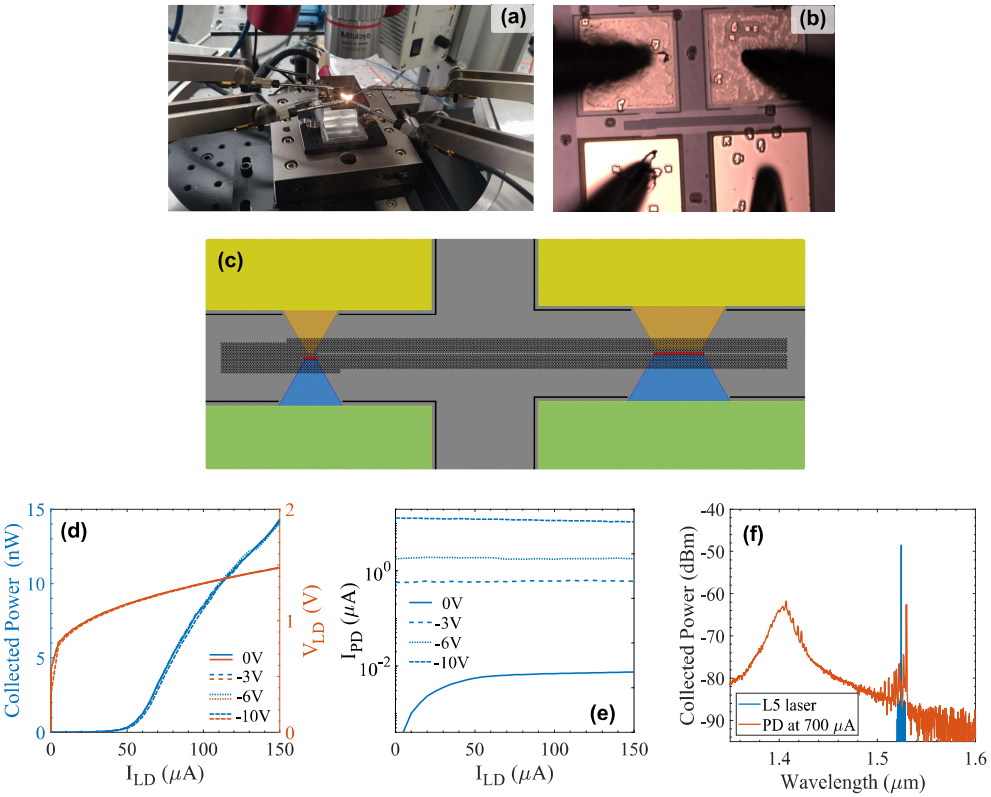

Figure B.1 | On-chip optical links. (a) Laser Setup for optical link characterization. (b) Microscope Picture of a PhC optical link. (c) Schematic Diagram of an L5-based optical link. (d) LIV characteristic of the L5 laser for different PD applied biases. (e) PD current as a function of the laser current for different reverse biases on the PD. (f) EL spectra for the laser at 100 μA and the PD at 700 μA.

APPENDIX C

Leaky-Field Component Calculation

The following matlab-based script is an algorithm for extracting the leaky field components of the a PhC mode profile extracted from 3D-FDTD simulations:

```
clc; clear all;

%% Extract Data from FDTD
ResultFolder = pwd;
load('HERO_L3_mode'); % Load profile monitor data

% Field Profile
Ey=real(Ey).'; % Real-part of Ey
Ex=real(Ex).'; % Real-part of Ex
E0= sqrt(abs(Ey).^2+abs(Ex).^2); % Calculate E0

% Real-space coordinates - re-centering
x= (x- x(ceil(end/2), :)); % Center x-vector in [m]
y= (y-y(ceil(end/2), :)); % Center y-vector in [m]

% Other parameters
lambda_res=1550e-9; %Resonant wavelength from Q-analysis in FDTD in [m]
a=440e-9; %Extracted from model in FDTD in [m]

%% Fourier Transform
% k-space coordinates
kx_range= 1/(x(2)-x(1)); % Get the range for ky
ky_range= 1/(y(2)-y(1)); % Get the range for ky
kx= a*linspace(-(kx_range/2),(kx_range/2),length(x)); % Calculate kx in [2 pi/a]
ky= a*linspace(-(ky_range/2),(ky_range/2),length(y)); % Calculate ky in [2 pi/a]
k_res= 1/lambda_res*a; % normalized k-radius of the light cone (n_air = 1)
```

```
27
28
29 %Fourier Transform of the fields
30 %Fast FT and shift the zero-frequency component to the center of the array
31 Ey_kspace= fftshift(fft2(Ey)); %FT for Ey
32 Ex_kspace= fftshift(fft2(Ex)); % FT for Ex
33
34 %% Get the leaky components in k-space
35 % Define the FT leaky fields
36 Ey_k_leaky=zeros(size(Ey_kspace)); %Prelocate leaky FTEy field with zeros
37 Ex_k_leaky=zeros(size(Ex_kspace)); %Prelocate leaky FTEx field with zeros
38
39 %Bandpass filter in k-space to get the leaky components
40 for i=1:length(kx) %scan over all kx_i
41     for j=1:length(ky) % scan over all ky_i
42         if ( kx(i)^2+ky(j)^2 <= (k_res/a)^2 ) % if in cone of light, else 0
43             Ey_k_leaky(i,j)=Ey_kspace(j,i);
44             Ex_k_leaky(i,j)=Ex_kspace(j,i);
45         end
46     end
47 end
48
49 %Transpose the FT leaky fields
50 Ey_k_leaky=transpose(Ey_k_leaky);
51 Ex_k_leaky=transpose(Ex_k_leaky);
52
53 %% Inverse fourier of the leaky components
54 %Inverse Fourier Transform of the leaky part
55 %Fast IFT and shift the zero-frequency component to the center of the array
56 Ey_ift=ifft2(ifftshift(Ey_k_leaky)); % IFT for Ey
57 Ex_ift=ifft2(ifftshift(Ex_k_leaky)); % IFT for Ex
58
59 %Get the Energy of each leaky field component, and the total leaky field
60 Leaky_E2y=abs(Ey_ift).^2;
61 Leaky_E2x=abs(Ex_ift).^2;
62 Leaky_E2=Leaky_E2y+Leaky_E2x;
```

APPENDIX D

RF Measurements

Our group has not previously performed radio-frequency (RF) measurements; thus, this Appendix is mainly used to list comments on the measurement setup. Special thanks should be given to Dagmawi Bekele and Gaoneng Dong for their help and guidance.

D.1 Measurements and Calibration

A picture of the RF-Laser Setup is shown in Fig. D.1(a), and its schematic is shown in Figs. 3.1(a) and 3.3.

The VNA model used in these experiments is the *HP 8722A*. The desired modulation range and magnitude (power) of the modulation are set up in the VNA. Table D.1 shows the conversion between the power and actual peak-to-peak AC voltage V_{AC}^{pp}, as measured using an oscilloscope. The calibration is only valid for a given frequency range and RF power, i.e., any changes in the measurement parameters require re-calibration. Therefore, the RF power should be determined before the actual measurement.

Calibrating the measurement setup is crucial for getting the S-parameters. The S-parameters S_{11} and S_{21} can be seen before and after calibration in Fig. D.1(c) and Fig. D.1(d-e), respectively. Even after calibration, the frequencies below 1.5 GHz are irregular, which is attributed to the VNA.

Table D.1 | Conversion from the RF Power Range of the *HP 8722A* VNA to the applied peak-to-peak AC voltage V_{AC}^{pp}.

VNA Power	1-2	3	4	5	6	7	8	9	10
$\mathbf{V_{AC}^{pp}}$ **(mV)**	NaN	200	120	100	55	30	17	6	3

Modulation Power

- Before the measurement, the DUT should be modulated at a constant frequency, and its spectrum should be inspected in the OSA. Fig. D.1(b) shows the laser

spectrum when modulated at a constant frequency of 5 and 10 GHz. For a good measurement, the sidebands should be visible. The prominence of the sidebands depends on the RF power (peak to peak V_{AC}).

- The modulation power (V_{AC}^{pp}) required is still not well-understood or optimized. Even low RF powers (20 mV) should be enough to modulate the laser by more than 4 µA (at high pumping), and a weak linewidth broadening can be observed. However, this was insufficient for a good S_{21}, and the V_{AC}^{pp} was chosen as 100 mV. The corresponding modulation current depends on the differential resistance of the DUT.

VNA and cables

- Port #1 should be calibrated with the cable right before the RF probe. The RF cable should be fixed for calibration and measurement for the best results. Port #2 should be calibrated directly; however, a connection adapter is needed, introducing errors in the calibration. In the future, a matching Cal kit should be purchased.

- Since only the relative shape of the S_{21} is needed, calibrating S_{11} and S_{22} individually should have been sufficient, and a unitary 'Through' measurement could have been assumed. Unfortunately, the VNA's algorithm needs the Through measurement for an S_{21} correction. As a result, the calibration substrate that would calibrate the RF probes cannot provide a Through measurement. Unfortunately, SOLT calibration is impossible for the DUT and thus can only happen for the VNA and the RF cable. There might be more advanced calibration methods where the Through is unknown and should be investigated for future measurements.

Sensitivity and Noise

- The main limitation in terms of power is the sensitivity of the PD. Femtolab's PD can detect signals between -25 dBm and a few dBm; thus, multiple EDFAs can be used in series. We consider a good signal to have power larger than -15 dBm (after amplification) and a good contrast with the ASE background of the EDFA. In reality, even if the laser power is lost in the EDFA background, a good S_{21} can still be observed due to the high sensitivity of the homodyne measurement. As a rule of thumb, signals down to -65 dBm (before amplification) can be measured.

- There are ranges in the EDFA gain spectrum ([1510-1525] nm and [1560, 1568] nm) with very weak gain. An additional EDFA or SOA can be used at these ranges to boost the signal. Thankfully, amplification does not affect the quality of the signal. Furthermore, filtering the EDFA background is not crucial. At some point, the BPF of the last EDFA was omitted by mistake, which resulted

in no visible degradation of the S_{21} trace. This is another indication of the robustness of the measurement in terms of noise.

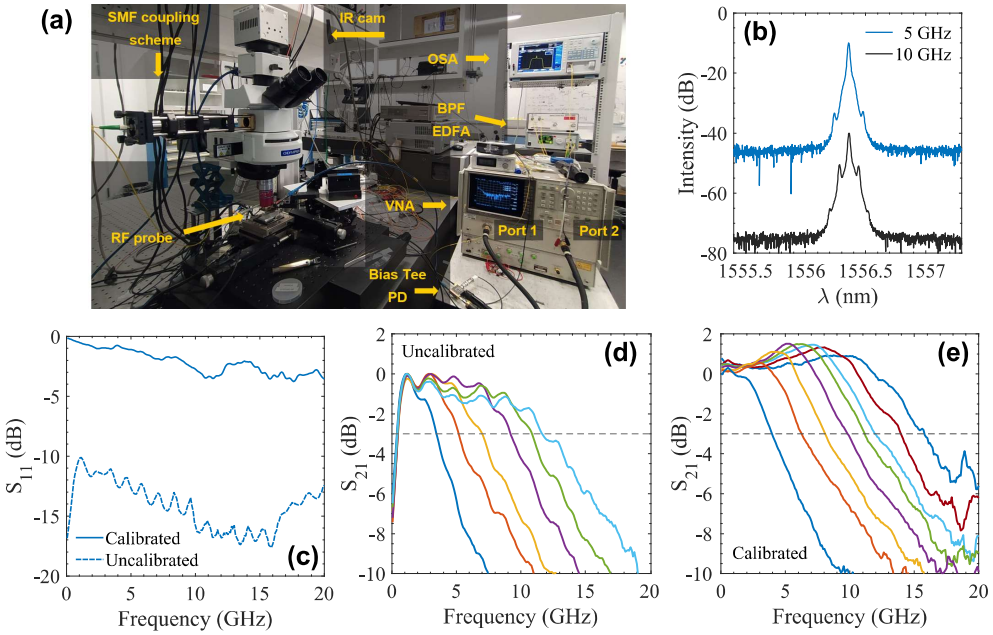

Figure D.1 | RF measurements. (a) The RF setup used for the measurement of the modulation response. The Laser Setup is modified to couple the vertically-leaking laser light to an SMF fiber. (b) The modulated laser spectrum at constant frequencies. (c) S_{11} trace before and after calibration. (d) S_{21} traces for different pump levels before calibration. (e) S_{21} traces for different pump levels after calibration.

D.2 Modulation Response of BH lasers

The modulation response (MR) of the BH1, BH3, BH7, and the 3QW-BH7 is depicted in Fig. D.2. As the BH size increases, the damping drops; however, all 1QW lasers are overdamped, and the conventional strong response (MR > 0-dB) for frequencies close to the relaxation oscillation frequency is not observed. In comparison, the 3QW laser does exhibit weaker damping due to the higher differential gain. It should also be noted that the response at low frequencies (< 1.5 GHz) is irregular and cannot be trusted. This erratic behavior is related to the VNA and not to the lasers or due to the impedance mismatch. Thus, the low-frequency part should be excluded during the response function fitting.

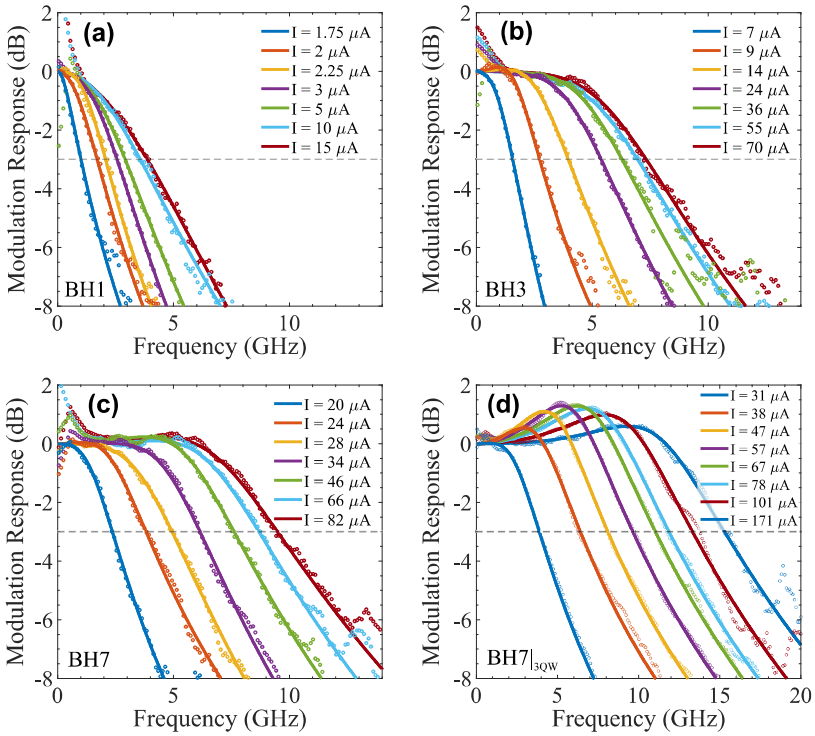

Figure D.2 | Modulation response (MR) of BH lasers. (a) MR for BH1 laser. (b) MR for BH3 laser. (c) MR for BH7 laser. (d) MR for BH7-3QW laser.

APPENDIX E

Fano Laser Design

The design parameters for two designs of an H0-based Fano laser are listed in Fig. E.1. In particular, the first Fano cavity was designed by Yi Yu, targeting a 250 nm thick InAs quantum-dot-embedded InP membrane. Due to the low density of the QDs, their effect on the refractive index of the InP slab can be neglected. This design targets an emission of 1570 nm. The second Fano cavity was designed by the author targeting a 1QW-BH Fano laser with a center wavelength at 1550 nm. The design assumes that the active material is selectively placed in the line-defect (LD) waveguide and has an effective refractive index of 3.2.[1]

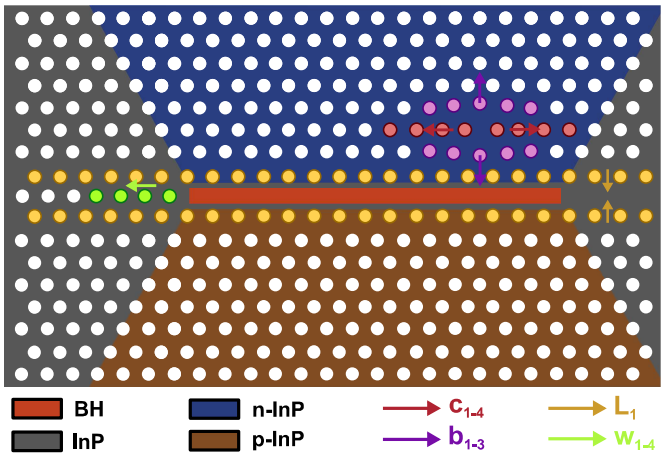

Design Parameters	QD (1570nm)	1QW (1550nm)
r (nm)	109	109
a (nm)	464	460
c_1 (a)	0.164	0.165
c_2 (a)	0	0
c_3(a)	-0.009	-0.009
c_4 (a)	-0.006	-0.007
b_1 (a)	0.153	0.000
b_{2x} (a)	0.060	0.061
b_{2y} (a)	0.034	0.035
b_{3x} (a)	0	0
b_{3y} (a)	0.004	0.004
L_1 (a)	0.170	0.107
w_1 (a)	0.328	0.291
w_2 (a)	0.190	0.191
w_3 (a)	-0.030	-0.030
w_1 (a)	-0.006	-0.007

Figure E.1 | Fano laser designs based on an H0 nanocavity for QDs and 1QW. The PhC holes whose position deviates from the lattice are colored and named depending on their functionality. Similarly, the intrinsic, doped, and BH active regions are color-coded.

[1] Later experiments (see Sec. 7.2) showed that the effective refractive index of a 1QW BH is approximately 3.26.

For both designs, the intrinsic Q-factor of the H0 cavity exceeds 500,000, while the loaded Q-factor is below 1000. In particular, the H0 cavity is optimized by shifting the surrounding holes away from the point defect; c_i and b_i shifts are considered positive when shifting the i^{th} hole away from the point defect. Similarly, positive w_i shifts represent the position shift of the end-mirrorholes away from the LD cavity, which is in accordance with the gentle confinement principle in LD cavities as described in Sec. 5.2. Finally, the L_1 holes' shifts correspond to shifting the PhC hole rows adjacent to the LD waveguide towards its center. Increasing L_1 increases the coupling strength of the H0 to the LD waveguide and redshifts the dispersion of the W1. Hence, excessive L_1 shifts will bring the band-edge closer to the resonance of the H0 cavity introducing slow-light effects. A similar redshift of the waveguide dispersion is caused by embedding a high index material in the line defect, i.e., a buried-heterostructure QW region.

APPENDIX F

Process Flow

This chapter presents the detailed step-by-step, optimized process flow for the fabrication of electrically-driven BH PhC membrane lasers. The passive InP-based devices with and without doping that are used in the thesis use a subset of this process flow, so it was omitted. The process flow was updated in February 2023.

Step Heading	Equipment	Procedure	Comments
1. Initial steps before bonding			
1.1. MOVPE sample growth			
1.1.1. Epitaxial growth	MOVPE	Grow InP with active QWs or QDs layers + $Ga_{0.47}In_{0.53}As$ sacrificial layer (d = 100 nm is enough)	InP layer thickness: d = 180 - 220 nm (QW layer dependent; aiming for the final device thickness of d = 250 nm)
1.1.2. PL characterization	PL mapper	532/980 nm, surface-map/wide-scan	Make sure the settings used are consistent.
1.2. Si thermal oxidation			***Si substrate 100mm***
1.2.1. Thermal oxidation	Furnace: Anneal-oxide (C1)	Wet oxidation at 1100°C for 4h05min; Annealing for 20min	Expected SiO_2 thickness ~1085 nm
1.2.2. SiO_2 thickness measurement	Ellipsometer VASE		
2. Formation of alignment marks in Si			
2.1. AZ5214 spin-coating			***Si substrate 100mm***

Step Heading	Equipment	Procedure	Comments
2.1.1. AZ5214 spin-coating	Spin coater: Gamma UV	Sequence 3411 and 4111 on Gamma UV, 4111 on Gamma e-beam & UV DCH 100mm 5214E 1.5um HMDS.	Before spin-coating, handle wafers with care to avoid introducing particles on the surface! Expected thickness 1.5um with HMDS.
2.2. UV exposure			
2.2.1. UV exposure	Aligner MA6-2	Mask "HERO GEN 1.5 NATEC ALIGN MARKS' (dark field); Flat alignment; Hard contact mode; Time 7s, intensity 11 mW/cm2	Exposing alignment marks and other markings. UV mask tends to get dirty fast and the quality of exposure decreases!
2.3. AZ5214 development			
2.3.1. Development	Developer: TMAH UV-lithography	Sequence 1002: DCH 100mm SP 60s	Check under the microscope if the structures look properly.
2.4. Descum			
2.4.1. Plasma ashing	Plasma Asher 2	10 s, 0.8 mbar, O_2 = 300 ml/min, power 400 W	The descum step is to make sure openings have no resist residues.
2.5. AOE etching of SiO_2			
2.5.1. Dry etching	AOE	Chiller temp: 0 °C, Recipe: SiO_2_RES, Time: 8:00 min	Set the chiller temperature at least 30 min before etching. Run TDESC3MIN chamber cleaning after each or every other Si wafer etching.
2.5.2. Chamber cleaning	AOE	Chiller temp: 5 °C, Recipe: TDESC10MIN, Time: 10:00 min	Cleaning can run while the chiller is heating up to 5 °C
2.6. Resist strip			
2.6.1. Resist strip	Resist strip Wetbench 06	Remover 1165, ultrasonic level 9, 60 min, Rinse, IPA, ultrasonic level 9, 5 min, DIW rinse: Program 01 (bath fill, 3x cycles of rinsing, 4 min DIW rinse)	AZ resist strip after dry etching might be a bit difficult, go for 60 min from the beginning, and after IPA rinse look at the wafers and consider if longer Remover 1165 step is needed.
2.6.2. Blow dry	Resist strip Wetbench 06 (or Solvents fumehood)	Blow dry using N_2 gun	This step might drop particles on the wafers. Consider cleaner wafer drying methods (spin-dryer?).

Step Heading	Equipment	Procedure	Comments
2.7. AZ5214 spin-coating			
2.1.1. AZ5214 spin-coating	Spin coater: Gamma UV	Sequence (3411 on Gamma UV, 4111 on Gamma e-beam & UV) DCH 100mm 5214E 1.5um HMDS. It includes: 1) HMDS priming, 2) Dispense 3ml@800rpm; 3) Spin-off for 30s@4500rpm; 4) Soft baking for 90s@90C.	Before spin-coating, handle wafers with care to avoid introducing particles on the surface! Expected thickness 1.5um with HMDS.
2.8. UV maskless exposure			
2.8.1. UV maskless exposure	MLA2/MLA3	Design: "ausa_Mask_preAM _HEROgen1-5_NATEC_labels-removed_' With alignment. Settings for MLA3: Dose: 80 mJ/cm2, Defocus: -2, Exposure mode: Quality, Exposure Time: 13:00 min	Exposure of preAM openings around previously exposed and etching alignment marks. Very high alignment and exposure precision are not needed, it is better to overexpose.
2.9. AZ5214 development			
2.9.1. Development	Developer: TMAH UV-lithography	Sequence 1002: DCH 100mm SP 60s	Check under the microscope if the structures look properly.
2.10. Descum			
2.10.1. Plasma ashing	Plasma Asher 2	10 s, 0.8 mbar, O_2 = 300 ml/min, power 400 W	Descum step is to make sure openings have no resist residues.
2.11. AOE etching of Si			
2.11.1. Dry etching	AOE	Chiller temp: 5 °C, Recipe: Si_etch2, Time: 5:00 min	Etching AM into Si with SiO_2 mask while etching preAM opening in SiO_2 with AZ resist mask. Run TDESC3MIN chamber cleaning after every other Si wafer etching.
2.11.2. Chamber cleaning	AOE	Chiller temp: 5 °C, Rec: TDESC10MIN, Time: 10:00 min	

Step Heading	Equipment	Procedure	Comments
2.12. Wet etching of SiO_2 in preAM openings			
2.12.1. Wet etching	Si acid/base fumehood	BHF, 10 min	Use special horizontal Teflon holder for 4' Si wafers and big plastic beaker for ∼1l BHF to etch many wafers at once. BHF etching rate of thermal SiO_2 should be around 80 nm/min.
2.12.2. Blow dry	Si acid/base fumehood	Blow dry using N_2 gun	Consider searching for cleaner wafer drying methods (spin-dryer?).
2.13. Resist strip			
2.13.1. Resist strip	Resist strip Wetbench 06	Remover 1165, ultrasonic level 9, 60 min, Rinse, IPA, ultrasonic level 9, 5 min, DIW rinse: Program 01 (bath fill, 3x cycles of rinsing, 4 min DIW rinse)	AZ resist strip after dry etching might be a bit difficult, go for 60 min from the beginning, and after IPA rinse look at the wafers and consider if longer Remover 1165 step is needed.
2.13.2. Blow dry	Resist strip Wetbench 06 (or Solvents fumehood)	Blow dry using N_2 gun	This step might drop particles on the wafers. Consider cleaner wafer drying methods (spin-dryer?).
3. Plasma-activated bonding			
3.1. Surface activation by plasma			***2' InP, 4' Si w/ SiO_2 with alignment marks***
3.1.1. Chamber cleaning	Plasma Asher 1	Gas: O_2: 210 ml/min, N_2: 70 ml/min, Power: 1000 W, Time: 30 min	Empty chamber. Afterwards, open the chamber door and keep it open for at least 10-15 min to cool it down after the cleaning to avoid particles.
3.1.2. Plasma activation	Plasma Asher 1	Gas: O_2: 300 ml/min, Power: 400 W, Time: 40 sec	
3.2. Wafer pre-bonding			***2' InP, 4' Si w/ SiO_2***
3.2.1. Si wafer unloading	Teflon bonding chuck	Place and align on the Teflon chuck (face up), add the teflon corner tool on top	

Step Heading	Equipment	Procedure	Comments
3.2.2. InP wafer unloading	Teflon bonding chuck	Position and align a few mm above the Si wafer (face down)	
3.2.3. Putting in contact	Teflon bonding chuck	Release the InP wafer, let it drop on Si, guided by the teflon corner tool	
3.2.4. Applying pressure	Teflon pressing tool	Quickly press with the Teflon pressing tool in the middle of the InP wafer, then press around	At this point, wafers should be locked together
3.3. Wafer bonding in a wafer bonder			***2' InP with 4' SiO_2/Si***
3.3.1. Loading Wafer	Bonder O_2	Place on the chuck	
3.3.2. Bonding process	Wafer Bonder O_2	Recipe: ausa/'300Cbonding -2to4inch, Temperature: 300 °C, Force: 2 kN, Pressure: vacuum	Total time 2.5 h
3.3.3. Unloading	Wafer Bonder O_2		Inspect if no cracks are visible
3.4. Substrate removal			
3.4.1. Wet etching	HCl	Time: 1 h, Use our own beaker	Preferably use a magnetic stirrer for agitation
3.4.2. Rinse	DI water		
3.4.3. Blow dry	N_2		
3.5. Collapsing of InP membranes above preAM openings in SiO_2			
3.5.1. Opening preAM openings in SiO_2	Solvents fumehood	Ultrasonic bath: level 9, 1 min, Put the bonded InP/Si wafer upside down into the 4' glass beaker filled with water onto some Teflon holder inside (to keep InP surface uncovered), and put the beaker into the ultrasonic bath.	This step is needed to remove InP membranes above preAM openings to ensure alignment marks are uncovered. It should be done before InGaAs removal to avoid particles on InP surface. This method works with 90% success rate (HERO AM mask has extra alignment marks for redundancy). Inspect under the microscope afterward.
3.6. Etch-stop layer removal			
3.6.1. InGaAs wet etching	H_2SO_4, H_2O_2	Mixture: (10%)H_2SO_4:H_2O_2 = 1:1, Time: 30 s	

Step Heading	Equipment	Procedure	Comments
3.4.2. Rinse	DI water		
3.4.3. Blow dry	N_2		
3.7. PL mapping			
3.7.1. Emission characterization	PL mapper	532/980 nm, surface-map/wide-scan	Use the same parameters as before for comparison.
3.8. Thickness mapping			
3.8.1. Thickness estimation	Ellipsometer VASE	Mapping 9 points (center and 8 points around), Angle scan: 65° — 70° - 75°, Acq. time: 3 s	Make sure this is done before ICP etching of BH!
4. BH definition			***e-beam with negative resist***
4.1. Sample surface preparation before e-beam resist coating			
4.1.1. Wet etching	BHF	Time: 30 s, Use our own beaker	A very important step for proper HSQ adhesion to the InP surface.
3.4.2. Rinse	DI water	use our own beaker	
3.4.3. Blow dry	N_2		
4.2. E-beam resist coating			
4.2.1. Baking	Hot plate	5 min, 220 °C	
4.2.2. Spin-coating	XR-1541-006	60 s, 2000 RPM, 3000 /s2	Take the bottle out of the refrigerator 20-30 min before opening. Expected thickness 120 nm.
4.2.3. Baking	Hot plate	2 min, 120 °C, 2 min, 220 °C	
4.3. Buried heterostructure mask exposure in e-beam			
4.3.1. Cassette loading	E-beam	preferably 4' Ti cassette	Keep the cassette inside the e-beam machine for >30 min to stabilize the temperature, check it with the temperature monitor software
4.3.2. Pre-alignment	E-beam	pre-alignment stage	Choose good quality P and Q global alignment marks
4.3.3. Exposure	E-beam	Condition file: 45na_ap8, Dose: 4000 C/cm2, with PEC, Alignment: P and Q global marks; chip marks for individual chips	Optimized e-beam alignment marks detection parameters (etched marks in Si): BE Coarse gain: 1, BE Middle gain: 12, BE Fine gain: 128, WAVE offset: 128, BE offset: 1806, 16 scans for chip marks.

Step Heading	Equipment	Procedure	Comments
4.4. E-beam resist development			
4.4.1. Development	E-beam development fumehood in E-4	Mixture: AZ400K:H2O = 1:3, Time: 2 min 40 s	
4.4.2. Rinse	E-beam development fumehood in E-4	Wafer in a beaker with water, spraying water into the beaker with a hose	Important! Do not spray water directly onto the wafer surface to prevent e-beam resist from being washed away.
4.4.3. Blow dry	N_2		
4.5. Descum before ICP etching of BH			
4.5.1. Chamber cleaning	Plasma Asher 1	Gas: O_2: 210 ml/min, N_2: 70 ml/min, Power: 1000 W, Time: 30 min	Empty chamber. Then, open the chamber door and keep it open for at least 10-15 min to cool it down to avoid particles.
4.5.2. Plasma activation	Plasma Asher 1	Gas: O_2: 300 ml/min, Power: 400 W, Time: 40 sec	Descum step is to make sure there are no residues
4.6. Formation of mesa-structures by dry etching			
4.6.1. Chamber preparation	III-V ICP	Temperature: heat up to 180 °C, Chamber cleaning: 30 min O_2 clean	Special recipe has to be run for ICP heating.
4.6.2. Chamber preconditioning	III-V ICP	Recipe: ausa/"HBr etch (low p)', Time: 15 min, Carrier: dummy 4' Si	Updated recipe with pressure reduced from 5 to 1 mTorr (and added strike pressure to ignite plasma), resulting in better sidewall roughness. 30 min O_2 chamber clean and 15 min precondition in between each BH etching.
4.6.3. Dry etching	III-V ICP	Recipe: ausa/"HBr etch (low p)' ,Time: 30 − 60 s	Keep etch time set for 15 min and then stop manually by tracking EtchDirector signal according to the sample layer model.
4.6.4. Unloading	DI water	Put into the glass beaker with DI water to neutralize Br	
4.6.5. Chamber cleaning	III-V ICP	30 min O_2 clean, Temperature: set back to 20 °C	Special recipe has to be run for ICP cooling.

Step Heading	Equipment	Procedure	Comments
4.7. Thickness mapping			
4.7.1. Thickness estimation	Ellipsometer VASE	Mapping 9 points (center and 8 points around), Angle scan: 65° — 70° - 75°, Acq. time: 3 s	Make sure this is done before the 1st MOVPE regrowth!
4.8. Descum before 1st MOVPE regrowth			
4.8.1. Chamber cleaning	Plasma Asher 1	Gas: O_2: 210 ml/min, N_2: 70 ml/min, Power: 1000 W, Time: 30 min	Empty chamber. Afterward, open the chamber door and keep it open for at least 10-15 min to cool it down after the cleaning to avoid particles.
4.8.2. Plasma activation	Plasma Asher 1	Gas: O_2: 300 ml/min, Power: 400 W, Time: 5 min	The need for this step before the regrowth is not certain.
4.9. Sample preparation for the 1st re-growth			***Right before the regrowth***
4.9.1. Cleaning/wet etching	III-V acid/base fumehood	Mixture: concentrated H_2SO_4 (96%) 20 nm InP etch assumed. Time: 3 min. Use dedicated H_2SO_4 and DIW beakers to avoid MOVPE contamination.	Etch in the III-V fumehood, rinse for 15 s under running water, place the wafer in a beaker filled with water and transport to the MOVPE wetbench for additional DIW rinsing.
4.9.2. Transportation	Chemical trolley	Wafer in the beaker with water. Use napkins below to absorb any splashes of water.	
4.9.3.Rinse	DI water	Time: 1 min	
4.9.4. Rinse (bubbler)	DI water	Time: 3 min	
4.9.5. Blow dry	N_2	No more tweezers, use vacuum handler.	
4.10. 1st MOVPE re-growth (selective area growth)			
4.10.1. Sample loading into the load-lock	MOVPE	Load and evacuate for >30 min	Make sure wafer backside is completely dry.
4.10.2. InP regrowth	MOVPE	Regrowth thickness: aiming for what was etched in III-V ICP + H_2SO_4 cleaning/etching	Estimated from comparing ellipsometer thickness maps.

Step Heading	Equipment	Procedure	Comments
4.11. Thickness mapping			
4.11.1. Thickness estimation	Ellipsometer VASE	Mapping 9 points (center and 8 points around), Angle scan: 65° – 70° - 75°, Acq. time: 3 s	
4.12. E-beam resist removal, 1st step			
4.12.1. Wet etching	III-V acid/base fumehood	BHF, 2 min	Use a dedicated beaker to avoid MOVPE contamination.
4.12.2. Rinse	III-V acid/base fumehood	DIW wafer	Use a dedicated beaker to avoid MOVPE contamination.
4.12.3. Blow dry	III-V acid/base fumehood	N_2	
4.13. Aggressive ashing to make sure HSQ is fully removed			
4.13.1. Chamber cleaning	Plasma Asher 1	Gas: O_2: 210 ml/min, N_2: 70 ml/min, Power: 1000 W, Time: 30 min	Empty chamber. Afterward, open the chamber door and keep it open for at least 10-15 min to cool it down after the cleaning to avoid particles.
4.13.2. Plasma activation	Plasma Asher 1	Gas: O_2: 210 ml/min, Power: 1000 W, Time: 5 min	Aggressive ashing to make sure no HSQ residues are left before the 2nd MOVPE regrowth.
4.14. E-beam resist removal, 2nd step			
4.14.1. Wet etching	III-V acid/base fumehood	BHF, 2 min, Use a dedicated beaker to avoid MOVPE contamination.	Repeated BHF etching to make sure HSQ or its residues are fully gone before the 2nd MOVPE regrowth.
4.14.2. Rinse	III-V acid/base fumehood	DIW wafer	Use a dedicated beaker to avoid MOVPE contamination.
4.14.3. Blow dry	III-V acid/base fumehood	N_2	
4.15. Sample preparation for the 2nd re-growth			***Right before re-growth***

Step Heading	Equipment	Procedure	Comments
4.15.1. Cleaning/wet etching	III-V acid/base fumehood	Mixture: concentrated H_2SO_4 (96%),	25 nm InP etch assumed. Use dedicated H_2SO_4 and DIW beakers to avoid MOVPE contamination. Etch in the III-V fumehood, rinse for 15 s under running water, place the wafer in a beaker filled with water and transport to the MOVPE wetbench for additional DIW rinsing.
4.15.2. Transportation	Chemical trolley	Wafer in the beaker with water.	Use napkins below to absorb any splashes of water.
4.9.3.Rinse	DI water	Time: 1 min	
4.9.4. Rinse (bubbler)	DI water	Time: 3 min	
4.9.5. Blow dry	N_2	No more tweezers, use vacuum handler.	
4.16.2nd MOVPE re-growth (planarization)			
4.16.1. Sample loading into the load-lock	MOVPE	Load and evacuate for >30 min	Make sure wafer backside is completely dry.
4.16.2. InP re-growth	MOVPE	Re-growth thickness: aiming for 250 nm final InP membrane thickness and 50 nm InGaAs thickness	Estimated from comparing ellipsometer thickness maps.
4.17. Thickness mapping			
4.17.1. Thickness estimation	Ellipsometer VASE	Mapping 9 points (center and 8 points around), Angle scan: 65° – 70° - 75°, Acq. time: 3 s	
5. Alignment marks cleaning from grown III-V			
5.1. Adhesion promoting			
5.1.1. Baking	Hot plate	5 min, 100 °C	
5.1.2. Adhesion promoting	Surpass 3000	1 min dip	Afterwards, collect Surpass3000 in a waste bottle.
5.1.3. Rinse (beaker)	DI water	1 min dip	
5.1.4. Rinse	DI water		
5.1.5. Blow dry	N_2		
5.2. AZ5214 spin coating			

Step Heading	Equipment	Procedure	Comments
5.2.1. AZ5214 spin coating	Spin coater: Gamma UV	Sequence (xxxx on Gamma UV, 4140 on Gamma e-beam & UV) DCH 100mm 5214E 4.2um. Without HMDS	Expected thickness 4.2um
5.3. UV exposure			
5.3.1. UV exposure	Aligner MA6-2	Mask "HERO NATEC PRE-ALIGN' (dark field), Time 25s, intensity 11 mW/cm2, Hard contact mode	Rough alignment to existing pattern
5.4. AZ5214 development			
5.4.1. Development	Developer: TMAH UV-lithography	Sequence (1002): DCH 100mm SP 60s	
5.5. Descum			
5.5.1. Plasma ashing	Plasma Asher 1	20 s, 0.8 mbar, O_2 = 300 ml/min, 400 W	
5.6. Hard bake			
5.6.1. Hard bake	Developer: TMAH UV-lithography / Stepper 130°C 90s		
5.7. III-V wet etching			
5.7.1. InGaAs etch	$1H_2SO_4$(10%):$1H_2O_2$	2 min	
5.7.2. InP etch	1HCl:4H3PO4	40 min (with stirring)	
5.8. Resist strip			
5.8.1. Stripping	Acetone	5 min	
5.8.2. Cleaning	IPA / ethanol	Rinse	
5.8.3. Cleaning	DI water	Rinse	
5.8.4. Blow dry	N_2		
5.8.5. Plasma ashing	Plasma Asher 1	5 min, 0.8 mbar, O_2 = 300 ml/min, 400 W	
6. Si ion implantation		***DUV with positive resist***	
6.1. DUV resist coating			
6.1.1. BARC spin coating	Spin coater: Süss Stepper	Sequence (1202) DCH 100mm BARC 65nm	Dispense 1.6ml@1000rpm; spin-off 30s@3000rpm; softbake 60s@175°C

Step Heading	Equipment	Procedure	Comments
6.1.2. KRF M35G spin coating	Spin coater: Süss Stepper	Sequence (1402) DCH 100mm KRF M35G 750nm	Dispense 1ml@1000rpm; spin-off 60s@5000rpm; softbake 90s@130°C
6.2. DUV exposure			
6.2.1. Loading sample	4'—>6' adapter	Use 4-1107-04 adapter	Make the wafer major flat parallel to the side of the carrier holder
6.2.2. DUV exposure	DUV stepper Canon FPA 3000	Reticle NATEC_Hero_N_doped. Dose 350 J/m2, focus offset -0.25um Semi-manual TVPA alignment, automatic AGA alignment in 4 chips	
6.3. Development			
6.3.1. Post-exposure bake and development	Developer TMAH: Stepper	Sequence (1003) DCH PEB_90s and DEV_60s	It is possible to run separate sequences for PEB and development
6.4. Si ion implantation			
6.4.1. Si ion implantation	Ion Beam Services	Dose 2x1014 cm-2. Tilt 7°, RT, Rotation 30°	Implantation is done in BARC/InGaAs/InP Send samples to Ion Beam Services.
6.5. Resist strip			
6.5.1. Plasma ashing	Plasma Asher 1	5 min, 0.8 mbar, O_2 = 300 ml/min, 400 W	
6.6. Resist crust removal			
6.6.1. Wet etching	BHF	BHF (standard, 7:1) 1 min.	Very important step to avoid overall p-doping
6.6.2. Rinse	DI water		
6.6.3. Blow dry	N_2		
7. Zn diffusion			***DUV with positive resist***
7.1. Hard mask (SiO_2) deposition			
7.1.1. SiO_2 PECVD	PECVD4	HF SiO_2 with wafer clean for 94 s. Thickness 100 nm.	Test on a dummy.
7.2. DUV resist coating			
7.2.1. BARC spin coating	Spin coater: Süss Stepper	Sequence (1202) DCH 100mm BARC 65nm	Dispense 1.6ml@1000rpm; spin-off 30s@3000rpm; softbake 60s@175°C

Step Heading	Equipment	Procedure	Comments
7.2.2. KRF M35G spin coating	Spin coater: Süss Stepper	Sequence (1402) DCH 100mm KRF M35G 750nm	Dispense 1ml@1000rpm; spin-off 60s@5000rpm; softbake 90s@130°C
7.3. DUV exposure			
7.3.1. Loading sample	4' to 6' adapter		
7.3.2. DUV exposure	DUV stepper Canon FPA 3000	Reticle NATEC_Hero_N_doped. Dose 350 J/m2, focus offset -0.25um Semi-manual TVPA alignment, automatic AGA alignment in 4 chips	
7.4. Development			
7.4.1. Post-exposure bake and development	Developer TMAH: Stepper	Sequence (1003) DCH PEB_90s and DEV_60s	It is possible to run separate sequences for PEB and development
7.5. BARC etching			
7.5.1. BARC dry etching	III-V RIE	Recipe "BCB_LP' 1 min.	
7.6. Pattern transfer to SiO_2 hard mask (SiO_2 etching)			
7.6.1. Chamber preparation	III-V ICP	Chamber cleaning: 30 min O_2 clean	
7.6.2. Chamber preconditioning	III-V ICP	Recipe: "SiO_2_CF4_H2_v1', Time: 15 min	Carrier: dummy 4' AZ5214/Si
7.6.3. Si etching using AZ5214E mask	III-V ICP	Recipe: 'SiO2_CF4_H2_v1' Time: 190s	
7.6.4. Chamber cleaning	III-V ICP	30 min O_2 clean	
7.7. Resist strip			
7.7.1. Stripping	Acetone	5 min	
7.7.2. Cleaning	IPA / ethanol	Rinse	
7.7.3. Cleaning	DI water	Rinse	
7.7.4. Blow dry	N_2		
7.7.5. Plasma ashing	Plasma Asher 1	5 min, 0.8 mbar, O_2 = 300 ml/min, 400 W	

Step Heading	Equipment	Procedure	Comments
7.8. Sample preparation for Zn diffusion			
7.8.1. Cleaning	H_2SO_4	Time: 3 min	
7.8.2. Rinse	DI water	Time: 1 min	
7.8.3. Rinse (bubbler)	DI water	Time: 3 min	
7.8.4.. Blow dry	N_2	No more tweezers, use vacuum handler.	
7.9. Zn diffusion (MOVPE)			
Set DEZn bubbler T to be 30°C at least several hours before			
7.9.1. Zn diffusion	MOVPE	1) T=650°C, t=15min, AsH3=175sccm, 2) RT control, T=505°C, t=20min, AsH3=50sccm, DEZneff=6.9sccm, Pr.=500sccm	DEZn bubbler T=30°C (if InGaAs is properly lattice matched), otherwise T=18°C
7.10.Zn activation			
7.10.1. Rapid thermal annealing	Jipelec RTP	T/C control, T = 450°C, t = 5 min, N_2 200 sccm	Always do a dummy run to calibrate T setpoint
7.11.Hard mask removal (SiO_2 wet etching)			
7.11.1. SiO_2 wet etching	BHF	t = 1 min.	
7.11.2. Rinse	DI water		
7.11.3. Blow dry	N_2		
8. InGaAs etching			***UV with positive resist***
8.1. Adhesion promoting			
8.1.1. Baking	Hot plate	5 min, 100 °C	
8.1.2. Adhesion promoting	Surpass3000	1 min dip	
8.1.3. Rinse (beaker)	DI water	1 min dip	
8.1.4. Rinse	DI water		
8.1.5. Blow dry	N_2		
8.2. AZ5214 spin coating			
8.2.1. AZ5214 spin coating	Spin coater: Gamma UV	Sequence (3410 on Gamma UV, 4110 on Gamma e-beam & UV) DCH 100mm 5214E 1.5um. It includes Without HMDS: 1) Dispense 3ml@800rpm, 2) Spin-off for 30s@4500rpm, 3) Soft baking for 90s@90C.	Expected thickness 1.5um

Step Heading	Equipment	Procedure	Comments
8.3. UV exposure			
8.3.1. UV exposure	Aligner MA6-2	Mask "HERO_InGaAs_cap' (bright field) Alignment to "IGA' alignment marks, Hard contact mode, Time 7s, intensity 11 mW/cm2	
8.4. AZ5214 development			
8.4.1. Development	Developer: TMAH UV-lithography	Sequence: DCH 100mm SP 60s	
8.5. Descum			
8.5.1. Plasma ashing	Plasma Asher 1	5 min, 0.8 mbar, O_2 = 300 ml/min, 400 W	
8.6. Hard bake			
8.6.1. Hard bake	Developer:	TMAH UV-lithography 130°C 90s	
8.7. InGaAs wet etching			
8.7.1. InGaAs wet etching	H_2SO_4, H_2O_2	Mixture: (10 %)H_2SO_4:H_2O_2 = 1:1, Time: 30 s	Diluted etching solution. Endpoint can be detected by observing change of colour.
8.8. Resist strip			
8.8.1 Stripping	Acetone	5 min	
8.8.2. Cleaning	IPA / ethanol	Rinse	
8.8.3. Cleaning	DI water	Rinse	
8.8.4. Blow dry	N_2		
8.8.5. Plasma ashing	Plasma Asher 1	5 min, 0.8 mbar, O_2 = 300 ml/min, 400 W	
9. PhC definition			***e-beam with positive resist***
9.1. Hard-mask deposition			
9.1.1. Test deposition	PECVD4	Recipe: "HF SIN with wafer clean', Time: 17 min	On dummy Si
9.1.2. Thickness estimation	Ellipsometer VASE	Determine SiNx thickness and deposition rate on dummy Si	
9.1.3. Real deposition	PECVD4	Recipe: 'HF SIN with wafer clean', Time: ? min	Aim for 95 100 nm (reduced thickness from earlier 200 nm for better dry etching)

Step Heading	Equipment	Procedure	Comments
9.2. E-beam alignment/exposure of photonic crystal patterns			
9.2.1. Test coating	Spin Coater: Gamma ebeam & UV	Recipe: "4318-DCH 100mm CSAR 180nm'	On dummy Si, Make sure there is no particles on it, otherwise do another test
9.2.2. Real coating	Spin Coater: Gamma ebeam & UV	Recipe: "4318-DCH 100mm CSAR 180nm'	
9.2.3. Cassette loading	E-beam	preferably 2' Ti cassette, slot D, Condition file: 6na_ap5, Dose: 260 C/cm2, Shot pitch: 7.5 nm	Keep the cassette inside the e-beam machine for >30 min to stabilize the temperature, check it with the temperature monitor software
9.2.4. Prealignment	E-beam prealignment stage	Choose good quality P and Q global alignment marks	
9.2.5. Exposure	E-beam	Condition file: 2na_ap4 Dose: 260 – 290 C/cm2, with PEC, Alignment: P and Q global marks; chip marks for individual chips	Optimized e-beam alignment marks detection parameters, InP marks on SiO_2 (Si marks):BE Coarse gain: 1, BE Middle gain: 15 (12), BE Fine gain: 200 (128), WAVE offset: 85 (128), BE offset: 2020 (1800), 16 scans for chip marks.
9.3. E-beam resist development			
9.3.1. Development	Developer: E-beam	Recipe: 546 SP60s, Developer: SP 546	
9.4. Cleaving wafer into chips			
9.4.1. Cleaving	Cleaving fumehood	Cleaver: Lattice Axe	
9.5. Transfer of the photonic crystal patterns into the hard-mask			
9.5.1. Chamber preparation	III-V ICP	Chamber cleaning: 30 min O_2 clean	
9.5.2. Chamber preconditioning	III-V ICP	Recipe: ausa/"SiNx etch w/ strike', Time: 15 min, Carrier: dummy 4' Si	
9.7.3. Dry etching	III-V ICP	Recipe: ausa/"SiNx etch w/ strike', Time: 2 mins for 180 nm CSAR, Carrier: Dedicated dummy 4' Si	Track EtchDirector signal, for optimal etching signal should go through around 1.1 cycle

Step Heading	Equipment	Procedure	Comments
9.5.4. Chamber cleaning	III-V ICP	30 min O_2 clean	
9.6. E-beam resist strip			
9.6.1. Stripping	Ultrasonic bath	Mixture: Remover 1165, Level: 1, Temperature: <60°C, Time: 25 mins	III-V ICP etching does not burn ZEP, so its removal is easier. Usually less than an hour is enough, bath can be set to heating just during the removal.
9.6.2 Stripping	Acetone	5 min	
9.6.3. Cleaning	IPA	Rinse	
9.6.4. Cleaning	Ethanol	Rinse	
9.6.5. Blow dry	N_2		
9.6.6. Plasma ashing	Plasma Asher 1	5 min, 0.8 mbar, O_2 = 300 ml/min, 400 W	
9.7. Transfer of the photonic crystal patterns into the InP layer			
9.7.1. Chamber preparation	III-V ICP	Temperature: heat up to 180 °C, Chamber cleaning: 30 min O_2 clean	
9.7.2. Chamber preconditioning	III-V ICP	Recipe: ausa/"HBr etch (low p), PP 80 W', Time: 15 min, Carrier: dummy 4' Si	Recipe is the same as for BH etching, except that platen power is increased to 80 W for +better sidewalls verticality
9.7.3. Dry etching	III-V ICP	Recipe: ausa/"HBr etch (low p), PP 80 W, Time: 90s, Carrier: Dedicated dummy 4' Si	Exact optimal time is still being optimized.
9.7.4. Unloading	DI water	Put into the glass beaker with DI water to neutralize Br	
9.7.5. Chamber cleaning	III-V ICP	30 min O_2 clean if no more InP etching is done	
10. N-Me contacts			***UV with negative resist***
10.1.Chip bonding			
10.1.1. Bonding	Hotplate (90°C)	Crystalbond chip to 4' Si wafer	Keep flat alignment to ease maskless alignment

Step Heading	Equipment	Procedure	Comments
10.2.nLOF2020 spin coating			
10.2.1. nLOF2020 spin coating	Spin coater: Gamma UV	Sequence (2421) DCH 100mm nLOF 2020 2um HMDS. (4um for 200nm SiNx)	Adhesion promotion is done with HMDS in spin coater since almost all the surface is covered with silicon nitride.
10.3.UV exposure			
10.3.1. UV exposure	Aligner: MLA1 or MLA2	Mask n_Me_contact (inverted polarity!), MLA1: 365nm light, 2um nLOF: Dose: 300, defocus: 0 MLA2: 375nm light, 2um nLOF: Dose: 400, defocus: -4	Avoid large areas without any structures (lift-off would be difficult). Add some dummy stripes (check in the design where it is possible to add them).
10.3.2. UV exposure	Aligner MA6-2	Mask "HERO_N_Me' (bright field), Alignment to "N' alignment marks, Hard contact mode, Time 20s, intensity 11 mW/cm2	
10.4.nLOF cross-linking and development			
10.4.1. PEB and development	Developer: TMAH UV-lithography	Sequence: 3008 DCH 100mm PEB120s@110C + SP60s, Development time could be increased, but 60s is also fine	Check alignment in optical microscope.
10.5.Chip debonding			
10.5.1. Debonding	Hotplate (90°C)	Carefully release the chip by sliding it	
10.6.Hard baking			
10.6.1. Hard baking	Hotplates near manual spin coaters	1min@110C, 3min@150C, 15s@110C	Hotplate setpoints 121°C and 165°C.
10.7.Descum			
10.7.1. Plasma ashing	Plasma Asher 1	5 min, 0.8 mbar, O_2 = 300 ml/min, 400 W	
10.8.Nitride wet etching			
10.8.1. SiNx wet etching	BHF	t = 2 min 30 s	Check the color of the openings in the microscope if nitride is fully etched. Be careful not to undercut resist too much.
10.8.2. Rinse	DI water		
10.8.3. Blow dry	N_2		

Step Heading	Equipment	Procedure	Comments
10.9.N-Metal (Ni/Ge/Au) deposition			
10.9.1. Metal e-beam evaporation	Temescal / Physimeca	Ni 40nm, Ge 50nm, Au 125nm. Deposition rates: Ni, Au 5 Å/s, Ge 1 Å/s.	Deposition rate is not very important, but lower—>better. For Ge it is advisory to be extra careful (can spit if too fast).
10.10. Lift-off			
10.10.1. Lift-off Remover 1165	Lift-off fumehood	15 min, 60°C – 65°C, ultrasound 9. Vertical sample holder (to avoid metal flakes on the surface).	Check that the process is finished by visual inspection
10.10.2. Rinse IPA/ethanol	Lift-off fumehood	1 min, RT.	
10.10.3. Rinse DI water	Lift-off fumehood	1 min, RT.	
10.11. Resist residues strip			
10.11.1 Plasma ashing	Plasma Asher 1	5 min, 0.8 mbar, O_2 = 300 ml/min, 400 W	
11. P-Me contacts			***UV with negative resist***
11.1.Chip bonding			
11.1.1. Bonding	Hotplate (90°C)	Crystalbond chip to 4' Si wafer	Keep flat alignment to ease maskless alignment
11.2.nLOF2020 spin coating			
11.2.1. nLOF2020 spin coating	Spin coater: Gamma UV	Sequence (2421) DCH 100mm nLOF 2020 2um HMDS. (4um for 200nm SiNx)	Adhesion promotion is done with HMDS in spin coater since almost all the surface is covered with silicon nitride.
11.3.UV exposure			
11.3.1. UV exposure	Aligner: MLA1 or MLA2	Mask p_Me_contact (inverted polarity!), MLA1: 365nm light, 2um nLOF: Dose: 300, defocus: 0 MLA2: 375nm light, 2um nLOF: Dose: 400, defocus: -4	Avoid large areas without any structures (lift-off would be difficult). Add some dummy stripes (check in the design where it is possible to add them).
11.3.2. UV exposure	Aligner MA6-2	Mask "HERO_P_Me' (bright field), Alignment to "N' alignment marks, Hard contact mode, Time 20s, intensity 11 mW/cm2	

Step Heading	Equipment	Procedure	Comments
10.4.nLOF cross-linking and development			
11.4.1. PEB and development	Developer: TMAH UV-lithography	Sequence: 3008 DCH 100mm PEB120s@110C + SP60s, Development time could be increased, but 60s is also fine	Check alignment in optical microscope.
10.5.Chip debonding			
11.5.1. Debonding	Hotplate (90°C)	Carefully release the chip by sliding it	
10.6.Hard baking			
11.6.1. Hard baking	Hotplate	1min@110C, 3min@150C, 15s@110C	Hotplate setpoints 121°C and 165°C.
11.7.1. Plasma ashing	Plasma Asher 1	5 min, 0.8 mbar, O_2 = 300 ml/min, 400 W	
11.8.Nitride wet etching			
11.8.1. SiNx wet etching	BHF	t = 2 min 30 s	Check the color of the openings in the microscope if nitride is fully etched. Be careful not to undercut resist too much. Etching time is for 100 nm SiNx.
11.8.2. Rinse	DI water		
11.8.3.. Blow dry	N_2		
11.9.P-Metal (Ti/Pt/Au) deposition			
11.9.1. Metal e-beam evaporation	Temescal / Wordentec /Physimeca	Ti 30nm, Pt 50nm, Au 250nm. Deposition rates: 5 Å/s	Deposition rate is not very important.
11.10. Lift-off			
11.10.1. Lift-off Remover 1165	Lift-off fumehood	15 min, 60°C – 65°C, ultrasound 9. Vertical sample holder (to avoid metal flakes on the surface).	Check that the process is finished by visual inspection
11.10.2. Rinse IPA/ethanol	Lift-off fumehood	1 min, RT.	
11.10.3. Rinse DI water	Lift-off fumehood	1 min, RT.	
11.11. Resist residues strip			
11.11.1. Plasma ashing	Plasma Asher 1	5 min, 0.8 mbar, O_2 = 300 ml/min, 400 W	
12. Me contact thermal alloying			
12.1.Thermal alloying			

Step Heading	Equipment	Procedure	Comments
12.1.1. Rapid thermal annealing	Jipelec RTP	Recipe "anma_nall2', T/C control, T = 430°C, t = 20 s, N_2 200 sccm	Always do a dummy run to calibrate T setpoint. After annealing check N-Me colour, it should turn white (indication of successful alloying)
13. Membranization			***UV with positive resist***
13.1.Chip bonding			
13.1.1. Bonding	Hotplate (90°C)	Crystalbond chip to 4' Si wafer	Keep flat alignment to ease maskless alignment
13.2.AZ5214 spin coating			
13.2.1. AZ5214 spin coating	Spin coater: Gamma UV	Sequence (3421) DCH 100mm 5214E 2.2um HMDS.	
13.3.UV exposure			
13.3.1. UV exposure	Aligner: MLA1 / MLA2 / MLA3	Mask: 'membranization', MLA1: 365nm light, Dose: 130, defocus: 0	, MLA2: 375nm light, Dose: 100, defocus -3, MLA3: 405nm light ,Dose: 130, defocus: 0
13.3.1. UV exposure	Aligner MA6-2	Mask 'Membranization' (dark field)	Alignment to "M' alignment marks, Hard contact mode, Time 12s, intensity 11 mW/cm2
13.4.AZ5214 development			
13.4.1. Development	Developer: TMAH UV-lithography	Sequence (1002): DCH 100mm SP 60s	
13.5.Hard baking			
13.5.1. Hard baking	Developer: TMAH UV-lithography / Stepper	Sequence (2008) PEB 130°C, 90 s	Don't forget to return T setpoint back to 110°C (in case of Developer UV-Lithography).
13.6.Chip debonding			
13.6.1. Debonding	Hotplate (90°C)	Carefully release the chip by sliding it	
13.7.Descum			
13.7.1. Plasma ashing	Plasma Asher 1	5 min, 0.8 mbar, O_2 = 300 ml/min, 400 W	
13.8.Membranization			
13.8.1. Wet etching	BHF with wetting agent	15 min	Tested etch rate 80 nm/min
13.8.2. Rinse	DI water		

Step Heading	Equipment	Procedure	Comments
13.8.3. Blow dry	N_2		
13.9.Resist strip			
13.8.4. Stripping	Acetone	5 min	Vertical sample holder (to avoid resist flakes on the surface)
13.8.5. Cleaning	IPA / ethanol	Rinse	
13.8.6. Cleaning	DI water	Rinse	
13.8.7. Blow dry	N_2		
13.8.8. Plasma ashing	Plasma Asher 1	5 min, 0.8 mbar, O_2 = 300 ml/min, 400 W	Check in optical microscope for possible resist residues

List of Acronyms

BH	Buried-Heterostructure
CMOS	Complementary Metal-Oxide-Semiconductor
DTU	Technical University of Denmark (Danmarks Tekniske Universitet)
DUT	Device under test
DUV	Deep Ultraviolet
EL	Electroluminescence
FC	Fiber Coupler
FDTD	Finite-Difference in Time-Domain
FP	Fabry-Pérot
FT	Fourier Transform
FWHM	Full-Width at Half-Maximum
GC	Grating Coupler
ICT	Information and Communication Technology
IQE	Internal Quantum Efficiency
IR	Infrared
LD	Line Defect
LEAP	Lambda-Scale Embedded Active-Region laser
LIV	Light-Current-Voltage
MMF	Multi-mode fiber
MOVPE	Metallorganic Vapor Phase Epitaxy
NA	Numerical Aperture
NC	Nanocavity
NTT	Nippon Telegraph and Telephone Laboratories
OSA	Optical Spectrum Analyzer
PD	Photodiode
PhC	Photonic Crystal
PL	Photoluminescence
QD	Quantum Dots
QW	Quantum Well
RF	Radio Frequency
SEM	Scanning Electron Microcsopy
SLED	Superluminescent Light Emitting Diode
SMF	Single-mode fiber
SMSR	Side-mode Supression Ratio
SNR	Signal to Noise Ratio
TEC	Thermoelectric Cooler
TLS	Tunable Laser Source
UV	Ultraviolet
VNA	Vector Network Analyzer

Bibliography

1. Inc, C. S. *Cisco annual internet report (2018–2023)* (2020).
2. Rahman, M. A. & Asyhari, A. T. The Emergence of Internet of Things (IoT): Connecting Anything, Anywhere. *Computers* **8.** ISSN: 2073-431X (2019).
3. Krenn, M., Pollice, R., Guo, S. Y., *et al.* On scientific understanding with artificial intelligence. *Nature Reviews Physics* **4,** 761–769 (Oct. 2022).
4. Jones, N. How to stop data centres from gobbling up the world's electricity. *Nature* **561,** 163–166 (Sept. 2018).
5. IEA. *Data Centres and Data Transmission Networks* , Paris (2022).
6. Andrae, A. & Edler, T. On Global Electricity Usage of Communication Technology: Trends to 2030. *Challenges* **6,** 117–157. ISSN: 2078-1547 (2015).
7. 2021, I. *International technology roadmap for semiconductors* , IEEE (2021).
8. Hu, E. L., Brongersma, M. & Baca, A. in *Nanotechnology Research Directions for Societal Needs in 2020: Retrospective and Outlook* 417–444 (Springer Netherlands, Dordrecht, 2011). ISBN: 978-94-007-1168-6.
9. Waldrop, M. M. The chips are down for Moore's law. *Nature* **530,** 144–147 (Feb. 2016).
10. IRDS. *International technology roadmap for semiconductors* IEEE (2015).
11. Frank, D. J., Haensch, W., Shahidi, G. & Dokumaci, O. H. Optimizing CMOS technology for maximum performance. *IBM Journal of Research and Development* **50,** 419–431 (July 2006).
12. Miller, D. A. B. Are optical transistors the logical next step? *Nature Photonics* **4,** 3–5 (Jan. 2010).
13. Magen, N., Kolodny, A., Weiser, U. & Shamir, N. *Interconnect-Power Dissipation in a Microprocessor* in *Proceedings of the 2004 International Workshop on System Level Interconnect Prediction* (Association for Computing Machinery, Paris, France, 2004), 7–13. ISBN: 1581138180.
14. Miller, D. A. B. Attojoule Optoelectronics for Low-Energy Information Processing and Communications. *Journal of Lightwave Technology* **35,** 346–396. ISSN: 07338724 (3 Feb. 2017).

15. Margalit, N., Xiang, C., Bowers, S. M., *et al.* Perspective on the future of silicon photonics and electronics. *Applied Physics Letters* **118,** 220501 (2021).

16. Lee, B. G. *Driving Down Link Energy and Driving Up Link Density in GPU Networks* in *2022 Optical Fiber Communications Conference and Exhibition (OFC)* (2022), 01–03.

17. Sun, C., Wade, M. T., Lee, Y., *et al.* Single-chip microprocessor that communicates directly using light. *Nature* **528,** 534–538. ISSN: 1476-4687 (2015).

18. Atabaki, A. H., Moazeni, S., Pavanello, F., *et al.* Integrating photonics with silicon nanoelectronics for the next generation of systems on a chip. *Nature* **556,** 349–354. ISSN: 1476-4687 (2018).

19. Tang, M., Park, J.-S., Wang, Z., *et al.* Integration of III-V lasers on Si for Si photonics. *Progress in Quantum Electronics* **66,** 1–18. ISSN: 0079-6727 (2019).

20. Corbett, B., Loi, R., Zhou, W., Liu, D. & Ma, Z. Transfer print techniques for heterogeneous integration of photonic components. *Progress in Quantum Electronics* **52,** 1–17. ISSN: 0079-6727 (2017).

21. Matsuo, S. & Kakitsuka, T. Low-operating-energy directly modulated lasers for short-distance optical interconnects. *Advances in Optics and Photonics* **10,** 567. ISSN: 1943-8206 (2018).

22. Utaka, K., Kobayashi, K. I. & Suematsu, Y. Lasing Characteristics of 1.5-1.6 µm GalnAsP/lnP Integrated Twin-Guide Lasers with First-Order Distributed Bragg Reflectors. *IEEE Journal of Quantum Electronics* **17** (5 1981).

23. Itaya, Y., Oishi, M., Nakao, M., *et al.* Low-threshold operation of 1.5µm buried-heterostructure DFB lasers grown entirely by low-pressure MOVPE. *Electronics Letters* **23** (5 1987).

24. Room-temperature operation of an InGaAsP double-heterostructure laser emitting at 1.55 m on a Si substrate. *Applied Physics Letters* **57** (6 1990).

25. GaInAsP Lateral Current Injection Lasers on Semi-insulating Substrates. *IEEE Photonics Technology Letters* **6** (4 1994).

26. Nunoya, N., Nakamura, M., Yasumoto, H., *et al.* Sub-milliampere operation of 1.55 µm wavelength high index-coupled buried heterostructure distributed feedback lasers. *Electronics Letters* **36** (14 July 2000).

27. Nakahara, K., Tsuchiya, T., Kitatani, T., *et al. 12.5-Gb/s Direct Modulation Up to 115 C in 1.3-µm InGaAlAs-MQW RWG DFB Lasers With Notch-Free Grating Structure* in. **22** (Jan. 2004), 159–165.

28. Tadokoro, T., Yamanaka, T., Kano, F., *et al. Operation of a 25-Gbps Direct Modulation Ridge Waveguide MQW-DFB Laser up to 85 °C* in (OSA, 2009), OThT3. ISBN: 978-1-55752-865-0.

29. Koyama, F., Kinoshita, S. & Iga, K. Room-temperature continuous wave lasing characteristics of a GaAs vertical cavity surface-emitting laser. *Applied Physics Letters* **55** (3 1989).

30. Babi, D. I., Mirin, R. P., Margalit, N. M., *et al.* Room-Temperature Continuous-Wave Operation of 1.54-µm Vertical-Cavity Lasers. *IEEE Photonics Technology Letters* **7** (11 1995).

31. Yang, G., MacDougal, M. & Dapkus, P. Ultralow threshold current vertical-cavity surface-emitting lasers obtained with selective oxidation. *Electronics Letters* **31,** 886–888 (11 May 1995).

32. Margalit, N. M., Babic, D. I., Streubel, K., *et al. Sub-milliamp long wavelength vertical cavity lasers* in *Conference Digest - IEEE International Semiconductor Laser Conference* (IEEE, 1996).

33. Nishiyama, N., Caneau, C., Hall, B., *et al.* Long-Wavelength Vertical-Cavity Surface-Emitting Lasers on InP With Lattice Matched AlGaInAs-InP DBR Grown by MOCVD. *IEEE Journal on Selected Topics in Quantum Electronics* **11** (5 2005).

34. Hofmann, W., Müller, M., Nadtochiy, A., *et al.* 22-Gb/s Long Wavelength VCSELs. *Opt. Express* **17,** 17547–17554 (2009).

35. Matsuo, S., Fujii, T., Hasebe, K., *et al.* Directly modulated buried heterostructure DFB laser on SiO_2/Si substrate fabricated by regrowth of InP using bonded active layer. *Optics Express* **22** (2014).

36. Nishi, H., Fujii, T., Takeda, K., *et al.* Membrane distributed-reflector laser integrated with SiO_x-based spot-size converter on Si substrate. *Optics Express* **24** (2016).

37. Tomiyasu, T., Hiratani, T., Inoue, D., *et al.* High-differential quantum efficiency operation of GaInAsP/InP membrane distributed-reflector laser on Si. *Applied Physics Express* **10** (2017).

38. Park, H. G., Kim, S. H., Kwon, S. H., *et al.* Electrically driven single-cell photonic crystal laser. *Science* **305,** 1444–1447. ISSN: 00368075 (2004).

39. Seo, M. K., Jeong, K. Y., Yang, J. K., *et al.* Low threshold current single-cell hexapole mode photonic crystal laser. *Applied Physics Letters* **90,** 171122. ISSN: 00036951 (2007).

40. Takeda, K., Sato, T., Shinya, A., *et al.* Few-fJ/bit data transmissions using directly modulated lambda-scale embedded active region photonic-crystal lasers. *Nature Photonics* **7,** 569–575. ISSN: 17494885 (2013).

41. Jeong, K.-Y., No, Y.-S., Hwang, Y., *et al.* Electrically driven nanobeam laser. *Nature Communications* **4,** 2822. ISSN: 2041-1723 (2013).

42. Kuramochi, E., Duprez, H., Kim, J., *et al.* Room temperature continuous-wave nanolaser diode utilized by ultrahigh-Q few-cell photonic crystal nanocavities. *Optics Express* **26,** 26598 (2018).

43. Takeda, K., Sato, T., Fujii, T., *et al.* Heterogeneously integrated photonic-crystal lasers on silicon for on/off chip optical interconnects. *Optics Express* **23,** 702. ISSN: 1094-4087 (2015).

44. Crosnier, G., Sanchez, D., Bouchoule, S., *et al.* Hybrid indium phosphide-on-silicon nanolaser diode. *Nature Photonics* **11,** 297–300. ISSN: 17494893 (2017).

45. Takeda, K., Tsurugaya, T., Fujii, T., *et al.* Optical links on silicon photonic chips using ultralow-power consumption photonic-crystal lasers. *Optics Express* **29,** 26082. ISSN: 1094-4087 (2021).

46. Dimopoulos, E., Sakanas, A., Marchevsky, A., *et al.* Electrically-driven Photonic Crystal Lasers with Ultra-low Threshold. *Laser & Photonics Reviews,* 2200109. ISSN: 1863-8880. eprint: 2207.02931 (2022).

47. Dimopoulos, E., Xiong, M., Sakanas, A., *et al.* Experimental Demonstration of Nanolaser with sub-μA Threshold Current. *arXiv,* 2212.05148 (2022).

48. Matsuoka, T. & Iwashita, K. *History of Distributed Feedback Laser* in *2017 IEEE HISTory of ELectrotechnolgy CONference (HISTELCON)* (2017), 127–132.

49. Michalzik, R. *VCSELs: Fundamentals, Technology and Applications of Vertical-Cavity Surface-Emitting Lasers* ISBN: 9783642249860 (Springer Berlin Heidelberg, 2012).

50. Akahane, Y., Asano, T., Song, B.-S. & Noda, S. High-Q photonic nanocavity in a two-dimensional photonic crystal. *Nature* **425,** 944–947. ISSN: 1476-4687 (2003).

51. Matsuo, S., Shinya, A., Kakitsuka, T., *et al.* High-speed ultracompact buried heterostructure photonic-crystal laser with 13 fJ of energy consumed per bit transmitted. *Nature Photonics* **4,** 648–654. ISSN: 17494885 (2010).

52. Matsuo, S., Shinya, A., Chen, C.-H., *et al.* 20-Gbit/s directly modulated photonic crystal nanocavity laser with ultra-low power consumption. *Optics Express* **19,** 2242. ISSN: 1094-4087 (2011).

53. Jang, H., Karnadi, I., Pramudita, P., *et al.* Sub-microWatt threshold nanoisland lasers. *Nature Communications* **6.** ISSN: 20411723 (2015).

54. Takeda, K., Fujii, T., Shinya, A., *et al. 1-fJ/bit Direct Modulation of Photonic-Crystal Lasers* in (IEEE, Sept. 2018), 1–3. ISBN: 978-1-5386-4862-9.

55. Hall, R. N., Fenner, G. E., Kingsley, J. D., Soltys, T. J. & Carlson, R. O. Coherent Light Emission From GaAs Junctions. *Phys. Rev. Lett.* **9,** 366–368 (9 1962).

56. Yablonovitch, E., Gmitter, T. J. & Leung, K. M. Photonic band structure: The face-centered-cubic case employing nonspherical atoms. *Phys. Rev. Lett.* **67,** 2295–2298 (17 1991).

57. Joannopoulos, J. D., Johnson, S. G., Winn, J. N. & Meade, R. D. *Photonic Crystals: Molding the Flow of Light* 2nd ed. ISBN: 0691124566 (Princeton University Press, 2008).

58. Jiao, Y., Nishiyama, N., Van Der Tol, J., *et al. InP membrane integrated photonics research* 2020.

59. Notomi, M. Spontaneous Emission Probabilities at Ratio Frequencies. *Physical Review* **69,** 681 (1964).

60. Lodahl, P., Floris van Driel, A., Nikolaev, I. S., *et al.* Controlling the dynamics of spontaneous emission from quantum dots by photonic crystals. *Nature* **430,** 654–657. ISSN: 1476-4687 (2004).

61. Lodahl, P., Mahmoodian, S. & Stobbe, S. Interfacing single photons and single quantum dots with photonic nanostructures. *Rev. Mod. Phys.* **87,** 347–400 (2 2015).

62. Kwon, S.-H., Park, H.-G. & Lee, Y.-H. in *Advances in Semiconductor Lasers* (eds Coleman, J. J., Bryce, A. C. & Jagadish, C.) 301–333 (Elsevier, 2012).

63. Notomi, M. Manipulating light with strongly modulated photonic crystals. *Reports on Progress in Physics* **73,** 096501 (2010).

64. Coles, R. J., Prtljaga, N., Royall, B., *et al.* Waveguide-coupled photonic crystal cavity for quantum dot spin readout. *Opt. Express* **22,** 2376–2385 (2014).

65. Okano, M, Yamada, T, Sugisaka, J, *et al.* Analysis of two-dimensional photonic crystal L-type cavities with low-refractive-index material cladding. *Journal of Optics* **12,** 075101. ISSN: 20408986 (2010).

66. Sauvan, C., Lecamp, G., Lalanne, P. & Hugonin, J. Modal-reflectivity enhancement by geometry tuning in Photonic Crystal microcavities. *Opt. Express* **13,** 245–255 (2005).

67. Hagemeier, J., Bonato, C., Truong, T.-A., *et al.* H1 photonic crystal cavities for hybrid quantum information protocols. *Opt. Express* **20,** 24714–24726 (2012).

68. Chalcraft, A. R., Lam, S., O'Brien, D., *et al.* Mode structure of the L3 photonic crystal cavity. *Applied Physics Letters* **90.** ISSN: 00036951 (2007).

69. Galli, M., Portalupi, S. L., Belotti, M., *et al.* Light scattering and Fano resonances in high-Q photonic crystal nanocavities. *Applied Physics Letters* **94** (2009).

70. Säynätjoki, A., Mulot, M., Ahopelto, J. & Lipsanen, H. Dispersion engineering of photonic crystal waveguides with ring-shaped holes. *Opt. Express* **15,** 8323–8328 (2007).

71. Caer, C., Le Roux, X., Do, V. K., *et al.* Dispersion Engineering of Wide Slot Photonic Crystal Waveguides by Bragg-Like Corrugation of the Slot. *IEEE Photonics Technology Letters* **23,** 1298–1300 (2011).

72. Song, B. S., Noda, S., Asano, T. & Akahane, Y. Ultra-high-Q photonic double-heterostructure nanocavity. *Nature Materials* **4,** 207–210. ISSN: 14761122 (2005).

73. Asano, T., Song, B.-S. & Noda, S. Analysis of the experimental Q factors (∼1 million) of photonic crystal nanocavities. *Opt. Express* **14,** 1996–2002 (2006).

74. Takahashi, Y., Hagino, H., Tanaka, Y., Asano, T. & Noda, S. *High-Q photonic nanocavity with a 2-ns photon lifetime* tech. rep. (2008).

75. Asano, T., Ochi, Y., Takahashi, Y., Kishimoto, K. & Noda, S. Photonic crystal nanocavity with a Q factor exceeding eleven million. *Optics Express* **25,** 1769 (2017).

76. Notomi, M., Shinya, A., Mitsugi, S., Kuramochi, E. & Ryu, H.-Y. Waveguides, resonators and their coupled elements in photonic crystal slabs. *Opt. Express* **12,** 1551–1561 (2004).

77. Kuramochi, E., Notomi, M., Mitsugi, S., *et al.* Ultrahigh-Q photonic crystal nanocavities realized by the local width modulation of a line defect. *Applied Physics Letters* **88,** 041112 (2006).

78. Tanabe, T., Notomi, M., Kuramochi, E. & Taniyama, H. Large pulse delay and small group velocity achieved using ultrahigh-Q photonic crystal nanocavities. *Opt. Express* **15,** 7826–7839 (2007).

79. Matsuo, S., Shinya, A., Kakitsuka, T., *et al.* High-speed ultracompact buried heterostructure photonic-crystal laser with 13Â fJ of energy consumed per bit transmitted. *Nature Photonics* **4,** 648–654. ISSN: 1749-4893 (2010).

80. Kim, J., Shinya, A., Nozaki, K., *et al.* Narrow linewidth operation of buried-heterostructure photonic crystal nanolaser. *Optics Express* **20,** 11643. ISSN: 1094-4087 (2012).

81. Matsuo, S., Takeda, K., Sato, T., *et al.* Room-temperature continuous-wave operation of lateral current injection wavelength-scale embedded active-region photonic-crystal laser. *Opt. Express* **20,** 3773–3780 (2012).

82. Matsuo, S., Sato, T., Takeda, K., *et al.* Ultralow operating energy electrically driven photonic crystal lasers. *IEEE Journal on Selected Topics in Quantum Electronics* **19.** ISSN: 1077260X (2013).

83. Nishi, H., Takeda, K., Fujii, T., *et al. Low-Operating Energy Heterogeneously Integrated Photonic-Crystal Laser on Si Waveguide* in *2018 IEEE International Semiconductor Laser Conference (ISLC)* (2018), 1–2.

84. Fano, U. Effects of configuration interaction on intensities and phase shifts. *Physical Review* **124,** 1866–1878. ISSN: 0031899X (1961).

85. Limonov, M. F., Rybin, M. V., Poddubny, A. N. & Kivshar, Y. S. Fano resonances in photonics. *Nature Photonics* **11,** 543–554. ISSN: 17494893 (9 Sept. 2017).

86. Nozaki, K., Tanabe, T., Shinya, A., *et al.* Sub-femtojoule all-optical switching using a photonic-crystal nanocavity. *Nature Photonics* **4,** 477–483. ISSN: 1749-4893 (2010).

87. Heuck, M., Combrié, S., Lehoucq, G., *et al.* Heterodyne pump probe measurements of nonlinear dynamics in an indium phosphide photonic crystal cavity. *Applied Physics Letters* **103,** 181120 (2013).

88. Yu, Y., Heuck, M., Hu, H., *et al.* Fano resonance control in a photonic crystal structure and its application to ultrafast switching. *Applied Physics Letters* **105,** 061117 (2014).

89. Mork, J., Chen, Y. & Heuck, M. Photonic crystal fano laser: Terahertz modulation and ultrashort pulse generation. *Physical Review Letters* **113** (2014).

90. Rasmussen, T. S., Yu, Y. & Mork, J. Theory of Self-pulsing in Photonic Crystal Fano Lasers. *Laser and Photonics Reviews* **11** (2017).

91. Rasmussen, T. S., Yu, Y. & Mork, J. Suppression of Coherence Collapse in Semiconductor Fano Lasers. *Phys. Rev. Lett.* **123,** 233904 (23 2019).

92. Yu, Y., Xue, W., Semenova, E., Yvind, K. & Mork, J. Demonstration of a self-pulsing photonic crystal Fano laser. *Nature Photonics* **11,** 81–84 (2017).

93. Yu, Y., Sakanas, A., Zali, A. R., *et al.* Ultra-coherent Fano laser based on a bound state in the continuum. *Nature Photonics* **15,** 758–764 (2021).

94. Dong, G., Liang, S. L., Sakanas, A., *et al.* Cavity dumping using a microscopic Fano laser. *Optica* **10,** 248. ISSN: 2334-2536 (2023).

95. Mork, J., Yu, Y., Rasmussen, T. S., Semenova, E. & Yvind, K. Semiconductor Fano Lasers. *IEEE Journal of Selected Topics in Quantum Electronics* **25** (2019).

96. Dong, G., Xiong, M., Dimopoulos, E., *et al. Fano Laser Based on a Photonic Crystal Nanobeam Cavity* in *Conference on Lasers and Electro-Optics* (Optica Publishing Group, 2022), STu4E.6.

97. Fox, A. *Optical Properties of Solids* ISBN: 9780198506126 (Oxford University Press, 2001).

98. Chen, Y., Ben, J., Xu, F., *et al.* Review on the Progress of AlGaN-based Ultraviolet Light-Emitting Diodes. *Fundamental Research* **1,** 717–734 (Nov. 2021).

99. Tsao, J. Y., Han, J., Haitz, R. H. & Pattison, P. M. The Blue LED Nobel Prize: Historical context, current scientific understanding, human benefit. *Annalen der Physik* **527,** A53–A61 (June 2015).

100. Zhai, L., Löbl, M. C., Nguyen, G. N., *et al.* Low-noise GaAs quantum dots for quantum photonics. *Nature Communications* **11** (Sept. 2020).

101. Michalzik, R. *VCSELs: A Research Review* (ed Michalzik, R.) ISBN: 978-3-642-24986-0 (Springer Berlin Heidelberg, Berlin, Heidelberg, 2013).

102. Adams, A. R. Strained-Layer Quantum-Well Lasers. *IEEE Journal of Selected Topics in Quantum Electronics* **17,** 1364–1373 (2011).

103. Arai, S. & Maruyama, T. GaInAsP/InP Quantum Wire Lasers. *IEEE Journal of Selected Topics in Quantum Electronics* **15,** 731–742 (2009).

104. Reithmaier, J. P., Sęk, G., Löffler, A., *et al.* Strong coupling in a single quantum dot–semiconductor microcavity system. *Nature* **432,** 197–200 (Nov. 2004).

105. Hennessy, K., Badolato, A., Winger, M., *et al.* Quantum nature of a strongly coupled single quantum dot–cavity system. *Nature* **445,** 896–899 (Jan. 2007).

106. Mikhelashvili, V., Eyal, O., Khanonkin, I., *et al.* On the relationship between electrical and electro-optical characteristics of InAs/InP quantum dot lasers. *Journal of Applied Physics* **124,** 054501 (Aug. 2018).

107. Xue, W., Ottaviano, L., Chen, Y., *et al.* Thermal analysis of line-defect photonic crystal lasers. *Opt. Express* **23,** 18277–18287 (2015).

108. Abdollahinia, A., Banyoudeh, S., Rippien, A., *et al.* Temperature stability of static and dynamic properties of 1.55 µm quantum dot lasers. *Opt. Express* **26,** 6056–6066 (2018).

109. Banyoudeh, S., Abdollahinia, A., Eyal, O., *et al.* Temperature-Insensitive High-Speed Directly Modulated 1.55- μm Quantum Dot Lasers. *IEEE Photonics Technology Letters* **28,** 2451–2454 (2016).

110. Park, H. G., Kim, S. H., Seo, M. K., *et al.* Characteristics of electrically driven two-dimensional photonic crystal lasers. *IEEE Journal of Quantum Electronics* **41,** 1131–1141. ISSN: 00189197 (2005).

111. Oe, K., Noguchi, Y. & Caneau, C. GaInAsP lateral current injection lasers on semi-insulating substrates. *IEEE Photonics Technology Letters* **6,** 479–481 (1994).

112. Ellis, B., Mayer, M. A., Shambat, G., *et al.* Ultralow-threshold electrically pumped quantum-dot photonic-crystal nanocavity laser. *Nature Photonics* **5,** 297–300. ISSN: 17494885 (2011).

113. Petykiewicz, J., Shambat, G., Ellis, B. & Vučković, J. *Electrical design for lateral junction photonic crystal lasers* in *Physics and Simulation of Optoelectronic Devices XXI* (eds Witzigmann, B., Osinski, M., Henneberger, F. & Arakawa, Y.) **8619** (SPIE, 2013), 86190W. ISBN: 9780819493880.

114. Lupi, A., Chung, I. S. & Yvind, K. Electrical injection schemes for nanolasers. *IEEE Photonics Technology Letters* **26,** 330–333. ISSN: 10411135 (2014).

115. Sakanas, A. *Buried Heterostructure Photonic Crystal Lasers* PhD thesis (Technical University of Denmark, 2019).

116. Marchevsky, Andrey. *Doping Technologies for Lateral Junctions in Photonic Crystal Membranes* PhD thesis (Technical University of Denmark, 2020).

117. Mathiesen S. Kristoffer. *Design and fabrication of photonic crystal nanolasers* PhD thesis (Technical University of Denmark, 2020).

118. Bekele, D. A. *Photonic crystal Fano structures for all-optical signal processing* PhD thesis (Technical University of Denmark, 2018).

119. Quentin Saudan. *Advances in all-optical switching using Fano resonance photonic crystal nanocavities* PhD thesis (Technical University of Denmark, 2022).

120. Sakanas, A., Semenova, E., Ottaviano, L., Mørk, J. & Yvind, K. Comparison of processing-induced deformations of InP bonded to Si determined by e-beam metrology: Direct vs. adhesive bonding. *Microelectronic Engineering* **214,** 93–99 (2019).

121. Sahoo, H. K., Ottaviano, L., Zheng, Y., Hansen, O. & Yvind, K. Low temperature bonding of heterogeneous materials using Al2O3 as an intermediate layer. *Journal of Vacuum Science & Technology B, Nanotechnology and Microelectronics: Materials, Processing, Measurement, and Phenomena* **36,** 011202. ISSN: 2166-2746 (2018).

122. Vasco, J. P. & Hughes, S. Anderson Localization in Disordered LN Photonic Crystal Slab Cavities. *ACS Photonics* **5,** 1262–1272. ISSN: 23304022. arXiv: 1708.07891 (2018).

123. Ferrini, R., Leuenberger, D., Houdré, R., *et al.* Disorder-induced losses in planar photonic crystals. *Opt. Lett.* **31,** 1426–1428 (2006).

124. Hagino, H., Takahashi, Y., Tanaka, Y., Asano, T. & Noda, S. Effects of fluctuation in air hole radii and positions on optical characteristics in photonic crystal heterostructure nanocavities. *Physical Review B - Condensed Matter and Materials Physics* **79.** ISSN: 10980121 (2009).

125. Taguchi, Y., Takahashi, Y., Sato, Y., Asano, T. & Noda, S. Statistical studies of photonic heterostructure nanocavities with an average Q factor of three million. *Optics Express* **19,** 11916. ISSN: 1094-4087 (2011).

126. Portalupi, S. L., Galli, M., Belotti, M., *et al.* Deliberate versus intrinsic disorder in photonic crystal nanocavities investigated by resonant light scattering. *Physical Review B - Condensed Matter and Materials Physics* **84.** ISSN: 10980121 (2011).

127. Borregaard, S. K. & Dubré, A. H. *Fabrication and characterization of photonic crystal nanocavities* (DTU Department of Photonics Engineering, 2020).

128. Xiong, M., Sakanas, A., Dimopoulos, E., *et al.* Experimental Realization of Topology-Optimized InP Photonic Cavities with Extreme Dielectric Confinement, IM2A.7 (2021).

129. Marchevsky, A., Mørk, J. & Yvind, K. Doping technologies for InP membranes on silicon for nanolasers. *Proc. SPIE, Novel In-Plane Semiconductor Lasers XVIII* **10939,** 109390U–1–9 (2019).

130. Takeda, K., Matsuo, S., Fujii, T., *et al.* Epitaxial growth of InP to bury directly bonded thin active layer on SiO2/Si substrate for fabricating distributed feedback lasers on silicon. *IET Optoelectronics* **9,** 151–157. ISSN: 1751-8768 (2015).

131. Ferris-Prabhu, A. V. in *Defect and Fault Tolerance in VLSI Systems: Volume 1* (ed Koren, I.) 33–46 (Springer US, Boston, MA, 1989). ISBN: 978-1-4615-6799-8.

132. Lippi, G., Wang, T. & Puccioni, G. "Phase transitions" in small systems: Why standard threshold definitions fail for nanolasers. *Chaos, Solitons & Fractals* **157,** 111850. ISSN: 0960-0779 (2022).

133. Strauf, S. & Jahnke, F. Single quantum dot nanolaser. *Laser & Photonics Reviews* **5,** 607–633 (2011).

134. Prieto, I., Llorens, J. M., Muñoz-Camúñez, L. E., *et al.* Near thresholdless laser operation at room temperature. *Optica* **2,** 66. ISSN: 23342536 (2015).

135. Ota, Y., Kakuda, M., Watanabe, K., Iwamoto, S. & Arakawa, Y. Thresholdless quantum dot nanolaser. *Optics Express* **25,** 19981. ISSN: 10944087 (2017).

136. Ning, C. Z. What is laser threshold? *IEEE Journal on Selected Topics in Quantum Electronics* **19.** ISSN: 1077260X (2013).

137. Woodham, R. L. *Application Note: ReliaTest L/I Threshold Calculations Understanding the First and Second Derivative Threshold Algorithms* tech. rep. (ILX Lightwave Corporation, 2006).

138. Blood, P. On the dimensionality of optical absorption, gain, and recombination in quantum-confined structures. *IEEE Journal of Quantum Electronics* **36,** 354–362. ISSN: 00189197 (2000).

139. Nozaki, K., Kita, S. & Baba, T. Room temperature continuous wave operation and controlled spontaneous emission in ultrasmall photonic crystal nanolaser. *Optics Express* **15,** 7506. ISSN: 1094-4087 (2007).

140. McCutcheon, M. W., Rieger, G. W., Cheung, I. W., *et al.* Resonant scattering and second-harmonic spectroscopy of planar photonic crystal microcavities. *Applied Physics Letters* **87,** 1–3 (2005).

141. Portalupi, S. L., Galli, M., Reardon, C., *et al.* Planar photonic crystal cavities with far-field optimization for high coupling efficiency and quality factor. *Opt. Express* **18,** 16064–16073 (2010).

142. Portalupi, S. L., Galli, M., Belotti, M., *et al.* Deliberate versus intrinsic disorder in photonic crystal nanocavities investigated by resonant light scattering. *Physical Review B - Condensed Matter and Materials Physics* **84** (2011).

143. Lai, Y., Pirotta, S., Urbinati, G., *et al.* Genetically designed L3 photonic crystal nanocavities with measured quality factor exceeding one million. *Applied Physics Letters* **104** (2014).

144. Osterkryger, A. D., de Lasson, J. R., Heuck, M., *et al.* Spectral symmetry of Fano resonances in a waveguide coupled to a microcavity. *Optics Letters* **41,** 2065. ISSN: 0146-9592. arXiv: 1512.05869 (2016).

145. Fanton, J. P. Convolution and deconvolution: Two mathematical tools to help performing tests in research and industry. **12.** ISSN: 21076847 (2021).

146. Crowder, M. NIST Handbook of Mathematical Functions. *International Statistical Review* **79,** 167–168 (2011).

147. Liu, Y., Lin, J., Huang, G., Guo, Y. & Duan, C. Simple empirical analytical approximation to the Voigt profile. *J. Opt. Soc. Am. B* **18,** 666–672 (2001).

148. Olivero, J. & Longbothum, R. Empirical fits to the Voigt line width: A brief review. *Journal of Quantitative Spectroscopy and Radiative Transfer* **17,** 233–236 (1977).

149. Simbula, A., Schatzl, M., Zagaglia, L., *et al.* Realization of high- Q / v photonic crystal cavities defined by an effective Aubry-André-Harper bichromatic potential. *APL Photonics* **2** (2017).

150. Akahane, Y., Asano, T., Song, B. S. & Noda, S. High-Q photonic nanocavity in a two-dimensional photonic crystal. *Nature* **425,** 944–947 (2003).

151. Taguchi, Y., Takahashi, Y., Sato, Y., Asano, T. & Noda, S. Statistical studies of photonic heterostructure nanocavities with an average Q factor of three million. *Optics Express* **19,** 11916 (12 2011).

152. Saudan, Q., Bekele, D. A., Dong, G., *et al.* Crosstalk-free all-optical switching enabled by Fano resonance in a multi-mode photonic crystal nanocavity. *Optics Express* **30,** 7457 (2022).

153. Barth, C., Wolters, J., Schell, A. W., *et al.* Miniaturized Bragg-grating couplers for SiN-photonic crystal slabs. *Optics Express* **23,** 9803 (2015).

154. Albrechtsen, M., Lahijani, B. V., Christiansen, R. E., *et al.* Nanometer-scale photon confinement in topology-optimized dielectric cavities. *Nature Communications* **13.** ISSN: 20411723 (1 Dec. 2022).

155. Takahashi, Y., Hagino, H., Tanaka, Y., *et al.* High-Q nanocavity with a 2-ns photon lifetime. *Opt. Express* **15,** 17206–17213 (2007).

156. Coldren, L. A. & Corzine, S. *Diode Lasers and Photonic Integrated Circuits* (Wiley, 1995).

157. Xue, W., Yu, Y., Ottaviano, L., *et al.* Threshold Characteristics of Slow-Light Photonic Crystal Lasers. *Physical Review Letters* **116.** ISSN: 10797114. arXiv: 1508.05349 (2016).

158. Lalanne, P., Sauvan, C. & Hugonin, J. P. Photon confinement in photonic crystal nanocavities. *Laser and Photonics Reviews* **2,** 514–526. ISSN: 18638880 (2008).

159. Mork, J. & Lippi, G. L. Rate equation description of quantum noise in nanolasers with few emitters. *Applied Physics Letters* **112,** 141103. ISSN: 0003-6951 (2018).

160. Gregersen, N., Suhr, T., Lorke, M. & Mørk, J. Quantum-dot nano-cavity lasers with Purcell-enhanced stimulated emission. *Applied Physics Letters* **100,** 131107. ISSN: 00036951 (2012).

161. Romeira, B. & Fiore, A. Purcell Effect in the Stimulated and Spontaneous Emission Rates of Nanoscale Semiconductor Lasers. *IEEE Journal of Quantum Electronics* **54,** 1–12. ISSN: 00189197. eprint: 1801.08879 (2018).

162. Taflove, A. & Hagness, S. C. *Computational electrodynamics: the finite-difference time-domain method* 3rd (Artech House, Norwood, 2005).

163. Lumerical FDTD: 3D Electromagnetic Simulator. *Ansys Lumerical Inc.*

164. Yee, K. Numerical solution of initial boundary value problems involving maxwell's equations in isotropic media. *IEEE Transactions on Antennas and Propagation* **14,** 302–307 (1966).

165. Pettit, G. D. & Turner, W. J. Refractive index of InP. *Journal of Applied Physics* **36,** 2081. ISSN: 00218979 (6 1965).

166. Chusseau, L., Martin, P., Brasseur, C., *et al.* Carrier-induced change due to doping in refractive index of InP: Measurements at 1.3 and 1.5 m. *Applied Physics Letters* **69,** 3054–3056. ISSN: 00036951 (20 Nov. 1996).

167. De Lasson, J. R., Frandsen, L. H., Gutsche, P., *et al.* Benchmarking five numerical simulation techniques for computing resonance wavelengths and quality factors in photonic crystal membrane line defect cavities. *Optics Express* **26,** 11366. ISSN: 10944087 (9 Apr. 2018).

168. Joannopoulos, J. D., Johnson, S. G., Winn, J. N. & Meade, R. D. in *Photonic Crystals: Molding the Flow of Light - Second Edition* (Princeton University Press, 2011).

169. Kolodziejski, L. A., Fan, S., Villeneuve, P. & Joannopoulos, J. D. Guided modes in photonic crystal slabs. *Physical Review B - Condensed Matter and Materials Physics* **60,** 5751–5758. ISSN: 1550235X (1999).

170. Velha, P., Picard, E., Charvolin, T., *et al.* Ultra-High Q/V Fabry-Perot microcavity on SOI substrate. *Opt. Express* **15,** 16090–16096 (2007).

171. Simbula, A., Schatzl, M., Zagaglia, L., *et al.* Realization of high - Q/V photonic crystal cavities defined by an effective Aubry-André-Harper bichromatic potential. *APL Photonics* **2.** ISSN: 23780967 (2017).

172. Bazin, A., Raj, R. & Raineri, F. Design of Silica Encapsulated High-Q Photonic Crystal Nanobeam Cavity. *J. Lightwave Technol.* **32,** 952–958 (2014).

173. Nakamura, T., Takahashi, Y., Tanaka, Y., Asano, T. & Noda, S. Improvement in the quality factors for photonic crystal nanocavities via visualization of the leaky components. *Optics Express* **24,** 9541. ISSN: 1094-4087 (2016).

174. Saldutti, M., Xiong, M., Dimopoulos, E., *et al.* Modal properties of photonic crystal cavities and applications to lasers. *Nanomaterials* **11,** 1–29. ISSN: 20794991 (11 2021).

175. Yang, X.-S. Second Edition (ed Yang, X.-S.) 111–121. ISBN: 978-0-12-821986-7 (Academic Press, 2021).

176. Minkov, M. & Savona, V. Automated optimization of photonic crystal slab cavities. *Scientific Reports* **4.** ISSN: 20452322 (2014).

177. Andreani, L. C. & Gerace, D. Photonic-crystal slabs with a triangular lattice of triangular holes investigated using a guided-mode expansion method. *Phys. Rev. B* **73,** 235114 (23 2006).

178. Weile, D. & Michielssen, E. Genetic algorithm optimization applied to electromagnetics: a review. *IEEE Transactions on Antennas and Propagation* **45,** 343–353 (1997).

179. Asano, T. & Noda, S. Optimization of photonic crystal nanocavities based on deep learning. *Optics Express* **26,** 32704. ISSN: 10944087. arXiv: 1808.05722 (2018).

180. Christiansen, R. E. & Sigmund, O. Inverse design in photonics by topology optimization: tutorial. *Journal of the Optical Society of America B* **38,** 496. ISSN: 0740-3224. arXiv: 2008.11816 (2021).

181. Wang, F., Christiansen, R. E., Yu, Y., Mørk, J. & Sigmund, O. Maximizing the quality factor to mode volume ratio for ultra-small photonic crystal cavities. *Applied Physics Letters* **113.** ISSN: 00036951. arXiv: 1810.02417 (2018).

182. Taguchi, Y., Takahashi, Y., Sato, Y., Asano, T. & Noda, S. Statistical studies of photonic heterostructure nanocavities with an average Q factor of three million. *Optics Express* **19,** 11916. ISSN: 1094-4087 (2011).

183. Martínez, L. J., Prieto, I., Alén, B. & Postigo, P. A. Fabrication of high quality factor photonic crystal microcavities in InAsP\InP membranes combining reactive ion beam etching and reactive ion etching. *Journal of Vacuum Science & Technology B: Microelectronics and Nanometer Structures* **27,** 1801 (2009).

184. Srinivasan, K., Barclay, P. E., Painter, O., *et al.* Experimental demonstration of a high quality factor photonic crystal microcavity. *Applied Physics Letters* **83,** 1915–1917 (2003).

185. Yu, Y., Hu, H., Oxenløwe, L. K., Yvind, K. & Mork, J. Ultrafast all-optical modulation using a photonic-crystal Fano structure with broken symmetry. *Optics Letters* **40,** 2357. ISSN: 0146-9592 (2015).

186. Crosnier, G., Sanchez, D., Bazin, A., *et al.* High Q factor InP photonic crystal nanobeam cavities on silicon wire waveguides. *Optics Letters* **41,** 579 (2016).

187. Xu, T., Wheeler, M. S., Ruda, H. E., Mojahedi, M. & Aitchison, J. S. The influence of material absorption on the quality factor of photonic crystal cavities. *Opt. Express* **17,** 8343–8348 (2009).

188. Casey, H. C. & Carter, P. L. Variation of intervalence band absorption with hole concentration in p-type InP. *Applied Physics Letters* **44,** 82–83. ISSN: 00036951 (1984).

189. Bennett, B., Soref, R. & Del Alamo, J. Carrier-induced change in refractive index of InP, GaAs and InGaAsP. *IEEE Journal of Quantum Electronics* **26,** 113–122 (1990).

190. Blood, P. *Quantum Confined Laser Devices: Optical gain and recombination in semiconductors* (Oxford Master Series in Physics, 2015).

191. Geng, P., Li, W., Zhang, X., *et al.* Effects of temperature and redshift on the refractive index of semiconductors. *Journal of Applied Physics* **124.** ISSN: 10897550 (2018).

192. Matsuo, S., Shinya, A., Kakitsuka, T., *et al.* High-speed ultracompact buried heterostructure photonic-crystal laser with 13 fJ of energy consumed per bit transmitted. *Nature Photonics* **4,** 648–654. ISSN: 17494885 (2010).

193. Fuchs, G., Schiedel, C., Hangleiter, A., Härle, V. & Scholz, F. Auger recombination in strained and unstrained InGaAs/InGaAsP multiple quantum-well lasers. *Applied Physics Letters* **62,** 396–398. ISSN: 00036951 (1993).

194. Piprek, J., Abraham, P. & Bowers, J. E. Self-consistent analysis of high-temperature effects on strained-layer multiquantum-well InGaAsP-InP lasers. *IEEE Journal of Quantum Electronics* **36,** 366–374. ISSN: 00189197 (2000).

195. Pankove, J. I. Temperature Dependence of Emission Efficiency and Lasing Threshold in Laser Diodes. *IEEE Journal of Quantum Electronics* **4,** 119–122. ISSN: 15581713 (1968).

196. O'Gorman, J., Levi, A. F., Tanbun-Ek, T., Coblentz, D. L. & Logan, R. A. Temperature dependence of long wavelength semiconductor lasers. *Applied Physics Letters* **60,** 1058–1060. ISSN: 00036951 (1992).

197. Bazin, A., Monnier, P., Lafosse, X., *et al.* Thermal management in hybrid InP/silicon photonic crystal nanobeam laser. *Optics Express* **22,** 10570. ISSN: 1094-4087 (2014).

198. Marchal, M. *Experimental characterization and theoretical modeling of electrically driven nanolasers* (DTU Department of Electrical and Photonics Engineering, 2022).

199. Andryieuski, A., Lavrinenko, A. V. & Zhukovsky, S. V. Anomalous effective medium approximation breakdown in deeply subwavelength all-dielectric photonic multilayers. *Nanotechnology* **26,** 184001 (2015).

200. Spiga, S., Soenen, W., Andrejew, A., *et al.* Single-Mode High-Speed 1.5-μm VCSELs. *Journal of Lightwave Technology* **35,** 727–733. ISSN: 07338724 (2017).

201. Spiga, S., Schoke, D., Andrejew, A., *et al. Single-Mode 1.5-μm VCSELs with 22-GHz Small-Signal Bandwidth* in *Optical Fiber Communication Conference* (Optica Publishing Group, 2016), Tu3D.4.

202. Haglund, E. P., Westbergh, P., Gustavsson, J. S. & Larsson, A. Impact of Damping on High-Speed Large Signal VCSEL Dynamics. *J. Lightwave Technol.* **33,** 795–801 (2015).

203. Sakanas, A., Marchevsky, A., Dimopoulos, E., *et al. Electrically-operated buried-heterostructure nanocavity laser with sub-20 μA threshold current* in *Conference on Lasers and Electro-Optics* (Optica Publishing Group, Washington, D.C., 2021), STu2C.3. ISBN: 978-1-943580-91-0.

204. Tucker, R. S., Wiesenfeld, J. M., Downey, P. M. & Bowers, J. E. Propagation delays and transition times in pulse-modulated semiconductor lasers. *Applied Physics Letters* **48,** 1707–1709. ISSN: 00036951 (1986).

205. Baba, T. Slow light in photonic crystals. *Nature Photonics* **2,** 465–473 (Aug. 2008).

206. Baba, T., Adachi, J., Ishikura, N., *et al.* Dispersion-controlled slow light in photonic crystal waveguides. *Proceedings of the Japan Academy, Series B* **85,** 443–453 (2009).

{2.7182818284}ϑφερτυθιοπσδφγηξκλ